University of California
Santa Barbara

Block Copolymer Membranes for Protein Nanopore-Based Biosensing

A dissertation submitted in partial satisfaction
of the requirements for the degree

Doctor of Philosophy
in
Physics

by

Justin Daniel Rofeh

Committee in charge:

Professor Luke Theogarajan, Co-Chair
Professor Deborah Fygenson, Co-Chair
Professor Philip Pincus

December 2017

The Dissertation of Justin Daniel Rofeh is approved.

Professor Philip Pincus

Professor Deborah Fygenson, Committee Co-Chair

Professor Luke Theogarajan, Committee Co-Chair

September 2017

Block Copolymer Membranes for Protein Nanopore-Based Biosensing

by

Justin Daniel Rofeh

Acknowledgements

I am thankful to many people who have played a role in supporting me and my research. I am most thankful to my advisor, Prof. Luke Theogarajan for his generosity and genuine caring. The questions and answers that arose from our many discussions were both an engine and rudder for our research. These discussions are also great memories that I will cherish.

I am also thankful to the UCSB Biomimetic group for its culture of collaboration and support: Dr. Avantika Sodii, Dr. Sukru Yemenicioglu, Dr. Samuel Beach, Sarah Grundeen, Dr. Shahab Mortezaei, Dr. Danielle Morton, Aaron Bluestone, Dr. Melika Payvand, and Dr. Prajakta Kulkarni. Shahab and Danielle established the groundwork for my work with polymer membranes. Specifically, Shahab synthesized the triblock copolymer used throughout this work and Danielle established methods for membrane formation and electrical measurement that I used as a starting point. They also directed me to interesting research questions when I began my work on membranes. Sam, Avantika, and Sukru were always helpful in navigating earlier research projects (not included in this thesis) that relied more heavily on nanofabrication. In an early MURI project, Avantika's integration and planarization work was crucial to my work on vertical integration of memristors onto CMOS. On a personal level, lunches with Sukru and dinners with Avantika are great memories from my time in Santa Barbara.

Outside of the Biomimetic group, I am thankful to Dr. Mike Stanton for teaching me experimental technique and Prof. Andrew Cleland for teaching me how to approach bioengineering as a physicist in my first months as an experimentalist. I would also like to thank Prof. Philip Pincus and Prof. Deborah Fygenson for their involvement in my committee. In particular, I am thankful to Deborah for our many memorable meetings and her valuable insights.

Outside of UCSB, I would like to thank Prof. Jens Gundlach for providing mutant MspA and Dr. Jeffrey Fisher and Steve Schankweiler at Illumina for developing the microfluidic membrane painting system used in this work. I am also grateful to the worldwide scientific community for giving attention to the emails of a stranger. In particular, my correspondence and conversations with Dr. Graham J. Taylor (at T&T Scientific) were invaluable as I transitioned to using the droplet interface bilayer technique. In this spirit, I welcome anyone with a curiosity in my work to contact me.

Others supported me by giving my life balance away from work. I will cherish memories with Rich Sander, Kate Wheeling, David Shultz, Andrew Schaeffer, Ted White, Gavin Hartnett, Mishel George, Nicole Iannaccone, Bugra Kaytanli, Jonathan Gardner, Amit Vainsencher, Willow Sprout, Kevin Malta, Darcey Elliot, and Trey Suntrup. I am especially thankful to Trey for his friendship over the years. Our Sunday morning Fareed Zakaria viewings with Darcey made Santa Barbara feel like home. Finally, I am grateful to my family and friends outside of Santa Barbara for being there for me, always.

Curriculum Vitæ

Justin Daniel Rofeh

Education

2017	Ph.D. in Physics, University of California, Santa Barbara
2013	M.A. in Physics, University of California, Santa Barbara
2008	B.S. in Physics, University of California, San Diego

Publications

Abarbanel, H.D.I., P. Bryant, P.E. Gill, M. Kostuk, J. Rofeh, Z. Singer, B. Toth, and E. Wong. "Dynamical parameter and state estimation in neuron models." The dynamic brain: an exploration of neuronal variability and its functional significance (2011).

Payvand, M., J. Rofeh, A. Sodhi, and L. Theogarajan. "A CMOS-memristive self-learning neural network for pattern classification applications." In Nanoscale Architectures (NANOARCH), 2014 IEEE/ACM International Symposium on, pp. 92-97. IEEE, 2014.

Rofeh, J., A. Sodhi, M. Payvand, M. A. Lastras-Montao, A. Ghofrani, A. Madhavan, S. Yemenicioglu, K.-T. Cheng, and L. Theogarajan. "Vertical integration of memristors onto foundry CMOS dies using wafer-scale integration." In Electronic Components and Technology Conference (ECTC), 2015 IEEE 65th, pp. 957-962. IEEE, 2015.

Payvand, M., A. Madhavan, M. A. Lastras-Montano, A. Ghofrani, J. Rofeh, K.-T. Cheng, D. Strukov, and L. Theogarajan. "A configurable CMOS memory platform for 3D-integrated memristors." In Circuits and Systems (ISCAS), 2015 IEEE International Symposium on, pp. 1378-1381. IEEE, 2015.

Rofeh, J., and L. Theogarajan. "Shape analysis for real-time tension measurement in droplet interface bilayers." In preparation.

Rofeh, J., and L. Theogarajan. "Droplet interface bilayers from insoluble block copolymer monolayers." In preparation.

Abstract

Block Copolymer Membranes for Protein Nanopore-Based Biosensing

by

Justin Daniel Rofeh

Model membranes are synthetic structures that mimic cell membranes. They may be used for basic research or as part of an engineered device. Phospholipids are typically used to make model membranes, but they may be replaced by amphiphilic block copolymers that are more physically and chemically stable, more tunable, and less costly. In this work, we explore the use of block copolymer membranes for biosensing applications. Specifically, we target the goal of nanopore DNA sequencing using the protein nanopore MspA in block copolymer membranes.

As a first step, we extended previous work on MspA in a block copolymer membrane by translating it to an array of apertures using a microfluidic painting technique. We found that the use of a volatile solvent in a microfluidic channel caused variations in membrane properties with corresponding undesirable variations in MspA behavior. Additionally, we used this method to demonstrate DNA translocation through MspA in block copolymer membranes. We selected droplet interface bilayers (DIBs) to investigate which membrane properties are responsible for variations in MspA behavior. However, we found that our aqueous block copolymer DIBs behave differently than any previously studied DIB, necessitating the use of new techniques to characterize their behavior. Key differences include reduced bilayer stability due to poor packing of the monolayer and slow equilibration kinetics. We addressed the poor bilayer stability by establishing a technique for manually packing monolayers prior to bilayer formation. We addressed the slow equilibration kinetics by establishing a new method for measuring monolayer and

bilayer tensions in DIBs using droplet shape analysis. While droplet shape analysis is typically used for single droplets with axial symmetry, our method works even for DIBs with asymmetric volumes and tensions. Another advantage is that the method can determine monolayer and membrane tensions in real time, independent of the applied voltage. The method may be used for polymer and phospholipid DIBs alike. The work presented in this thesis contributes to the understanding of amphiphilic block copolymer behavior and will aid in the optimization of membrane properties for biosensing applications.

What I cannot create,

I do not understand.

— Richard Feynman

Contents

Chapter 1

Introduction

Two main thrusts are presented in this thesis. The primary thrust is the use of a block copolymer as a replacement for phospholipids in membranes. The secondary thrust is the use of block copolymer membranes specifically for the purpose of protein nanopore-based DNA sequencing. Both of these topics are relatively new and have only been reported in the literature in the last two decades. In this chapter, we will introduce and motivate the membrane techniques that are utilized in Chapters 3 and 4: aperture-suspended membranes and droplet interface bilayers. This includes an introduction to nanopore DNA sequencing.

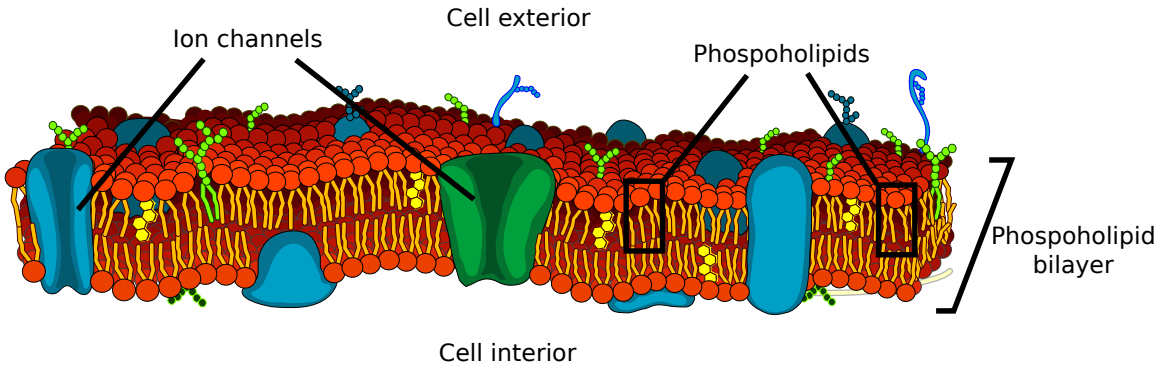

Figure 1.1: Illustration of a cell membrane with phospholipids and ion channel proteins indicated. All structures larger than phospholipids are proteins. These components, and many more not shown here, interact to produce the complex behavior of cell membranes.

1.1 Membranes, block copolymers, and protein nanopores

Cell membranes have a fundamental importance in biology. They not only separate cells from their surroundings but are also involved in cell signaling, the regulation of cell interiors, and cell adhesion [1]. Cell membranes are complex structures composed of lipids and proteins, as shown in Figure 1.1. The importance of membrane proteins is such that the genes that make them comprise 20-30% of genes in most genomes [2], including humans [3], and membrane proteins comprise about half of all drug targets [4]. To an extent, membrane lipids are responsible for structural properties while proteins are responsible for functional properties; however, this division is not absolute. One way membrane lipids affect function is by their effect on proteins through their physical interaction [5]. The effect of membranes on the proteins that reside in them is one of the focuses of this thesis.

One approach to cell membrane research is to perform observations or experiments on cells. These experiments often involve small perturbations to elucidate their behavior, for example by altering the environment outside the cell or by genetically modifying a

protein that is present in the membrane. Another approach to cell membrane research is to use model membranes to investigate one or a few components of a cell membrane in isolation. Model membranes are synthetic structures that mimic the behavior of the phospholipid bilayers of cells, so that they often allow for analyses and insights that are difficult to achieve in cell experiments. These experiments have provided important information about both lipids and membranes. For example, model membranes composed of phospholipids have allowed for the determination of their phase behavior [6], thickness [7, 8], tension [9, 10], and properties of bilayer formation [11]. Additionally, proteins are often introduced to the membranes to investigate their behavior and how it is affected by membrane composition [12].

In addition to their importance to basic research, these membranes are the system of choice for the growing field of protein nanopore-based biosensors. Nanopore-based biosensors use the analysis of current through a protein nanopore to sense molecules. The molecules of interest range from small molecules to macromolecules, and can be synthetic or of natural origin. Among other possibilities, the measurements may be used to determine concentration as in the case of cocaine [13], molecular weight as in the case of synthetic polymers [14], or the sequence of nucleotides in DNA [15].

In this engineering context, membranes may be composed either of natural surfactants such as phospholipids or of synthetic surfactants that mimic their behavior. Amphiphilic block copolymers are synthetic surfactant molecules that can have certain advantages over phospholipids depending on their synthesis: they are generally cheaper to produce; they have improved chemical stability[1]; they can be more electrically and physically robust [16, 17]; and they have a wider range of properties than can be tuned according to their synthesis [18, 19]. It is for these reasons that they hold promise for commercial

[1]Phospholipids must typically be stored in a freezer at -20°C while copolymers can typically be stored at room temperature.

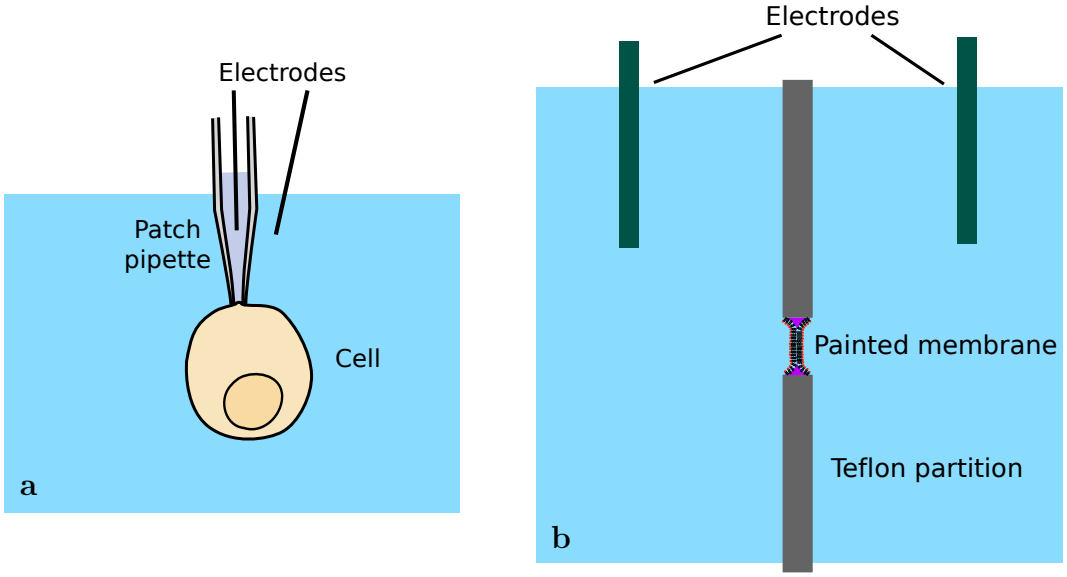

Figure 1.2: Illustration of (a) a patch clamp experiment on a cell and (b) a painted bilayer experiment. In both experiments, an electrochemical measurement is made over the membrane to investigate its behavior. In a painted bilayer, the experimenter has full control over the membrane components.

applications. However, prior to their use they must be tailored for each protein of interest. This process can be time consuming [18, 20] because block copolymer membranes are relatively new and uncharacterized, and also because the desired membrane properties for a particular protein are often not known. Additionally, we will see in this thesis that block copolymers can behave in ways that differ significantly from phospholipids.

In their use with membranes, protein nanopores can be used as they are found in nature or they can be modified by genetic engineering if a suitable protein nanopore does not exist for an application. Protein nanopores are chosen for their ability to pass a current that responds to some stimulus. The two most frequently used protein nanopores are ion channels and pore-forming proteins. Ion channels are ion-selective nanopores that are present in all cells. They play a role in establishing electrochemical gradients across membranes, whereby they are responsible for important functions such as electrical signaling (including signals between neurons) and energy metabolism [1]. They

can be naturally responsive to stimuli such as heat, mechanical stress, and a variety of chemicals [21]. Pore-forming proteins are proteins that form pores in cell membranes [22]. Their pores are larger than ion channels, making them nonselective or less selective to ions. Pore-forming proteins include pore-forming toxins that cause cell death by creating unrestricted leaks in cell membranes, such as α-Hemolysin. They also include porins that are present in the membranes of many bacteria and other organisms, which are responsible for transport by passive diffusion; one example is Mycobacterium smegmatis porin A (MspA), which is used in this work.

1.2 Membranes for research and protein nanopore-based biosensing

There are many types of techniques for making membranes, each with particular benefits and limitations [23]. These include giant unilamellar vesicles [24, 25], supported membranes [26, 27], droplet interface bilayers [28] and aperture-suspended membranes [12]. In our case, we desire a membrane system that is amenable to protein nanopore-based sequencing. Supported membranes cannot be used because they rest directly on a substrate so that translocation is impeded. Giant unilamellar vesicles could be used, but transmembrane electrical measurements necessitate patch clamping [29, 30], which is known to be complicated and laborious [31]. Alternatively, aperture-suspended membranes and droplet interface bilayers are both naturally suited for transmembrane electrical measurements due to the ease of accessing reservoirs on either side of the membrane with electrodes. For this reason, we chose them for use in our research. Here, we briefly review the history of model membranes, focusing on aperture-suspended membranes and droplet interface bilayers. Additionally, we motivate our choice of droplet interface bilayers in particular in Chapter 4. Finally, we describe and motivate the use of automated and arrayed devices.

Aperture-suspended membranes

The first cell membrane mimics were lipid bilayers reported in 1962 in a paper by Mueller and Rudin [32]. They described the use of a lipid painted on an aperture in an aqueous environment (Figure 1.3). Mueller and Rudin used the membrane to reconstitute a voltage-gated ion channel to demonstrate the membrane's ability to replicate behavior that was until then unique to cell membranes. In their protocol, a dispersion of lipid in a volatile solvent is first painted on the rim of the aperture and allowed to dry in air [33].

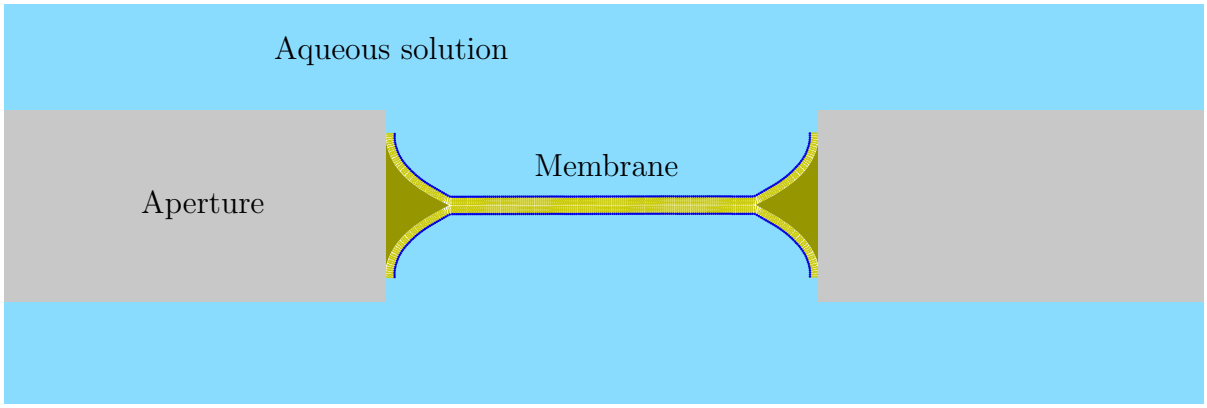

Figure 1.3: Illustration of a painted bilayer membrane in an aqueous solution. An electrode on either side of the membrane can be used for electrochemical measurements.

Then the aperture is submerged in aqueous solution. Finally, a "brush" composed of some inert material such as Teflon is used to paint a small amount of lipid in solvent over the aperture. The membrane spontaneously thins, first due to suction due to the Laplace pressure at the border[2], and then due to adhesion of the monolayer leaflets[34]. In a variation of the Mueller-Rudin approach by Szabo et al. [35], the lipid solution is introduced to the aperture using a pipette and bubbles are dragged over the aperture to form membranes. This is the manual approach most similar to the automated approach that was used in Chapter 3.

In 1972, Montal and Mueller [36] developed an approach which allowed for the creation of asymmetric bilayers. In their approach, they first spread a monolayer over the surfaces of two troughs separated by a partition with an aperture. The water level of the troughs is initially below the aperture so that, by raising the level in each trough independently, an asymmetric bilayer is formed as shown in Figure 1.4. This is important because membranes in all eukaryotic cells and potentially all prokaryotic are asymmetric [37, 38]. For example, the Montal-Mueller approach has been used successfully to model the asymmetric outer membrane of Gram-negative bacteria to better understand how they

[2]This process is illustrated in more detail in Section 2.4.

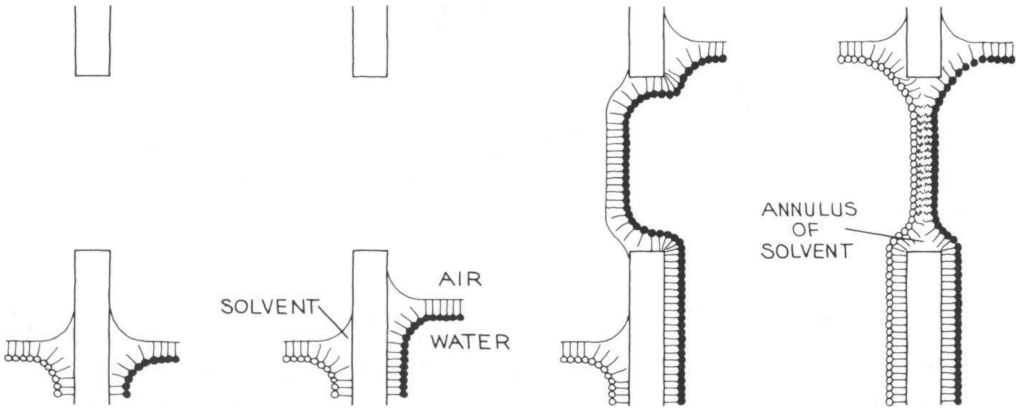

Figure 1.4: Illustration of the Montal-Mueller technique described in the text. Source: White et al. [42]

function [39, 40]. It has also been used to model the formation of lipid domains (rafts) in asymmetric membranes [41].

Droplet interface bilayers

In 1966, Tsofina et al. demonstrated the first droplet interface bilayers (DIBs), bilayers which are formed by the contact of two monolayer-covered aqueous droplets surrounded by oil [43]. With the exception of few researchers such as Michaels and Dennis, who in 1973 used DIBs to form asymmetric bilayers [44], the approach went largely unnoticed from its discovery until 2005 when it was popularized by Bayley's group [28]. The approach is versatile: the formation of monolayers can be achieved by the presence of surfactant in either the oil phase or the water phase. One major benefit of DIBs is the ease of making asymmetric membranes, which can be achieved simply by dispensing droplets with differing surfactants. DIBs can be formed in either a vertical or horizontal configuration, as shown in Figure 1.5. In the vertical configuration, a small aqueous droplet is lowered onto a larger aqueous pool or hydrogel beneath it. In the horizontal configuration, two droplets may be suspended on the tip of electrodes, but alternatively they may reside in a microfluidic channel [45] or they may be dispensed by capillar-

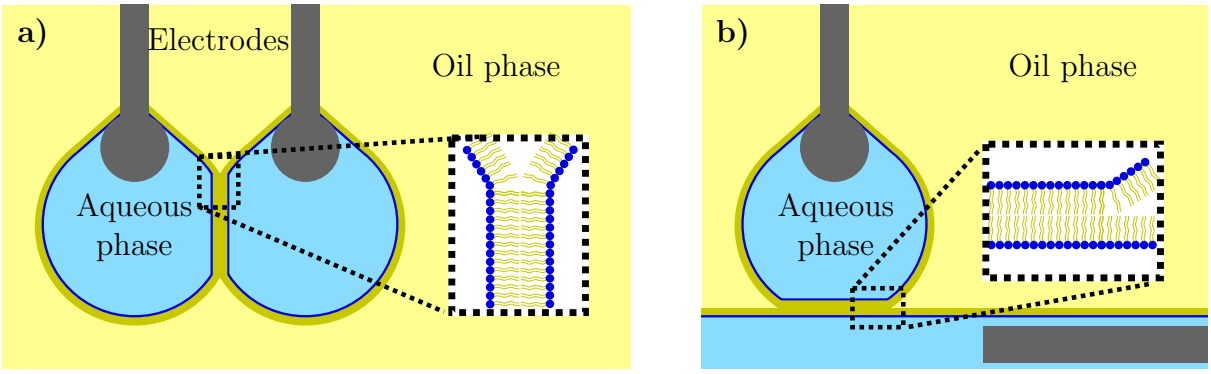

Figure 1.5: Side view of a droplet interface bilayer experiment in a horizontal configuration (a) and a vertical configuration (b). First a monolayer of surfactant is formed on each droplet. Then the monolayers are contacted to form a bilayer. For the vertical configuration, a microscope views the experiment from the bottom so that the bilayer area is visible as a circle. A hydrogel may be used to make the bilayer planar. Phospholipids are shown but block copolymers may be used instead. Diagrams adapted from Refs. [8] and [48].

ies [46]. Other major benefits of droplet interface bilayers include their versatility and ease of use [47].

Using membranes to determine bilayer thickness and tension

There are several properties of membranes that are known to have an effect on protein behavior, including thickness, tension, fluidity, and spontaneous curvature [5, 49]. Our interest in these properties arises from results that will be presented in Chapter 3: notably, the behavior of the protein nanopore MspA in block copolymer membranes exhibits a strong dependence on membrane preparation. This dependence is important because in most cases it causes the MspA to behave in a way that prevents its use in DNA sequencing. This motivates our desire to investigate the properties of the block copolymer membranes in Chapter 4. We focus our attention on membrane tension and thickness because methods exist for measuring them in situ during transmembrane electrical measurements.

The most common method for determining membrane thickness is by determining its

specific capacitance. This is done by imaging the membrane to determine its area and simultaneously performing a capacitance measurement over the membrane. Then, from the formula for a parallel plate capacitor, the specific capacitance is $C = \epsilon/h$, where h and ϵ are the thickness and dielectric constant of the hydrophobic region. This method is straightforward and has been used in both aperture-suspended membranes [7] and droplet interface bilayers [8].

The determination of membrane tension is less straightforward. A common method is to use geometric measurements. Requena and Haydon [11] established a method for determining tension in a variation of an aperture-suspended membrane on a microscope stage. They used the interference fringes of a lens of oil trapped in a bilayer to calculate the contact angle between the monolayers at each voltage. The relation between contact angle and voltage provides the monolayer and bilayer tension if the specific capacitance is known, as will be described in Section 2.5.

A different method for determining membrane tensions was reported recently by Beltramo et al. [9]. They use confocal microscopy with fluorescent particles on the interface of an aperture-suspended membrane to determine the curvature of the monolayer that supports it. By concurrently measuring the pressure difference over the monolayer, they determined its tension using the Young-Laplace equation, which will be derived in Section 2.4. The monolayer tension was used to determine the bilayer tension.

DIBs in both the vertical and horizontal configurations can also be used to determine thickness and tension. Gross et al. used a droplet-on-hydrogel bilayer to determine membrane thicknesses for different oils [8]. In this vertical configuration, the bilayer area is visible as a circle, allowing for an accurate measurement of the area. Additionally, they reported that bilayer tension can again be estimated by determining the relation between

contact angle and voltage[3]. More recently, the horizontal configuration has been used by Taylor et al. [10] to image the bilayer contact angle directly. Again the relation between contact angle and voltage was used to determine tension. For membrane thickness measurements, the interfacial area is viewed edge-on in the horizontal configuration, so that its diameter can be determined. However, the bilayer is stretched due to the effect of gravity on droplet shape, so that determining the bilayer area requires a correction factor. Due to the angles from which imaging is performed (head-on vs edge-on), it is probable that the vertical configuration provides more accurate area and membrane thickness measurements, while the horizontal configuration provides more accurate angle and bilayer tension measurements[4].

While other methods exist[5], we aimed to emulate the DIB approach of Taylor et al. [10] in Chapter 4 to determine bilayer tensions for its relative ease of use [28] and the availability of a detailed protocol for droplet interface bilayers [47]. DIBs require a minimal initial cost due to their use of simple materials and common laboratory equipment. In our case, a microscope, micropositioners, a patch clamp amplifier, and suitable surfactants were already available in the lab, so that the only materials missing to start experiments were silver wire and agarose.

Automated and arrayed devices

Most membrane techniques are compatible with automation and arraying, which serve to increase the throughput and consistency of measurements. Since these are both re-

[3]See the supporting material in Ref. [8]. In this configuration, they used the bilayer and droplet radius to estimate the contact angle assuming a spherical droplet.

[4]However, the accuracy of contact angle measurements using horizontal DIBs decreases for small contact angles [50]

[5]For example, the method of Takei et al. uses laser-induced surface deformation spectroscopy to determine bilayer tension, which requires a complex apparatus [51]. The method of Petelska et al. uses the shape of the bulge of a bilayer under a hydrostatic pressure to determine bilayer tension using the Young-Laplace equation, which cannot scaled down to a desirable membrane area [52].

quirements for the commercialization of technologies such as nanopore DNA sequencing, the use of an automated and arrayed membrane formation system is explored in Chapter 3. For a fully parallel system, each unit of the array must include an electrode, an aperture or sealing mechanism, and a well to hold the measurement solution and insulate the electrode from the other units in the array. Several groups have reported such arrays for aperture-based systems [53, 54, 55, 56, 57, 58]. For example, Hirano-Iwata et al. [58] created a 3×3 aperture array on which they deposited membranes by the Montal-Mueller approach. Notably, Baaken et al. [55] demonstrated the use of a planar microelectrode-cavity array for BLMs, painting the apertures manually but simultaneously with a piece of PTFE. Their system has the additional benefit of scalability, due to the ability to photolithographically pattern all elements on a planar chip. This allowed for their commercialization so that their microelectrode-cavity arrays are available for purchase as part of an easy-to-use automated painting system (Ionera). With cost and scalability in mind, we too use a photolithographically-patterned system in Chapter 3.

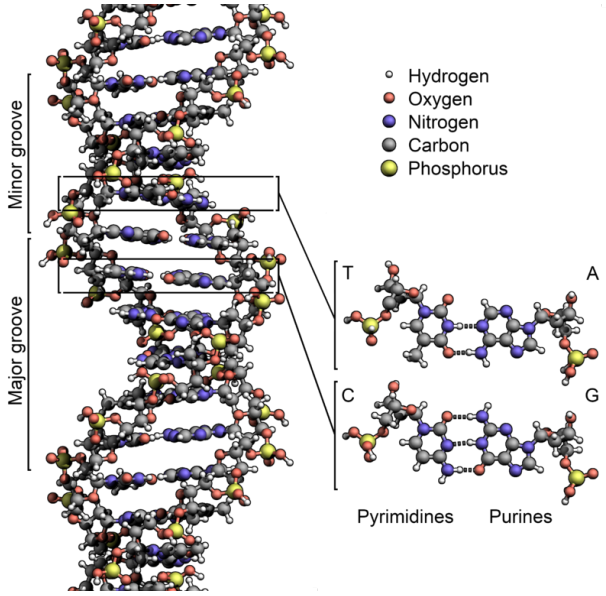

Figure 1.6: Atomic scale illustration of the DNA double helix. The four bases guanine, adenine, thymine, and cytosine are labeled G, A, T, and C. Credit: Richard Wheeler under a Creative Commons license [59]

1.3 Motivations for nanopore DNA sequencing

DNA is a polymer molecule that is essential to all known organisms [1]. As illustrated in Figure 1.6, it is composed of two separate strands which bond to form a double helix. Each strand is comprised of a sequence of four nucleotides that are distinguished by their bases: guanine, adenine, thymine, and cytosine. The sequence of bases encodes the instructions that are used for the function and reproduction of all cells. DNA is passed from one generation to the next so that it is responsible for heredity.

DNA sequencing is the determination of the sequence of bases in DNA. Due the importance of DNA to biology, DNA sequencing has a high potential for use in medicine. It is estimated that variants of single genes are responsible for disease in approximately 1% of births [60]. Many more common diseases such as heart disease [61], diabetes [62], and cancer [63] are known to have a more complex genetic link that depends on multiple genes as well as environmental effects. Some of these links have already been discovered. For

example, around 60% of women with a known mutation of the BRCA1 gene will develop breast cancer before the age of 70 [64]. As the understanding of the human genome improves, DNA sequencing will continue to have increasing clinical relevance [65].

There are many medical applications of DNA sequencing other than the analysis a person's genome. For example, DNA sequencing is increasingly being used to diagnose cancer subtype, which is used to inform treatment [66, 67]. Another example is the analysis of the microbiome, the 10,000 or so species of bacteria that present in a given person. Research on the microbiome is still in the very beginning stages: DNA sequencing is being used to determine which bacteria are present in the human microbiome, which might possibly play a significant role in conditions such as diabetes and obesity [68, 69]. Yet another example is the field of epigenetics, which is concerned with the expression of genes: while DNA stores the genes, epigenetics controls to what extent genes are activated [70, 71]. One mechanism of epigenetics is the addition of a methyl group to some of the cytosine groups in DNA, which can be discerned from the four bases using nanopore sequencing [72]. Considering the novelty of all of these fields, it is difficult to predict how important they will be. But extrapolating from what is already known in the reviews cited in this paragraph, the potential is massive [73].

This high potential of DNA sequencing has driven efforts reduce cost and improve speed. This goal is being met at an astounding pace: while sequencing a genome cost ~$10 million in 2006, it costs ~$1,000 today [74, 75]. Concurrently, the speed and throughput of methods have similarly improved [74]. These improvements have accompanied the transition from first-generation DNA sequencing technologies such as Sanger sequencing to second-generation sequencing technologies such as Illumina's Solexa technology. Now there are many so-called third-generation technologies vying to reduce cost and time even further, some of which have been commercialized [76].

Most commercial DNA sequencing technologies that are available today are second-

generation technologies, which are comprised of four steps [65]. The first step is the preparation of the material to be sampled, which, for example, could originate from blood or saliva. In this step the DNA is extracted and used to prepare a library of DNA fragments for the next step. The second step is called amplification, where the DNA fragments are duplicated. This is necessary to create a signal strong enough to be detected. For example, Illumina's Solexa technology uses fluorescent detectors, where clusters of identical DNA fragments are used to create a detectable fluorescent response. The third step is measurement, which is parallelized to increase speed. Enough overlap must exist between adjacent strands of DNA so that the entire library of fragments can be pieced together. The read length, the number of bases read consecutively in each fragment DNA, is an important parameter which is typically limited because most methods have an error rate that increases with the number of bases read. The last step is data analysis, which is not trivial due in part to the large amount of fragments that must be pieced together.

Each of these steps contributes to both the cost and time of DNA sequencing. Nanopore DNA sequencing, like other third-generation technologies, could reduce the cost and time of each of these four steps. DNA could be read without modification, cutting down significantly on preparation costs. Additionally, because it is based on single-molecule measurements, the error rate is independent of read length, allowing for much larger consecutive reads. This eliminates the need for DNA amplification and reduces the computation time for piecing together a whole sequence [77, 65].

It is likely that second-generation technologies will continue to improve also. For example, Illumina has recently predicted that its newest machine will eventually cost $100 per genome [78]. If they succeed, nanopore sequencing could still offer benefits such as portability and lower capital cost. At the time of this writing, Oxford Nanopore Technologies' handheld MinION sequencer costs $1,000 [79], in comparison to Illumina's

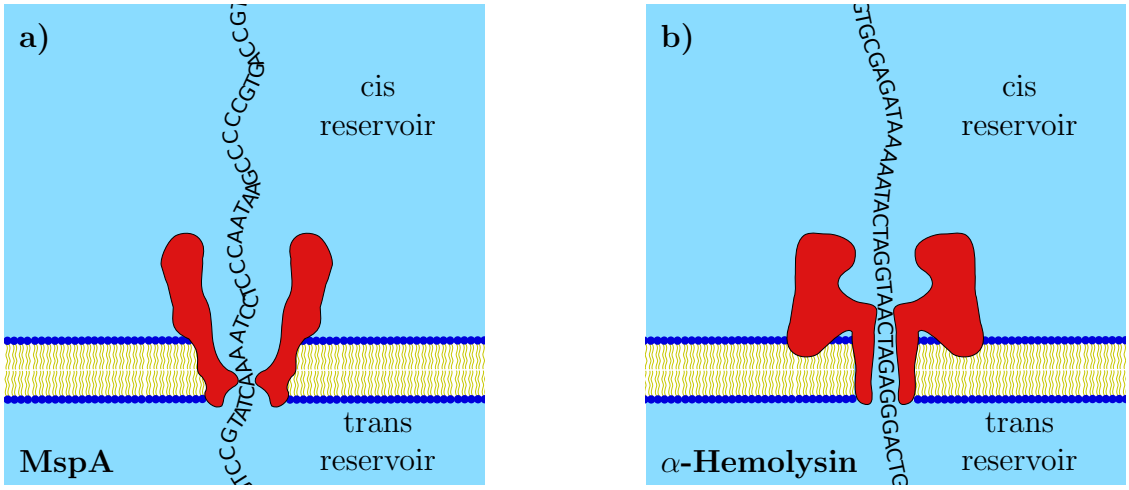

Figure 1.7: Illustration of nanopore DNA sequencing using MspA (a) and α-Hemolysin (b) nanopores. A positive voltage is applied to the cis reservoir relative to the trans reservoir to drive the negatively charged single strand of DNA through the nanopore. The resulting current is analyzed to determine the sequence. For both nanopores, the constriction is barely wider than the DNA, but the constriction is much shorter for MspA; this results in a greatly improved ability to discern bases using the current signal in MspA.

least expensive sequencer, the MiniSeq, a tabletop sequencer that costs $49,500 [80].

1.3.1 Nanopore DNA sequencing

Nanopore sequencing uses an applied voltage to drive single-stranded DNA through a nanopore, as shown in Figure 1.7. The nanopore diameter is close to the ~1-nm diameter of DNA, so that the differences between the four bases contribute to distinct levels of current through the nanopore. The best results to date have been with proteins because they reproducibly fold into the same structure with atom-scale precision. Solid state, synthetic nanopores have also been made, but the fabrication of nanopores of the desired dimensions has been a major obstacle [81].

The first successful translocation of DNA through a nanopore was demonstrated in 1996 using the protein nanopore α-Hemolysin [82] (Figure 1.7b). Early experiments with α-Hemolysin revealed that single-nucleotide resolution was limited by both short,

poorly-controlled translocation times and nonideal nanopore geometry [15, 81]. Membranes have increasing noise at higher frequencies arising from the capacitance of the membrane and the system as a whole [81]. Because the signal strength (the magnitude of current changes associated with translocation) is independent of the translocation time, the signal-to-noise ratio decreases with shorter translocation times. Thus, in practice there is a maximum frequency at which bases can be discerned based on practical system limitations, so that the DNA must be slowed down. Additionally, to discern multiple consecutive repeats of the same base, it would be beneficial to have a system that steps DNA through in a controlled manner, one base at a time. The pore geometry is important because it effects the spacing of current levels associated with different sequences of bases. α-Hemolysin has a 5-nm long constriction region so that the current is a reflection of over 10 bases at a time. The small differences in current between the different combinations of bases makes sequencing in this case impractical.

Since the 1990s great progress has been made to resolve both of these issues. Following the discovery of MspA, Gundlach identified it as a superior candidate for sequencing due to its ~1 nm constriction length [15]. His group performed two sets of mutations on MspA [83]. First, they converted negatively-charged amino acids to positively-charged amino acids at the site of the constriction so that they would not repel negatively-charged DNA. This was successful in allowing for the translocation of DNA. Second, they performed similar mutations from negative to positive charge in the vestibule of the protein, further from the constriction, thereby increasing the capture rate of DNA from solution. It is this mutant of MspA, referred to as M2MspA by Butler et al. [83], that is used exclusively in our research in Chapter 3.

In 2010 Lieberman et al. showed that a phi29 DNA polymerase could be used to slowly ratchet DNA through α-Hemolysin [84]. Using this method, the Gundlach group slowed DNA translocation through M2MspA to show that the current through it depends

on ~4 nucleotides at a time, with the majority of the signal arising from one or two nucleotides [85]. This allowed single-nucleotide polymorphisms in a DNA sequence to be detected with 77% accuracy [86]. After exploring similar technologies in a parallel string of developments [87], the portable nanopore sequencing-based device MinION, which is commercially available from Oxford Nanopore Technologies, has been shown to have single-nucleotide accuracy of over 85% [88]. With repeated readings, accuracy increases to above 99% [15]. Accuracy remains the primary impediment to the widespread use of nanopore sequencing.

1.4 Outline of this thesis

In Chapter 2, we will describe some of the theory that is relevant to membranes. The physics of surfactant aggregates and of monolayers and bilayers will help us interpret the behavior of both planar membranes in Chapter 3 and DIBs in Chapter 4. In particular, the Young-Laplace equation is critical to the droplet shape analysis that will be performed in Chapter 4.

In Chapter 3, we will present the results of experiments using MspA as a nanopore in a block copolymer membrane. The membranes are made on an array of apertures using a microfluidic painting technique. The method causes variations in the behavior of MspA that do not occur in the manual-painting method established by previous members in our group. We investigate the source of these variations and show that they originate primarily from changes in solution composition. Additionally, we will use the method to demonstrate DNA translocation using MspA.

In Chapter 4, we will present the results of experiments performed using the same block copolymer in DIBs. The DIB method was chosen as a simple way to determine the tension of the block copolymer membranes. However, the DIBs behave in a manner that is different enough from phospholipid DIBs that the intended methods cannot be used. Specifically, the block copolymer we use does not adsorb to form a packed monolayer on its own. Additionally, once stable bilayers are formed, they are so slow to reach equilibrium that the relation between contact angle and voltage cannot be used to determine membrane tension. To circumvent these issues, we demonstrate a technique for manually packing monolayers to form stable polymer bilayers. We also establish a new method for measuring monolayer and bilayer tensions in a DIB using droplet shape analysis based on the Young Laplace-equation. The method has the advantage that it can determine tensions in real time, independent of the applied voltage.

Chapter 2

Theory

2.1 The thermodynamics of interfaces

As we discussed in Chapter 1, interfacial tension is an important parameter in membranes. In our case, it is important because the interfacial tension in a bilayer may potentially cause the undesirable current fluctuations in MspA that we will see in Chapter 3. Additionally, bilayer tension can be directly related to the packing of amphiphiles in the bilayer, so that it determines bilayer stability [89]. Monolayer tension is similarly important to us because both aperture-suspended membranes and droplet interface bilayers begin with the formation of monolayers. Accordingly, the monolayer tension prior to bilayer formation determines the resulting bilayer tension. This will be relevant in Chapter 4 where the stability of DIBs formed by unassisted adsorption was poor due to the incomplete packing of our block copolymer in the monolayer. Additionally, the monolayers coexist with the bilayers after they are formed. This coexistence was exploited to make an experimental determination of the membrane tension using geometry in Chapter 4.

Similar to the thermodynamic definition of pressure as the change in energy due to

increasing volume, $P = \frac{\partial U}{\partial V}$, interfacial tension γ can be defined as the work required to change the surface area, $\gamma = \frac{\partial G}{\partial A}$, at constant temperature [90]. This explains the tendency of a droplet of water in air, with its constant, positive surface tension, to minimize its surface area, forming a sphere in the absence of gravity. γ can refer to surface tension at a liquid-gas interface or interfacial tension at a liquid-liquid interface.

The origin of γ is molecular, and to understand its origin, it is helpful to first consider the surface tension of a liquid without surfactant in contact with gas or vacuum. In order to increase the interfacial area, it is necessary to move molecules from the bulk to the interface. As an approximation, let us consider that all adjacent pairs of molecules in the liquid have an average interaction energy. Because molecules at the surface have fewer nearest neighbors, the total interaction energy of molecules at the surface is lower than that in the bulk. It is in essence this energy difference that is responsible for interfacial tension. More formally, this energy difference is described by the work of cohesion w_c of a liquid, which is defined as the reversible work per unit area done on a liquid to split it in two [91]. Because two surfaces are created, it is related to surface tension simply as $w_c = 2\gamma$.

The tension at the interface between two liquids has an additional contribution to the work of cohesion: the work of adhesion, which arises from the molecular interaction between molecules across the interface. The work of adhesion is defined as the reversible work per unit area done on the system to separate the two liquids at an interface [91]. Including this contribution, the interfacial tension can be described by:

$$\gamma_{12} = \frac{1}{2}(w_{c,1} + w_{c,2}) - w_{a,12}.$$

Interfacial tension is always positive (and hence tensile) in equilibrium because if the work of cohesion were negative, the interface would not be stable.

The interfacial tension between liquids cannot be changed by any external means except those that affect the composition of the interface. At an oil-water interface, the introduction of surfactant molecules acts to lower interfacial tension by increasing the work of adhesion between the liquids. Surfactants are typically amphiphiles, which have both hydrophilic and hydrophobic regions. They increase the work of adhesion by orienting along the interface and providing molecular groups that satisfy both liquids, so that the interaction energy of molecules is not much different at the interface than in the bulk. In general, denser packing of a surfactant is associated with lower interfacial tension because it reduces the less favorable interactions between the adjacent phases.

Interfacial tension can alternatively be described using a mechanical formalism, so that for a planar interface

$$\gamma = \int_{z_1}^{z_2} \left[P_{\text{ext}} - \mathbf{P_T}(z) \right] dz \tag{2.1}$$

where the z coordinate runs perpendicular to the interface, the integration is performed over the thickness of the interface, P_{ext} is the pressure outside the interface, and $\mathbf{P_T}(z)$ is a tensor describing the pressure in the transverse direction within the plane of the interface as a function of height [92]. This formalism provides additional insight for thicker interfaces such monolayer and bilayers, where the intermolecular forces between adjacent molecules vary obviously as a function of height, contributing to $\mathbf{P_T}(z)$. This makes it clear that the reduction of free energy in the interface also depends on energetically favorable interactions between molecules in the plane of the interface. This formalism emphasizes that the tension is a mechanical property that exerts measurable forces in the plane of the membrane. It shows how even a tensionless bilayer may exert forces on a protein that affect its function if positive and negative values of $\mathbf{P_T}(z)$ cancel out [5].

2.1.1 Bilayer formation

The bilayers used in this work begin with the formation of monolayers which are then joined. Prior to joining, the water/oil/water structure may be treated as two separate oil/water interfaces, with the total free energy of the interface equal to the sum of each individual monolayer. As the monolayers approach each other, they begin to interact as the distance between them approaches ~100 nm. This interaction pushes the oil out from between the monolayers and a bilayer is formed [34, 93]. Once the bilayer is formed, it may be considered to be a single interface that is characterized by a single interfacial tension, γ_{b}. The difference in interfacial tension between the bilayer γ_{b} and the two monolayers γ_{m} is the free energy of bilayer formation per unit area [94]:

$$\Delta A = \gamma_{\mathrm{b}} - 2\gamma_{\mathrm{m}}$$

When a bilayer is formed by the adhesion of identical monolayers, a balance of tensions occurs, so that the vector components of the monolayer tensions and bilayer tension are in balance. If the two monolayers are not identical so that they have unequal tensions γ_{L} and γ_{R}, they may form an asymmetric bilayer. The in-plane components give[1]

$$\gamma_{\mathrm{b}} = \gamma_{\mathrm{L}} \cos\theta_{\mathrm{L}} + \gamma_{\mathrm{R}} \cos\theta_{\mathrm{R}} \tag{2.2}$$

where θ_{L} and θ_{R} are the angles between the left or right monolayer and the plane of the bilayer, as shown in Figure 2.1 [96]. This relationship derives from the minimization of free energy at an interface [95]. For identical monolayers, $\gamma_{\mathrm{L}} = \gamma_{\mathrm{R}} = \gamma_{\mathrm{m}}$, so that $\gamma_{\mathrm{b}} = 2\gamma_{\mathrm{m}} \cos\theta$. Equation (2.2) makes it possible to determine γ_{b} indirectly by the

[1] In some cases, local interactions surrounding the monolayer-bilayer contact line can have an associated free energy per unit length that comprises a line tension [95]. The presence of a line tension adds an additional term proportional to τ/r to Equation (2.2), where r is the radius assuming a circular contact area.

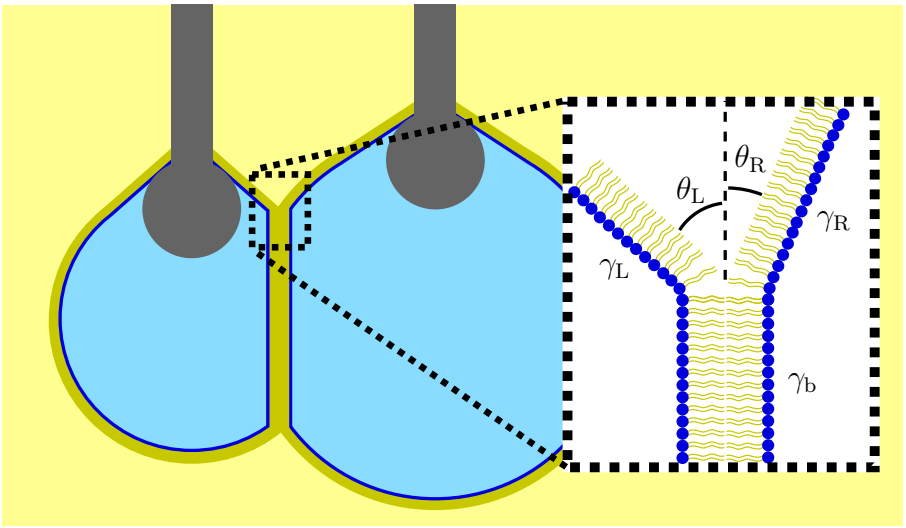

Figure 2.1: Illustration of quantities in 2.2 for an asymmetric droplet interface bilayer in the absence of a line tension.

measurement of contact angles and monolayer tensions, an approach we will use for the analysis of droplet interface bilayers in Chapter 4. Similarly, the out of plane components of the monolayer tensions are also balanced at equilibrium [96]:

$$\gamma_L \sin\theta_L - \gamma_R \sin\theta_R = 0 \tag{2.3}$$

These components act to pull apart or push together the monolayers, so that they are responsible for bilayer stability and changes in bilayer area [93].

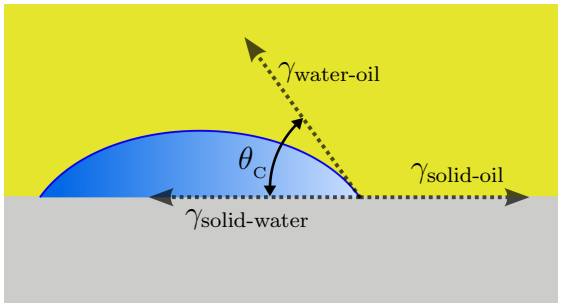

Figure 2.2: Illustration of the contact angle at the interface between oil, water, and a substrate.

2.1.2 Liquid-solid contact angles

In both aperture-suspended membranes and droplet interface bilayers, the bilayer is held in place by adjoining monolayers. The monolayers in turn are supported by a solid part of the apparatus. At the line of intersection between the oil, water, and substrate, the oil-water interface will make an angle relative to the substrate depending on the properties of each of the three interfaces, as shown in Figure 2.2. Just as in the case of liquid-fluid interfaces, the interface between a solid and a liquid is characterized by an interfacial free energy per unit area γ. In analogy to the liquid-fluid case, this arises from the energy difference resulting from the replacement of some of the liquid molecules' nearest neighbors by the solid. It can be derived [97, 98] from the minimization of free energy of the oil-water-substrate system that at equilibrium:

$$\gamma_{\text{solid-oil}} = \gamma_{\text{solid-water}} + \gamma_{\text{water-oil}} \cos\theta_{\text{C}} \tag{2.4}$$

This is known as Young's equation. The solid-oil and solid-water interface can be considered to apply virtual tensions that are in balance with the interfacial tension at the oil-water interface, just as in Equation (2.2). Ideally, the contact angle is independent of other system properties such as the force of gravity and droplet volume. However, more complicated effects such as line tension and hysteresis of the contact angle are often at

play due to nonidealities such as surface roughness or contaminants. Typically, θ_C may take a range of values and a more complicated analysis is required [90, 98].

2.2 Surfactant aggregates in solution

In contrast to most substances, which simply dissolve to varying extents in solution, surfactants often form multi-molecular aggregates. The aggregates form due to the cohesive interaction between surfactant molecules which originates from the hydrophobic or lyophobic interaction [90]. As a surfactant is added to water or oil, it dissolves as single molecules which begin to aggregate once the concentration crosses a threshold. This threshold concentration is called the critical micelle concentration (CMC) or the critical aggregate concentration.

The form of the aggregates depends on the surfactant properties. For small molecule amphiphiles such as lipids, the packing parameter $p = \frac{v}{al}$ provides a prediction of aggregate geometry. Here l and v are the length and volume of the hydrophobic tail and a is the area of the head group. Depending on the value of p, the aggregates are likely to be spherical micelles, cylindrical micelles, or vesicles, as shown in the top of Figure 2.3. For block copolymers, p is similarly predictive of aggregate geometry when l and v refer to the hydrophobic region and a refers to the hydrophilic region, as shown in the bottom of Figure 2.3 [100, 19]. Block copolymers will form spherical micelles, cylindrical micelles and vesicles[2] for similar values of p. Because the geometry of individual molecules is not known prior to performing experiments, the hydrophilic ratio $f = \frac{m_{\text{hydrophilic}}}{m_{\text{total}}}$ may be used to predict it, where $m_{\text{hydrophilic}}$ is the molecular weight of the hydrophilic group and m_{total} is the molecular weight of the total polymer [101]. Typically vesicles form for $25\% < f < 45\%$ and micelles form for $f > 45\%$. As we will see in Chapter 4, these values

[2]Block copolymers can also form more exotic aggregate types if their molecular weight is large enough [19]. This is not the case for the block polymer used in our work.

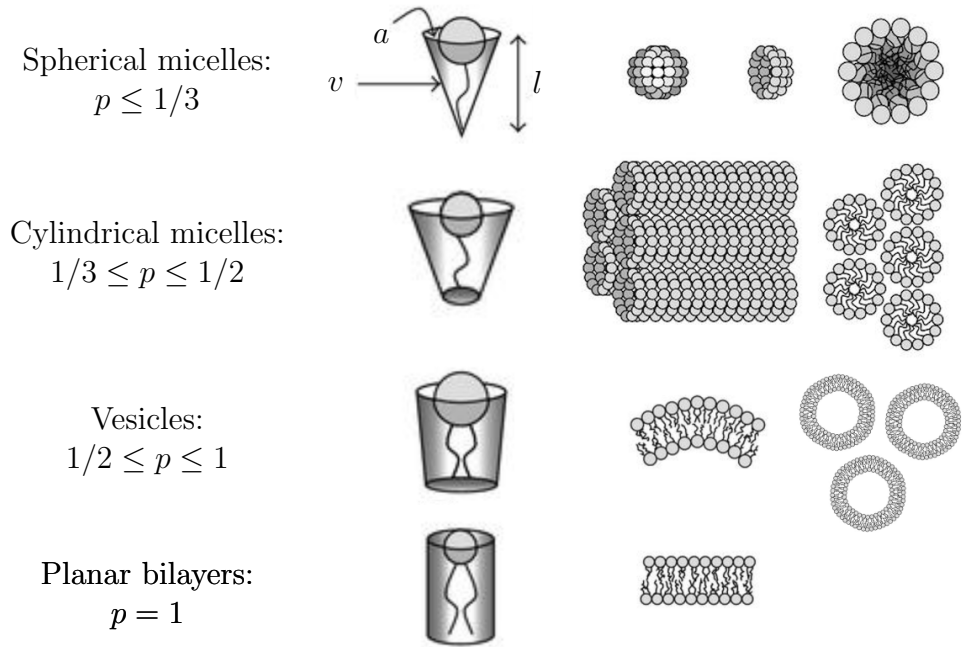

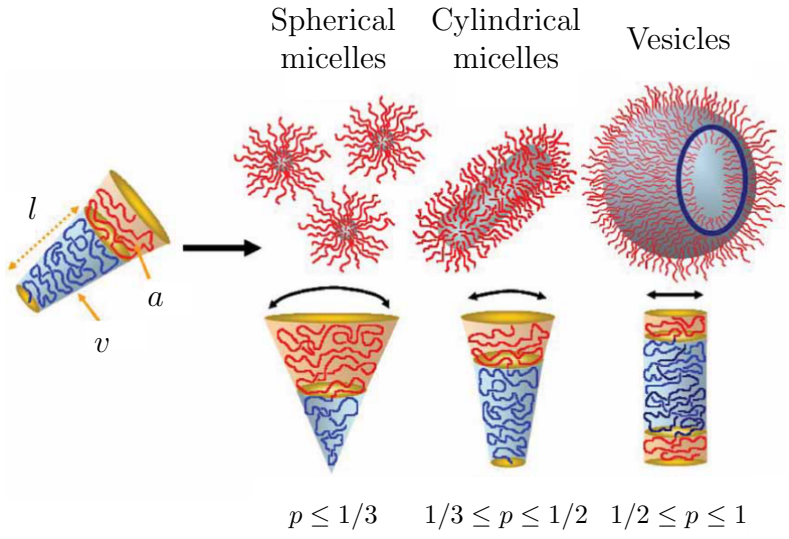

Figure 2.3: Dependence of lipid aggregates (top) and polymer aggregates (bottom) on packing parameter $p = \frac{v}{al}$. Top figure adapted from Balazs et al. [99] under a Creative Commons license. Bottom figure is taken from Blanazs et al. [19] with text modified for clarity and consistency.

are only rules of thumb.

It is possible for multiple aggregate types to exist in thermodynamic equilibrium [90]. Additionally, it is common for surfactants such as phospholipids and block copolymers to be trapped in aggregates that are not at the minimum of Gibbs free energy. For example, phospholipids require the addition of energy (e.g. via sonication) to form vesicles, and some phospholipid aggregates take years to reach their equilibrium lamellar configuration [102]. Amphiphiles with larger hydrophobic blocks have increasingly slower equilibration kinetics, so that they exhibit kinetic trapping [101, 103, 104]. We will see that this has important implications for the block copolymer aggregates used in Chapter 4.

2.3 Gibbs and Langmuir monolayers

A property that will turn out to be relevant for droplet interface bilayers in Chapter 4 is whether a monolayer is soluble or insoluble. Here the monolayer solubility is distinguished from the surfactant solubility, although the two are related. Soluble monolayers are monolayers whose molecules are in exchange equilibrium with the molecules in the adjacent bulk. Insoluble monolayers are monolayers that do not exchange molecules with the bulk over some timescale of interest [90]. Soluble monolayers are also called Gibbs monolayers, while insoluble monolayers are also called Langmuir monolayers. Both types of monolayers may be adsorbed from surfactant in the adjacent bulk solution, but Langmuir monolayers are usually formed by dissolving surfactant in a volatile solvent and spreading it directly onto the interface.

In Langmuir monolayers, the monolayer behaves as a thermodynamic closed system. For a given total number of surfactant molecules at the interface, the surfactant will exist in a phase that depends on the interface area available to it [105]. This stands in direct

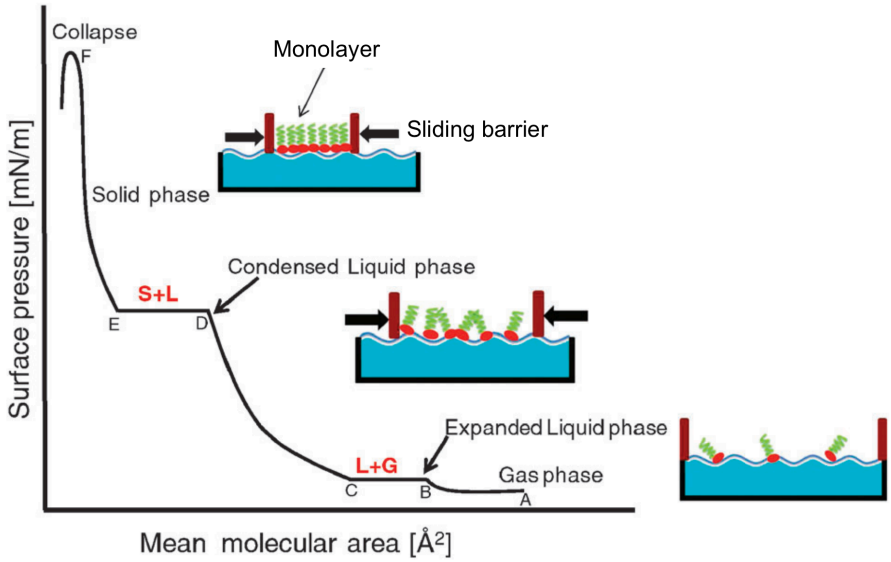

Figure 2.4: Phases apparent on an idealized Π-A isotherm for a Langmuir monolayer as a sliding barrier in compressed. This experimental setup is called a Langmuir trough. Source: Matharu et al. [107]

analogy to the dependence of the phase (ice, water, or vapor) of a fixed number of water molecules on the volume of an enclosure. Insoluble surfactant monolayers are typically characterized by a surface pressure-area (Π-A) phase diagram, as shown in Figure 2.4. The surface pressure Π is defined as the difference $\gamma_0 - \gamma$, where γ_0 is the interfacial tension in the absence of any surfactant, and γ is the interfacial tension; this means that the maximum surface pressure a monolayer may attain is γ_0, which corresponds to an interfacial tension of 0. The phases of surfactant molecule are gaseous, liquid expanded, liquid condensed, and solid[3] [106]. Once the Π-A phase diagram for a surfactant is determined, the phase of a monolayer can later be deduced simply by a measurement of its interfacial tension.

Gibbs monolayers also exist in one of the phases above. However, the phase is independent of the interface area because surfactant moves freely to and from the interface.

[3]Kaganer et al. suggest the use of the phrases "tilted condensed" and "untilted condensed" to describe the liquid condensed and solid phases because the two phases have the same amount of translation order, which is not always long range.

Instead, the phase of the monolayer is determined by the concentration of surfactant in the bulk. The relationship between concentration and monolayer tension below the CMC can be derived by considering the fundamental thermodynamic relation at an interface. For an interface:

$$dU = TdS + \gamma dA + \sum_j \mu_j dn_j \tag{2.5}$$

This is the same as the fundamental thermodynamic relation in bulk systems with the volume term PdV replaced with the area term γdA. Because all differentials in Equation (2.5) are extensive quantities they may be integrated to give:

$$U = TS + \gamma A + \sum_j \mu_j n_j$$

Differentiating this gives

$$dU = SdT + TdS + \gamma dA + Ad\gamma + \sum_j \mu_j dn_j + \sum_j n_j d\mu_j$$

and subtracting this from Equation (2.5) at constant temperature gives

$$d\gamma = -\sum_j \Gamma_j d\mu_j \tag{2.6}$$

where $\Gamma_j = \dfrac{n_j}{A}$ is the monolayer density. This equation is called the Gibbs equation or the Gibbs adsorption isotherm, and will be used again later in this section. It shows that if a species in the bulk accumulates at an interface, or equivalently if $d\mu_j$ is positive, then it will reduce the interfacial tension. By inserting a formula for μ as a function of the concentration of the species in the bulk, the relation between the bulk concentration and the interfacial tension can be deduced. Then, for low concentrations, the Gibbs

adsorption isotherm may be written as approximately [90, 105]:

$$\Gamma = -\frac{C}{RT} \cdot \frac{\partial \gamma}{\partial C} \tag{2.7}$$

which is often used to fit for the surface concentration Γ in a plot of interfacial tension against concentration C.

2.4 The dependence of droplet shape on interfacial tension

Wherever there exists a tension at the interface between fluids, the interfacial tension and geometry determine the pressure drop over the interface, which is called the Laplace pressure. The relationship between interfacial tension, pressure, and geometry is important to our work because it allows for the determination of surface tension from droplet shape in Chapter 4. Additionally, the Laplace pressure is important in the process of membrane thinning in a black lipid membrane in Chapter 3.

As a simple example, let us consider a immiscible sphere of fluid within the bulk of a liquid with a size small enough so that gravity does not affect its shape. For example, it could be a bubble of air in water or a droplet of water in oil. Let us consider a deviation in the size of the sphere by the exertion of work. The work dW has two contributions: PdV due to the volume expansion of the droplet against the bulk, and γdA due to the increase in interfacial area. In equilibrium, these variations must balance each other so that $PdV = \gamma dA$. For a sphere, $dV = 4\pi R^2 dR$ and $dA = 8\pi R dR$. Thus we have $P(4\pi R^2 dR) = \gamma(8\pi R dR)$ or:

$$P = 2\gamma/R \tag{2.8}$$

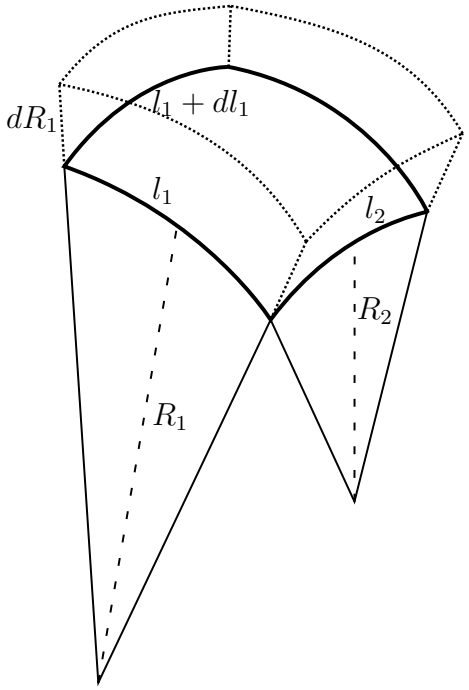

Figure 2.5: A small patch of interface used for deriving the Young-Laplace equation in the text.

This implies that as the size of the sphere decreases, its internal pressure increases relative to its surroundings.

This result can be generalized to arbitrary interfacial geometries following the derivation in Isenberg [108]. Consider the small section of the interface between two fluids shown in Figure 2.5. We must have $dW = PdV - \gamma dA = 0$ at equilibrium. An isotropic change in the radii by dz increases the area from $A = l_1 l_2$ to $dA = (l_1 + dl_1)(l_2 + dl_2)$, so that to first order $dA = l_1 dl_2 + l_2 dl_1$. The corresponding volume change is $dV = l_1 l_2 dz$. This gives $P l_1 l_2 dz = \gamma(l_1 dl_2 + l_2 dl_1)$ or

$$P = \gamma \left(\frac{1}{l_1} \frac{dl_1}{dz} + \frac{1}{l_2} \frac{dl_2}{dz} \right)$$

The derivatives $\dfrac{dl_j}{dz}$ can be determined by considering that the ratio of arc lengths must

equal the ratio of radii:

$$\frac{R_j}{R_j + dz} = \frac{l_j}{l_j + dl_i}$$

which gives simply that $\frac{dl_j}{dz} = \frac{l_j}{R_j}$. Thus we have:

$$P = \gamma \left(\frac{1}{R_1} + \frac{1}{R_2} \right) = 2\gamma\kappa \tag{2.9}$$

which is known as the Young-Laplace equation. The variable κ introduced here is called the mean curvature. The expression simplifies to Equation (2.8) when $R_1 = R_2 = R$. The Young-Laplace equation can be derived equivalently by considering the force due to membrane tension in each dimension independently [109]. Alternatively, it may be derived by minimizing the Helmholtz free energy [110].

The Young-Laplace equation has a simple form, but it must be written as a differential equation to model most physical systems. Its solution is typically difficult[4] unless it can be formulated naturally in polar or spherical coordinates. It is often used to describe axisymmetric droplets, such as a droplet in equilibrium on a flat and level surface, or a pendant droplet hanging from an axisymmetric needle or support. For a pendant drop, the coordinate system is typically set up as in Figure 2.6. Both inside the droplet and outside the droplet, the pressure must vary with height exclusively due to hydrostatic pressure $P = \rho_j g h$, where $g = 9.8$ m/s^2 and ρ_j is the density of the droplet or the surrounding fluid. Thus at each height $h = z$, buoyancy determines the pressure P over

[4] In Cartesian coordinates, for an arbitrary surface $z = S(x, y)$ the mean curvature has the form [108]:

$$\kappa = \frac{\left(1 + \left(\frac{\partial S}{\partial x}\right)^2\right) \frac{\partial^2 S}{\partial y^2} - 2\frac{\partial S}{\partial x}\frac{\partial S}{\partial y}\frac{\partial^2 S}{\partial x \partial y} + \left(1 + \left(\frac{\partial S}{\partial y}\right)^2\right) \frac{\partial^2 S}{\partial x^2}}{\left(1 + \left(\frac{\partial S}{\partial x}\right)^2 + \left(\frac{\partial S}{\partial y}\right)^2\right)^{3/2}}$$

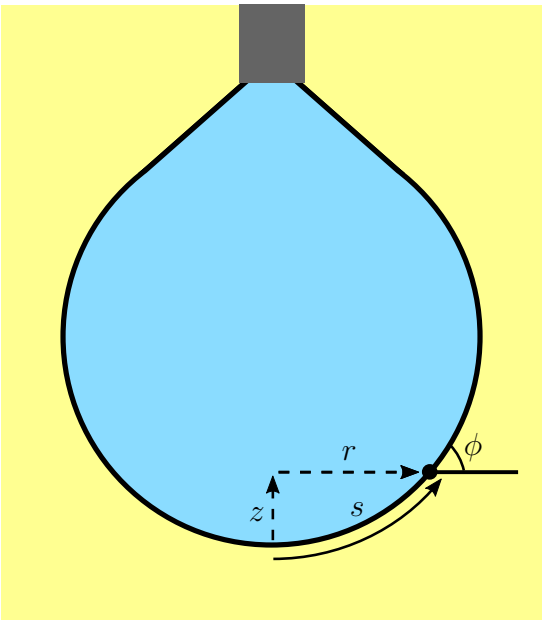

Figure 2.6: Coordinate system used for a pendant drop in Equation (2.10).

the interface:

$$P = P_0 - \Delta\rho g z.$$

Rewriting Equation (2.9) using the coordinates in Figure 2.6 yields the differential equation [109, 111]:

$$-\frac{\Delta\rho g}{\gamma}\sin\phi = \frac{d}{ds}\left(\frac{d\phi}{ds} + \frac{\sin\phi}{r}\right) \tag{2.10}$$

The boundary conditions are $\phi(0) = 0$ and $\phi'(0) = 1/r_0$, where r_0 is the radius of curvature at the bottom of the droplet. Only two unknowns are required to fully specify the solution to the equation. These may be chosen as γ and r_0, or they may be droplet dimensions such as the width and height of the droplet. This freedom is exploited in pendant drop fitting software so that a fit to the droplet shape provides the unknown value of γ [111, 112].

In aperture-suspended bilayers, the Young-Laplace equation is responsible for the initial stage of membrane thinning [34]. As shown in Figure 2.7, the curvature near the

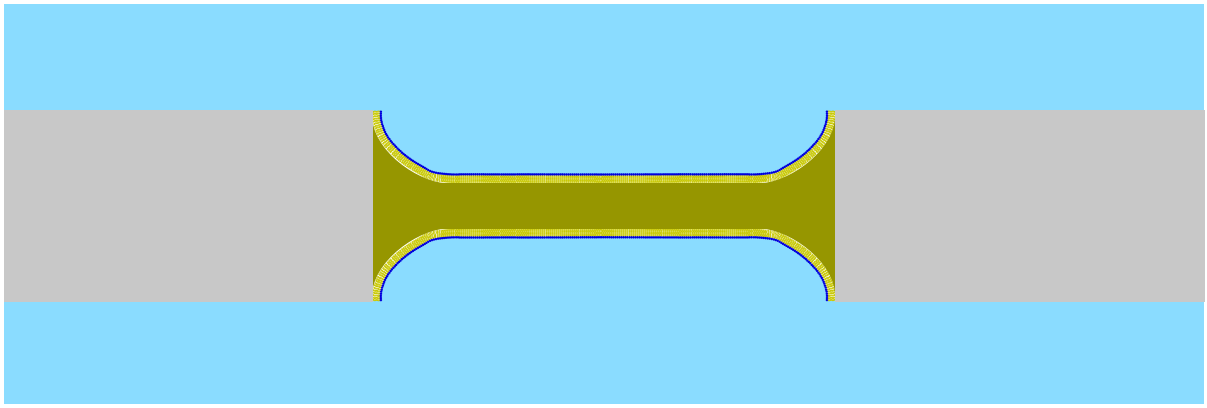

Figure 2.7: A painted lipid membrane in the process of thinning. If the contact angle is less than 90°, the interfaces must curve near the aperture edge. This causes a negative pressure near the aperture edges relative to the center, where the curvature is close to zero, so that the membrane thins.

center of an aperture is lower than the curvature near the aperture perimeter. This means that the Laplace pressure near the center is close to that of the surroundings, while the Laplace pressure near the aperture is lower. This causes the solution to flow from the center to the edges so that it thins out. This process continues until the top and bottom interface are within ~100 nm of each other, when thermal fluctuations and the Van der Waals attraction begin to play a role [42, 93].

2.5 The effect of applied voltage on membrane tension

In the presence of an applied voltage, a bilayer in electrolyte solution will accumulate charge, behaving as a capacitor. This has two important uses that relate to our research. First, it allows for the calculation of the thickness of the hydrophobic region of a membrane via its measured capacitance, as described in Chapter 1. Second, the capacitive stored energy acts to lower the free energy of the bilayer and similarly its tension. Because the monolayer tension is unaffected, this effect causes a change in contact

angle following Equation (2.2). Thus, the application of a voltage and corresponding measurement of the contact angle allows for the experimental determination of γ_{b} and γ_{m}. The relation and its derivation is outlined here, following the derivation of Requena and Haydon [11].

Changes in bilayer tension due to an applied voltage V can be described with the Gibbs adsorption isotherm, Equation (2.6), modified to include the effect of V. This is done by replacing the chemical potential μ with the electrochemical potential $\bar{\mu} = \mu + z_j FV$, where z_i is the valency of the charged species and F is the Faraday constant. At the bilayer, we have:

$$d\gamma_{\mathrm{b}} = -\sum_j \Gamma_j d\bar{\mu}_i$$

The sum is over all species in solution on both sides of the bilayer. The only species that accumulate at the interface are charged, so that they comprise the surface charge density $\sigma = e\sum_j \Gamma_j$, where e is the charge of an electron. Additionally, the electrochemical potential of these charged species is set by the electrode potential, so that $d\bar{\mu}_j = edV$.

Thus we have that $d\gamma_{\mathrm{b}} = -\sigma dV$. For a specific capacitance C, $\sigma = CV$, so that $d\gamma_{\mathrm{b}} = -CVdV$, which may be integrated:

$$\Delta\gamma_{\mathrm{b}} = -\int_{\gamma_0}^{\gamma_V} CVdV = \frac{1}{2}C\Delta V^2.$$

This describes the difference in bilayer tension γ for a difference in applied voltage V. Combining this with Equation (2.2) for a symmetric bilayer yields:

$$\cos\theta_0 - \cos\theta_V = -\frac{C}{4\gamma_{\mathrm{m}}}(V^2 - V_0^2) \tag{2.11}$$

which relates the observed contact angle θ_V at an applied voltage to γ_{m} and C given a contact angle of θ_0 for $V = 0$. This is known as the Young-Lippmann equation.

2.6 Redox electrodes

Nanopore sequencing is based on a resistive pulse technique: different nucleotides in the pore cause changes in the pore resistance, allowing DNA to be sequenced. The current through the pore is purely ionic[5], while the current measured in the amplifier (i.e. the data to be analyzed) is electronic. It follows that in order for charge to form a complete circuit, electronic current must be converted into ionic current. This conversion occurs at the electrode-solution interface, and the study of this electron transfer process lies in the field of electrochemistry [113].

A complete electrochemical circuit consists of a voltage source, wires, a pair of electrodes, and the solution. In order to complete the circuit to both terminals, there must be two electrode/solution interfaces. The electron transfer behavior at an interface depends on the metal, the species that are dissolved in the aqueous phase, and the applied voltage. In order to convert electronic charge into ionic charge, there must be a species dissolved in the solution that is capable of being oxidized (having an electron removed) or reduced (having an electron added) by the electrode. The process of oxidation and reduction typically have a forward and reverse reaction rate, so that the process can be described by $\mathrm{Ox} \longleftrightarrow \mathrm{Red} + \mathrm{e}^-$. This reaction is characterized by a potential $V^\ominus$ at which the forward and reverse rates are equal for a standard concentration of both species, so that equilibrium is reached. This is called the redox potential for the species.

The Nernst equation describes the dependence of the equilibrium on concentration. Due to nonidealities, the equation is written in terms of activities a_{Red} and a_{Ox}, which are equal to concentration in the limit of low concentration:

$$V = V^\ominus - \frac{kT}{q} \ln \frac{a_{\mathrm{Red}}}{a_{\mathrm{Ox}}} \tag{2.12}$$

[5]Electrons in water do not form a conduction band.

The logarithmic dependence arises from Boltzmann's equation. If the electrode potential is lowered to below the redox potential, the reduced species is favored, and current will flow until equilibrium is reached; on the other hand, if the potential is raised above the redox potential, the oxidized species is favored. The Nernst equation applies whether or not an external voltage is applied. In the absence of an applied voltage, the concentration of the reduced and oxidized species determine the potential at the interface via the Nernst equation. Alternatively, for an applied constant voltage V, the Nernst equation determines the ultimate concentrations once equilibrium is reached.

Ag/AgCl electrodes are frequently used in nanopore sensing for several reasons: (1) the electron transfer reaction $Ag + Cl^- \longleftrightarrow AgCl + e^-$ happens readily even at very low applied voltages, so that the nanopore and solution resistances always dominate the current; (2) the value of the redox potential avoids undesirable reactions such as the hydrolysis of water; (3) the requisite inclusion of Cl^- for the electrode to function properly is rarely detrimental, considering NaCl and KCl are common electrolytes; (4) their construction is relatively straightforward. The potential of each Ag/AgCl electrode is set by the Cl^- concentration as given by the Nernst equation. For these reasons, Ag/AgCl electrodes are used for measurements in both Chapters 3 and 4.

The use of Ag/AgCl electrodes has two limitations that are common to all redox electrodes. First, the concentration of Cl^- will change as current is flowed, effecting the relative potential of the electrodes. Second, if the finite supply of Ag, AgCl or Cl^- is exhausted, the electrode will cease to function normally. These can translate into practical limitations in nanopore sequencing devices such as a minimum reservoir size for the measurement solution or a minimum electrode size; alternatively the devices must be designed differently to replenish Cl^- or they must be operated differently to periodically replenish Ag or AgCl in the electrodes.

Chapter 3

Automatically-painted triblock copolymer membranes for protein nanopore-based DNA sequencing

As explained in the introduction, the use of an automated approach is critical to the commercialization of nanopore DNA sequencing. The rate of nanopore DNA sequencing has to date been limited to below 500 bases per second [114] due to the tradeoff between noise and bandwidth [81]. Even at a rate of 1,000 base per second, it would take 35 days to sequence a full human genome (~3 gigabases) using a single nanopore. An arrayed device reduces this time by taking measurements in parallel: a 1-cm square device could fit 2,500 nanopores each in a 200-µm square area, ideally lowering the translocation time for an entire genome from 35 days to 20 minutes. Therefore, in this section, the use of an automated, arrayed system is explored.

The automated system uses a microfluidic painting approach similar to that used by Suzuki et al. [54]. In this chapter we show that when switching from a previous hand-painted system [20] to this system, both using the same painting solution with

the same block copolymer, the behavior of the nanopore MspA is often degraded significantly. We establish a metric for quantifying the quality of MspA behavior and the causes for variations in the behavior are investigated. Finally, we demonstrate the successful translocation of hairpin DNA through an MspA nanopore in an automatically-painted block copolymer membrane, producing results that are similar to the pioneering results of Butler et al. [83] in phospholipid bilayers.

3.1 Experimental details

The device used here was largely designed by collaborators at Illumina. It features a microfluidic array of eight wells and apertures as well as two ground wells fabricated using a photopatternable epoxy similar to SU-8 (ADEX from DJ Devcorp) on a glass substrate. Each aperture well is comprised of a Ag/AgCl electrode (silver on gold, electrochemically chlorided) at the base and apertures between 35 µm and 100 µm in diameter aperture at the top, sitting on a wider reservoir. The ground wells and electrodes are much larger so that they can accommodate the use of all eight apertures. The thickness of the apertures is 10 µm. A fluoropolymer (Fluoropel 2000V) was spin coated and baked on the surface in order to make it more hydrophobic. The microfluidic channel was formed by placing a rectangular gasket over the electrode array and sandwiching them between two holder pieces. The top holder piece was machined from Teflon and featured reservoirs and fittings for microfluidic tubing to serve as an inport and outport while the bottom piece served as a support. A window was made through the bottom piece so that the channel could be viewed during the flow of polymer solution if desired.

The device design received from Illumina was optimized for use with the equipment available at UCSB by varying microfabrication parameters such as bake times, photolithography exposure times, and cleaning protocols. The most serious fabrication issue

encountered at UCSB was delamination of the SU-8 from the glass, which was resolved by adding a 400W oxygen plasma cleaning step before lamination of SU-8, as well back-side flood exposure through the glass substrate during photolithography of the SU-8. This helped the SU-8 achieve a more uniform exposure throughout its thickness, which likely resulted in reduced stress.

Electrical measurements were performed in voltage clamp mode (constant voltage) by connecting the headstage of an Axopatch 200B to the ground wells and one of the aperture wells. Data was filtered using the Axopatch's built-in 8-pole, 10-kHz filter and was sampled using a Digidata 1550 at 100 kHz. Capacitance measurements were performed by applying a 50-Hz sinusoid and using the impedance to deduce R and C. To address other aperture wells, the live electrode was switched manually from one to another. In some cases this would cause a membrane to break, but in most cases it would not; the presence of MspA in these cases proved that a polymer membrane could withstand manual electrode switching. Membrane quality was typically deduced from capacitance (though these were unreliable, as will be explained), leak current, and voltage-induced breakage. MspA insertions served as a final indication of membrane formation.

Once the channel was assembled, buffer solution was loaded into the channel and the assembly was placed under vacuum to load the buffer into the wells. In all experiments, a buffer solution of 1M KCl, 10 mM HEPES, pH 8 (titrated using KOH) in Millipore water was used. Typically, between 0.2 µL and 5 µL of a solution of 1 wt% polymer in 3:1 chloroform:decane (v:v) was loaded at the in-port and pushed through using a syringe pump. Electrical measurements of this first set of membranes was performed, and after these membranes were broken, an air bubble was flowed through at a rate between 1 µL/min and 5 µL/min to form a new set of membranes. The process of flowing air bubbles and making measurements was repeated until membranes could no

longer be formed.

In all cases, $PMOXA_{13}$-*b*-$PDMS_{47}$-*b*-$PMOXA_{13}$ was used as the block copolymer, synthesized as reported in Isaacman et al. [115]. The block lengths are deduced from their corresponding molecular weights, which were determined to be 1,100 g/mol for each PMOXA block and 3,500 g/mol for the PDMS block. Polymer solutions made previously by our group for manually painted apertures [20] were typically prepared by volume in a ~200 µL quantity and stored in 5 mL vials. This had the potential to cause variation between experiments due to evaporation of chloroform both during preparation and over the course of experiments. To avoid such variations in these experiments, the painting solutions used here were always made in large batches (>1 mL), were always measured by weight, and were stored in 2 mL, low-leakage vials (SureStop by Thermo Fisher Scientific) with Teflon caps. Typically, 16 mg of dry $PMOXA_{13}$-*b*-$PDMS_{47}$-*b*-$PMOXA_{13}$ was dissolved in 1.20 g of chloroform. After dissolution, 0.20 g of decane was added, yielding a solution that is 1.1 wt.% polymer. By volume, the solution is 75% chloroform and 25% chloroform, the same as the solution made previously [20].

The MspA referred to throughout this chapter is the mutant M2MspA reported in Butler et al. [83], provided generously by Jens Gundlach. Prior to use, MspA was stored in a buffer solution at 0.1 or 1 µg/mL concentration with 0.1 wt.% octyl-POE (n-Octyl-oligo-oxyethylene, Santa Cruz Biotechnology, Inc.; a nonionic surfactant) in a refrigerator to prevent its aggregation. At the time of an experiment, MspA was added to the 1M KCl, 10 mM HEPES, pH 8 buffer described above to a working concentration of 2.5 ng/mL. For all results reported here, this MspA-buffer solution was introduced prior to membrane formation. Hairpin DNA was diluted to a concentration of 1 µM in the same buffer and was introduced only after membrane formation and MspA insertion. The hairpin DNA used was provided by Illumina with the following sequence:

/5Phos/TTT TTT TTT TTT TTT TTT TTT TTT TTT TTT TTT TTT TTT TTT TTA AAC GAC CGA GAC AAC GCT CTC TCG TTG TCT CGG TCG

Membrane formation

The flow of polymer solution typically coated the channel interior and caused all apertures to be insulating. The subsequent flow of air bubbles then lead to a diminishing number of insulating channels until eventually all channels remained conducting. Typically, most or all insulating apertures could be made conductive with a 1.3-V zap. When MspA was present in solution, most or all membranes after the first or second air bubble included MspA insertions. Membranes that could not be broken with a 1.3-V zap never allowed for the insertion of MspA, which indicates an excess of polymer solution that prevented thinning to bilayer thickness.

MspA insertion statistics

In order to analyze DNA translocation data, it is important that there be a single nanopore in an aperture; otherwise the multiple pores will all contribute to the current. Because nanopore insertion events are discrete and independent, insertion is a Poisson process, and it is straightforward to show that the maximum theoretically attainable average number of single insertions is $1/e = 36.8\%$. This means that an average of approximately 3 out of the 8 apertures will have single MspA insertions if an optimal concentration of MspA is present in the buffer solution, regardless of the insertion mechanism. At a concentration of 2.5 ng/mL MspA loaded in the buffer prior to membrane formation, it was common that two to four membranes had single insertions. This shows that the concentration used was near optimal.

Specific capacitance measurements

The system did not permit a simple analysis of membrane specific capacitance. Typically, when a planar membrane experiment is performed, it can be assumed that the membrane area is bounded by the aperture area. If the membrane cannot be imaged to determine the membrane area as in our case, the aperture area can still be used to provide a bound on the specific capacitance. However, in our system, the specific capacitance would occasionally rise to unrealistically high values (~2 $\mu F/cm^2$) using this approach. This implies that the membrane was not actually bounded by the aperture area. Additionally, the capacitance would sometimes decrease to below the baseline value for a plugged aperture. This occurred either due to movement of the leads during polymer and air flows or due to impedance changes from the accumulation of polymer solution on the electrodes. While the measurement of capacitance gave an indication of membrane quality, no one measurement could be relied upon as accurate. For these reasons, we do not report capacitance measurements in this microfluidic system.

3.2 Investigation into the variation of MspA behavior

In order to perform resistive pulse based DNA sequencing, it is desirable to have a nanopore with a steady conductance in the absence of DNA. There are two types of conductance variations that arise in nanopores: voltage gating and noise. Gating is the partial or complete shutting of a pore, and is a common response of many pore-forming proteins to applied voltages [116]. Voltage gating occurs stochastically and can occur over both short and long timescales, causing both small and large jumps in current. A nanopore that is gated might not translocate DNA or otherwise could make the nucleotide sequence difficult to discern [15]. Additionally, gated pores can make it difficult to determine whether there is one or more nanopore present. Different mechanisms for gating have been proposed [116, 117], and membrane thickness and tension are two such mechanisms known to affect gating via membrane-protein interactions [49, 118].

Noise in the nanopore current is also undesirable because it decreases the signal-to-noise ratio, so that current levels associated with different DNA nucleotides are harder to discern [81]. Nanopore noise is common and often has a $f^{-\alpha}$ characteristic so that it increases with lower frequency f with α~1 [20, 119, 120]. Other noise characteristics also occur, which include a flat characteristic that is still larger than thermal noise or shot noise [20, 121]. As in voltage gating, noise in nanopores is also exacerbated by membrane-protein interactions [20]. Additionally, for many proteins, both the probability of gating and the amplitude of noise increases with voltage magnitude [81, 116, 121, 122].

Wild-type MspA shows significant voltage gating behavior even at 30 mV [117]. By modifying some of the amino acids at the constriction of MspA, Butler et al. succeeded in removing most noise and gating behavior of MspA even at 180 mV [83]. The application of 180 mV is desirable not only to increase the capture rate of DNA, but also to provide

the force needed to use polymerase as a DNA ratchet with MspA experiments [85]. In ordinary aperture-suspended membranes using DPhPC, MspA exhibits a flat frequency spectrum [20] and few gating events (~0.5 short dips in current per second) [83] at 180 mV in the absence of DNA.

Our group previously sought to replace DPhPC with a block copolymer [20] for the benefits discussed in Chapter 1, including improved stability and robustness. Triblocks were chosen over diblocks for their simpler synthesis, and PMOXA-PDMS-PMOXA polymers were chosen in particular because the PDMS group has a high flexibility that allows it to accommodate proteins of different sizes [123]. Despite the high PDMS flexibility, in initial experiments, MspA in PMOXA-PDMS-PMOXA polymer membranes exhibited high noise and significant voltage gating even at 60 mV. After optimizing polymer block length, MspA exhibited DNA-free characteristics similar to lipids [20]. However, when we switched from a manually-painted aperture to the microfluidic painting approach described here, high noise and gating were observed again using the optimized polymer ($PMOXA_{13}$-*b*-$PDMS_{47}$-*b*-$PMOXA_{13}$). Thus we set to determine the cause of this gating and noise so that it could be reduced.

To this end, an investigation into the variation in MspA behavior was performed on three devices. As determined by optical microscopy shown in Figure 3.1, device 1 had 50-µm apertures, device 2 had 43-µm apertures, and device 3 had 35-µm diameter apertures. Because the aperture arrays were all made using the same photomask with circles of the same diameter, the differing UV exposure conditions resulted in differing sidewall profiles also. A highly inclined sidewall profile is visible in device 3 due to this effect, while the profiles of device 1 and 2 were less extreme. When MspA was introduced to membranes formed in this system, most MspA insertions behaved poorly, displaying both high baseline noise and gating, while some insertions behaved well.

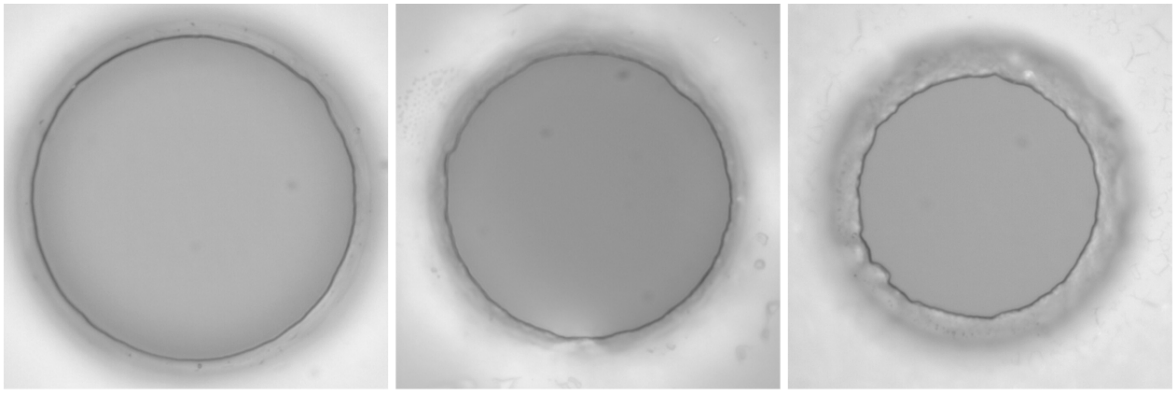

Figure 3.1: Representative apertures 50 µm, 43 µm, and 35 µm in diameter, from left to right. The shading on the 35-µm diameter aperture suggests its shape is a conical frustum. These images are focused at the tops of the apertures, but the microscope objective could also resolve the bottoms of the apertures by looking through the SU-8 as a results of the wider diameter at the bottom. This indicated that the 43-µm and 50-µm apertures are also shaped like the 35-µm apertures, but with sidewall angles much closer to vertical.

3.2.1 A metric for MspA behavior

In order to determine the experimental parameters causing MspA variation, it was useful to establish a numerical metric for MspA behavior. The frequency spectrum analysis in Morton et al. [20] could not be used alone because at 180 mV gated MspA sometimes has a low and flat noise spectrum that is typically indicative of better behavior, as evidenced in Figure 3.2. Thus the conductance at 60 mV was used as a primary filter against pores with significant gating: MspA with an open-pore conductance lower than 1.55 nS at 60 mV typically exhibited gating or otherwise behaved erratically, which is in line with the previously reported conductance of 1.84 ± 0.24 nS for well-behaved MspA in this polymer. Insertions with conductances above 1.55 nS allowed for a straightforward frequency spectrum analysis at 180 mV. We used the spot noise at 10 Hz as a metric for MspA behavior because it correlates with spectrum slope but also takes magnitude into account, as demonstrated in Figures 3.2 and 3.3. Using this criteria, the spot noise at 10 Hz varied over 3 orders of magnitude.

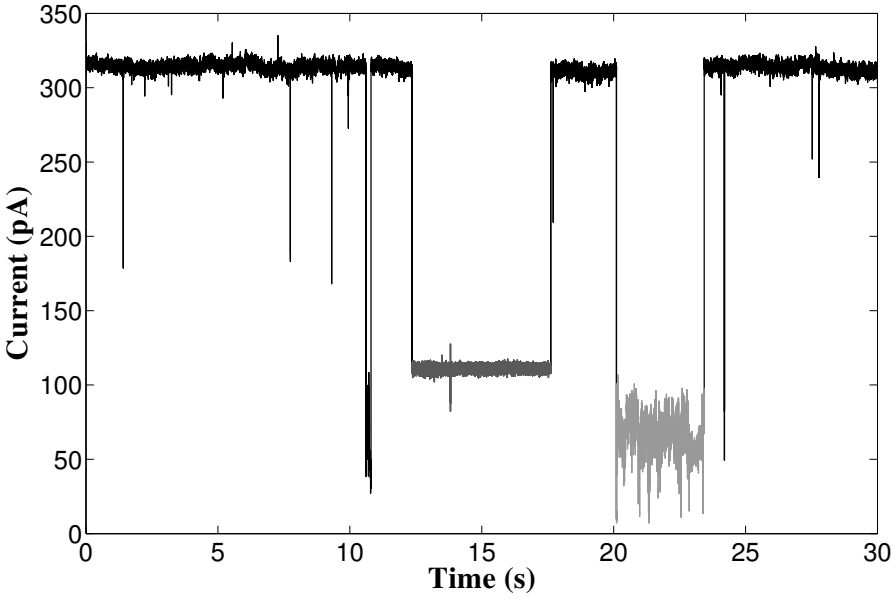

(a)

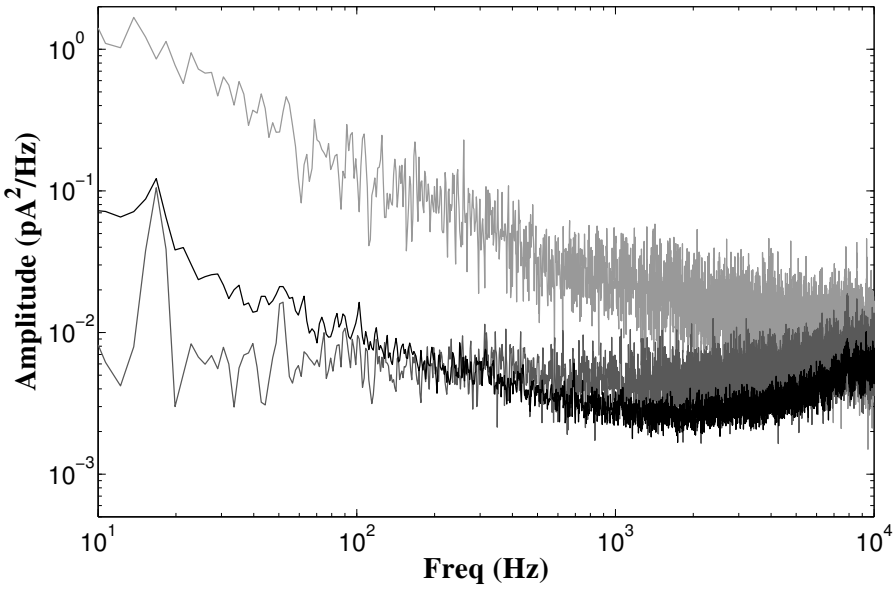

(b)

Figure 3.2: Current trace (a) and frequency spectrum (b) for a single poorly-behaved insertion at 180 mV applied. The frequency spectra correspond to different parts of the trace, which demonstrates that gated pores can be noisier or quieter than the baseline. All dips, spikes, and gating events that deviated by more than 3.5 standard deviations from each current level were excised from the current trace to produce the frequency spectra as described in text. Note that the spot noise of the baseline at 10 Hz is ~0.07 pA^2/Hz.

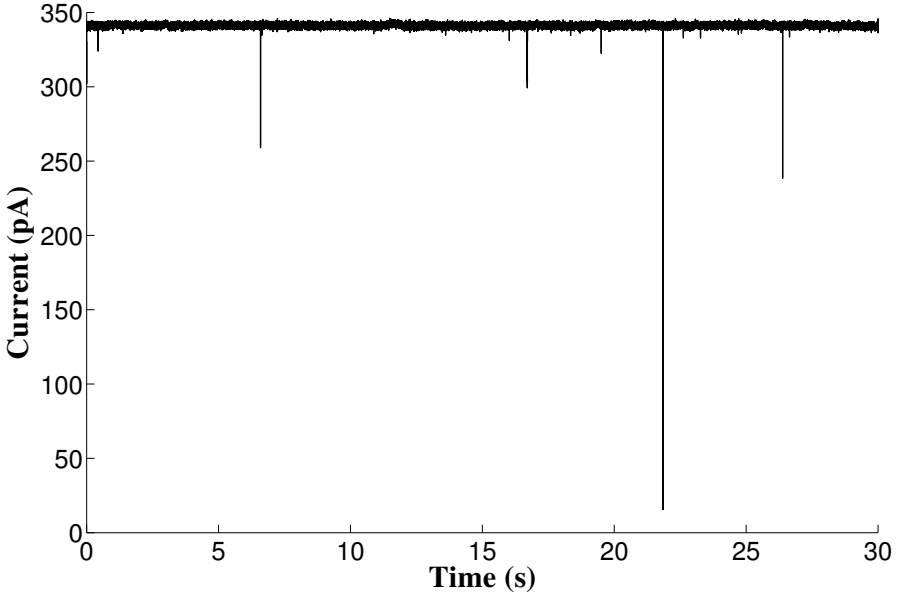

(a)

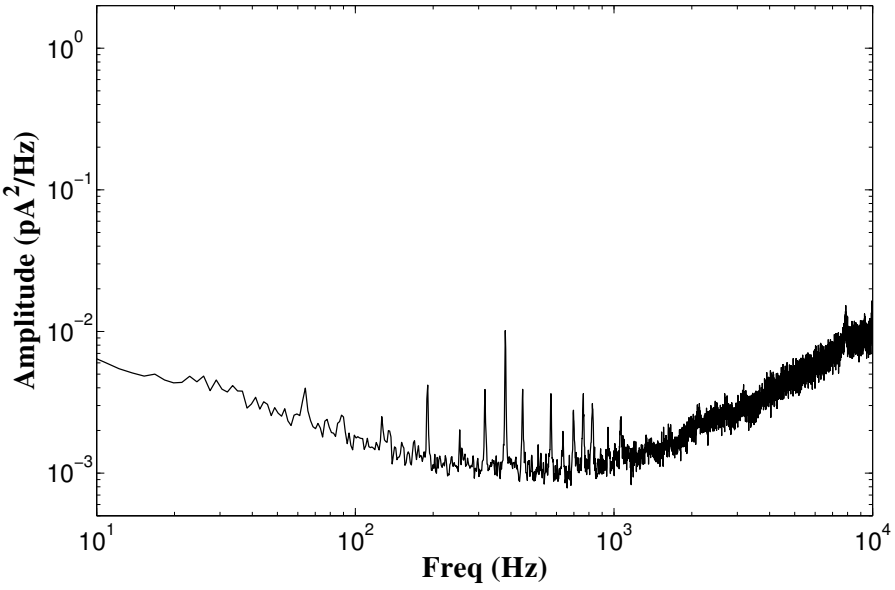

(b)

Figure 3.3: Current trace (a) and frequency spectrum (b) for an MspA insertion exhibiting low baseline noise with 180 mV applied. The large, single-step dip in current (and other similar large dips not shown here) prove the presence of an insertion of at least 320 pA in current. The spot noise at 10 Hz is ~0.006 pA^2/Hz, over 10 times lower than the baseline in Figure 3.2.

Prior to computing the frequency spectra, all dips and spikes that deviated by more than 3.5 standard deviations from the baseline were excised from the current trace $I(t)$. This was done to exclude the stochastic contribution of dips and spikes, which significantly impacts the frequency spectrum. A Gaussian function was fit to the main peak in the histogram of $I(t)$ and used to determine the mean $\langle I \rangle$ and standard deviation σ of the baseline. Then all datapoints between $\langle I \rangle - 4\sigma$ and $\langle I \rangle + 4\sigma$ were used to compute a 10,000-point-smoothed baseline over time, $I_{\mathrm{B}}(t)$. $I(t)$ was then excised so that only datapoints between $I_{\mathrm{B}}(t) - 3.5\sigma$ and $I_{\mathrm{B}}(t) + 3.5\sigma$ were used to compute the frequency spectrum via a fast Fourier Transform (FFT). Prior to computing the FFT, the data was windowed into overlapping intervals 0.7 seconds in duration beginning every 0.2 seconds. Then the FFT of all windows was averaged to yield a smoothed FFT[1].

3.2.2 Origin of noise and gating variation

Multiple insertions in the same membrane typically have similar noise characteristics, as evidenced by Figure 3.4. This suggests that the behavior of MspA insertions is primarily a result of the properties of an individual membrane and not another feature such as the polydispersity of the polymer [20, 124]. There are two main experimental parameters that could affect the membranes: aperture geometry and painting protocol. The difference in aperture geometry was already shown in Figure 3.1: both shape and diameter varied between devices. The major difference in painting protocol was that after the flow of painting solution, a different number of air bubbles was used to form each membrane. In order to discern these effects, the aperture geometry and the spot noise for single MspA insertions were plotted against the number of air bubbles flowed since the most recent painting solution flow in Figure 3.5. There is a strong trend that membranes formed after more air bubbles support better quality insertions. Additionally, at each air

[1] A Hann window was used. All computations were made using a Matlab script.

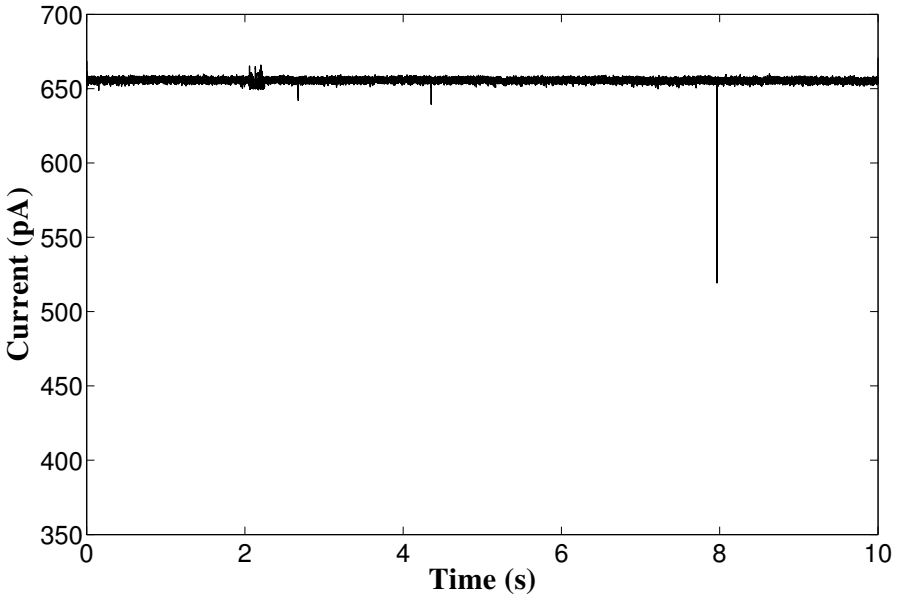

(a)

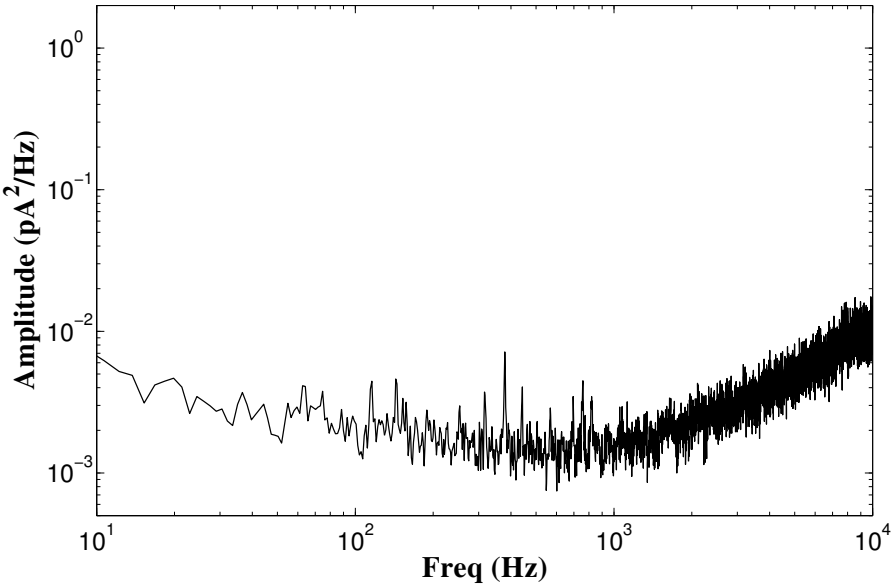

(b)

Figure 3.4: Current trace (a) and frequency spectrum (b) for two good insertions in the same membrane. While such low baseline noise was extremely rare, these two occurred in the same membrane, which demonstrates that insertion quality is a reflection of individual membrane properties. This is the same membrane as in Figure 3.3 and a discrete jump in the baseline current from 340 pA to 660 pA was recorded between these two measurements. Note: the scale is the same as in Figure 3.2 but trace is offset by 350 pA.

bubble number, larger apertures are more likely to support better insertions.

After the polymer solution coats the channel interior, the flow of air bubbles has three potential effects: (1) it can sweep painting solution out of the channel[2], (2) it can induce drainage of the painting solution from the aperture [125], and (3) it can decrease the chloroform and decane[3] concentration by evaporation. This suggests two possible mechanisms for affecting MspA behavior: differing volumes in the solvent annulus for different apertures and changing composition of the polymer solution.

Annulus volume directly affects membrane area, and thereby affects the possibility for the existence of a membrane. If the annulus volume is too low, the membrane will lack the volume necessary to span the aperture; if annulus volume is too large, a bilayer may take too long to form. This air bubble approach is very similar to the automated approach reported by Sandison et al. [125]. For their devices, they reported that exposure to air between 15 and 35 seconds lead to rapid thinning of their membranes to achieve large bilayer areas. However, in their case, there were major differences: (1) their painting solution involved lipid in decane only, (2) their open geometry included a surrounding space to which the painting solution could wick away, and (3) they began with a controlled volume of painting solution and actively monitored its volume as it was wicked away by exposure to air.

Due to the confined geometry, the painting solution probably cannot wick from the aperture to the channel if the coated thickness is too large. It is possible that the membranes can wick into the wells beneath the aperture, but the surface chemistry of the bottom surface of the apertures is not well controlled: the Fluoropel may have reduced access to the aperture bottoms during spin coating, so that the aperture bottoms may be uncoated, fully coated, or partially coated. This was supported by the observation that

[2]This behavior is observed when dragging air bubbles over the polymer solution on a transparent Teflon partition.

[3]The decane concentration is affected less because it is far less volatile.

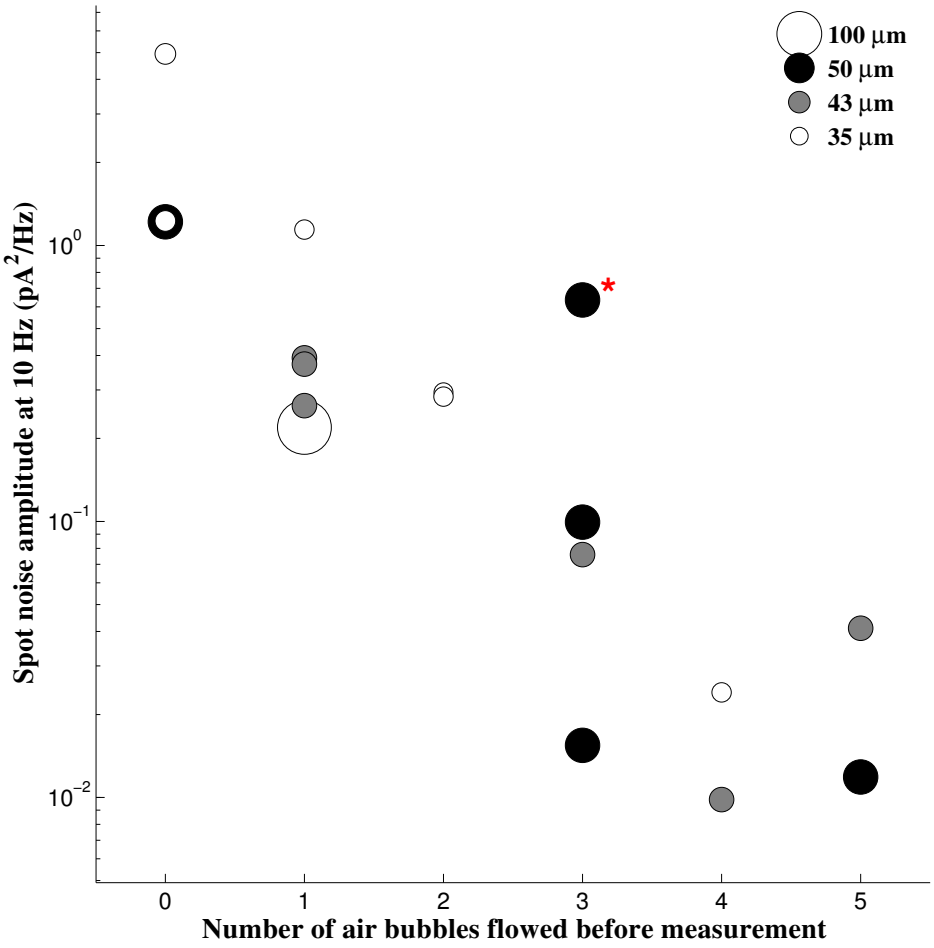

Figure 3.5: Scatter plot showing how spot noise at 10 Hz in MspA single insertions at 180 mV depends on the number of air bubbles flowed through the channel since polymer solution was last flowed. Each circle represents a single MspA insertion in a different membrane, with aperture diameter represented by circle area and shading. The trend is clear that MspA has better noise characteristics in membranes formed using more air bubbles: for a linear regression of the semilog data, $p = 6 \times 10^{-6}$ and $r^2 = 0.73$ when including the outlier point marked with an asterisk. In the case of the outlier, the spot noise dropped by a factor of 100 about 5 minutes later. Reductions in noise were very rarely observed, so the point may be considered to be an outlier. Excluding this data point, or repositioning it to its later value, makes the trend even more prominent. However, the point is included because additional measurements beyond the first 5 minutes at 180 mV were not always available. Additionally, at every bubble number, the geometric mean of the spot noise increased with aperture diameter with the exception of 3 bubbles. This trend becomes absolute with the outlier removed or repositioned. In all cases, the first 5 seconds of data taken at 180 mV was used to calculate the spot noise. Note the overlapping data points for 0, 1, and 2 air bubbles.

the aperture bottoms were more likely than the tops to accumulate material that seemed to have been precipitated by solvent changes. All of these effects amount to potential variations in the amount of painting solution in the aperture, which determines the area or the existence of a bilayer region.

Solution volume and aperture size and shape can affect membrane properties because the curvature at the annulus causes a Laplace pressure via Equation (2.9). This increased pressure within the annulus counteracts the pressure associated with the free energy of bilayer formation (called the disjoining pressure) and could thereby affect membrane thickness and tension [93]. The effect of the Laplace pressure on membrane tension in an aperture-suspended membrane involving lipids has been reported by Beltramo et al. [9]. Knowing the effect of the Laplace pressure requires knowing the geometry of the annulus, but, while the geometry has been solved for cylindrical aperture by White [126], to our knowledge such an analysis has not been performed for our geometry. It is reasonable that smaller apertures would lead to higher membrane curvatures, leading to higher Laplace pressures and higher membrane tension. This higher tension could be responsible for the trend that larger apertures tend to have better MspA behavior. Reducing the volume of solution in the annulus and its surroundings by flowing air bubbles could affect MspA behavior in a similar way.

The other potential mechanism by which the number of air bubbles has an effect is the solution composition. Solution composition is known to affect the bilayer on a molecular level, whereby residual solvent in the membrane affects both its thickness[4] and tension. Thus it is possible that differing aperture areas affect bilayer properties by affecting solution composition via the evaporation of chloroform. To investigate this effect, a preliminary experiment was performed using a 200-µm-diameter Teflon aperture on a microscope stage with the same polymer solution used for microfluidic painting. The

[4]The effect of oil on thickness will be demonstrated in Chapter 4.

polymer solution was dispensed over the aperture manually and air bubbles were allowed to sit on the polymer solution for 1 to 5 minutes prior between each subsequently formed membrane. All membranes spanned the 200-µm-diameter aperture, so that their area was known during capacitance measurements. The result was that the specific capacitance rose monotonically from less than 0.1 µF/cm^2 for the first membrane to over 0.2 µF/cm^2 for the last membrane.

If the dielectric constant ϵ of the hydrophobic region is known, it can be used to determine its thickness h using the formula for a parallel plate capacitor: $C_{\text{specific}} = \epsilon/h$. The presence of three potential components in the hydrophobic region (PDMS, decane, and chloroform) each with different dielectric constants ($2.8\epsilon_0$, $2.0\epsilon_0$, and $4.8\epsilon_0$, respectively) makes a determination of the hydrophobic thickness difficult, because the composition is unknown and varies with hydrophobic thickness. However, assuming as a rough estimate that $\epsilon = 3\epsilon_0$ implies a hydrophobic thickness that varies from ~20 nm to ~10 nm with exposure to air. Considering that MspA has a hydrophobic thickness of 3.7 nm [127], it is understandable why air bubbles improve behavior: a membrane with a hydrophobic thickness of 10 nm is much less likely to affect MspA than a hydrophobic thickness of 20 nm. At the same time, the high flexibility of PDMS could reduce the impact of this difference.

While the precise thickness values are unknown, the varying specific capacitance shows that the solution composition is affected by the evaporation of polymer solution in contact with air bubbles. Considering that membrane tension also varies with membrane composition, both the thickness and tension are potential causes of the variation in MspA behavior. This all suggests that the use of a volatile solvent that is sometimes used to form block copolymer membranes [20, 128, 129] necessitates special attention. One remedy would be to avoid the use of a volatile solvent. Other remedies would be to plan the effects of evaporation into the design or to avoid the use of air bubbles altogether.

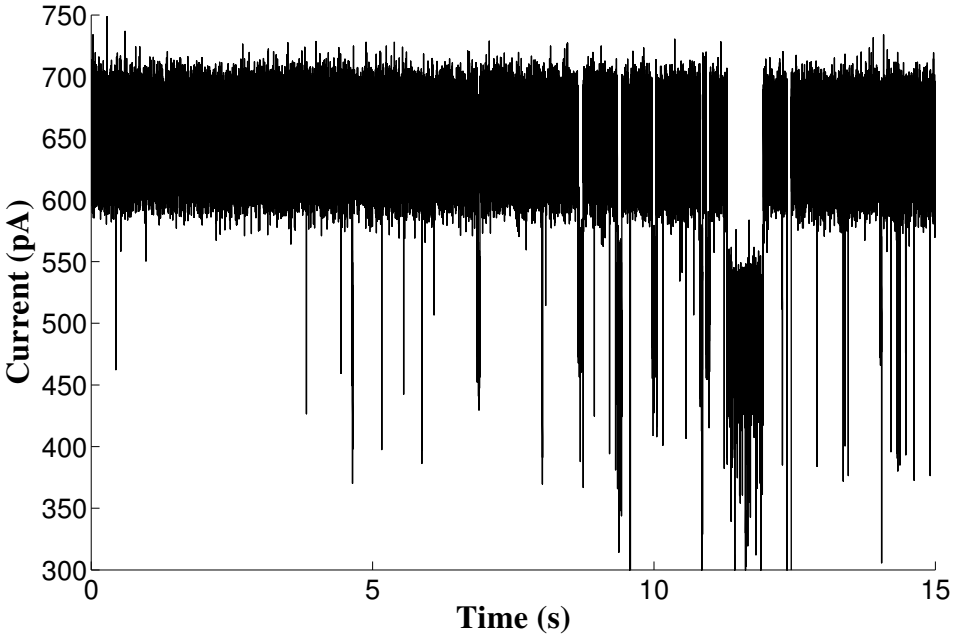

Figure 3.6: The trace shows two MspA insertions in a polymer membrane just as the front of hairpin DNA solution reaches the membrane with 180 mV applied. 6 blockades are visible in the first 5 s and approximately 20 blockades are visible in the last 5 s, a 4-fold increase. Overall (not shown) the combined blockade rate increased 20-fold, from 0.5/s prior to the introduction of hairpin DNA, to over 10/s.

3.3 Translocating hairpin DNA through MspA in block copolymer membranes

In order to investigate the ability of MspA in a $PMOXA_{13}$-*b*-$PDMS_{47}$-*b*-$PMOXA_{13}$ membrane to translocate DNA, hairpin DNA constructs were added in the measurement buffer, in a replication of Butler et al.'s experiment using lipid bilayers [83]. Figure 3.6 shows a current trace just as MspA in microfluidically-painted polymer membranes was exposed to 1 µM hairpin DNA. Overall, the hairpin DNA caused a 20-fold increase in the blockade rate.

Zooms of the current traces of individual hairpin DNA blockades in a single MspA insertion are shown in Figure 3.7 and closely resemble those reported by Butler et al. After hairpin DNA measurements were performed on a single MspA insertion, the statistics

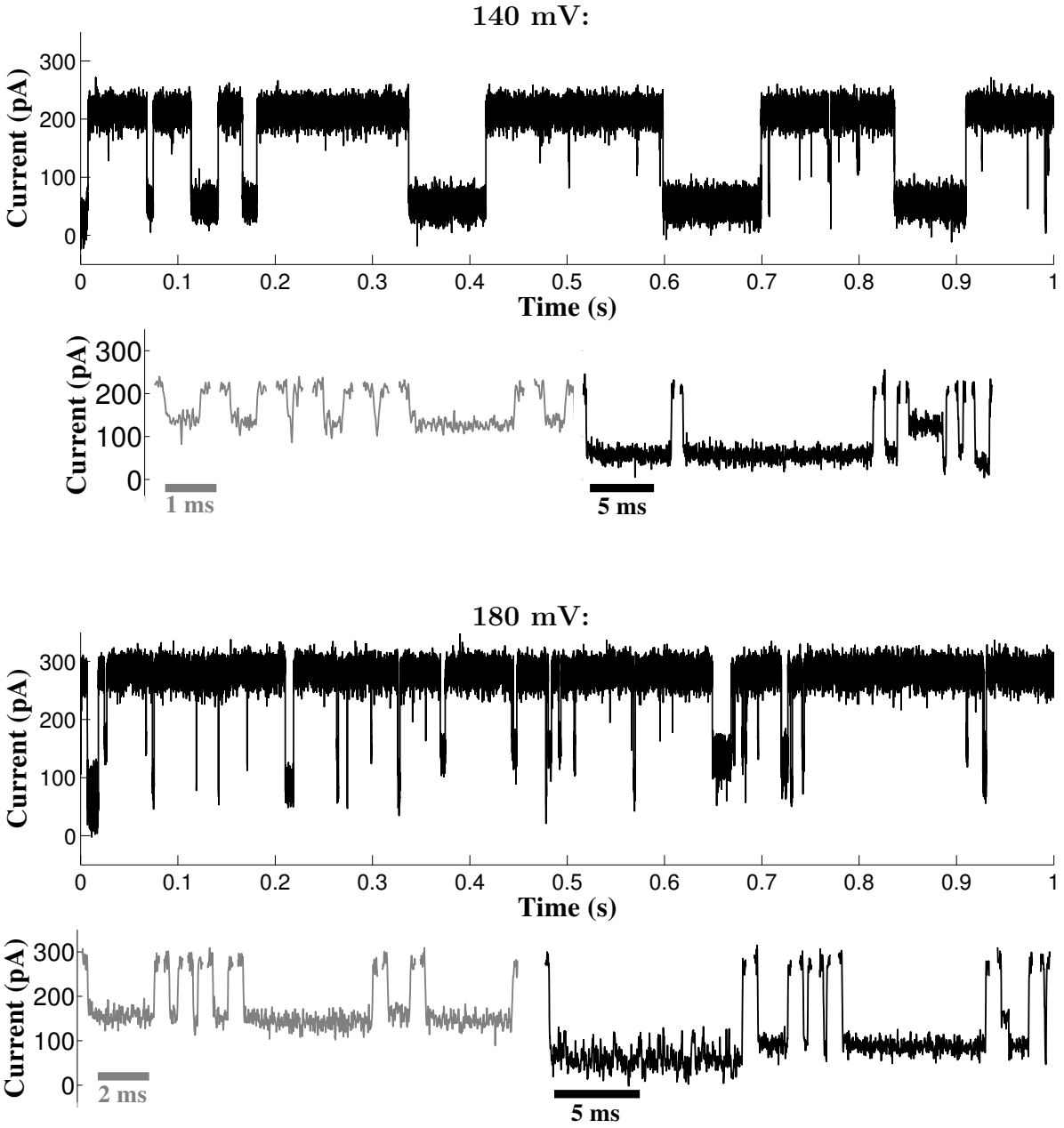

Figure 3.7: Current traces for translocation data for hairpin DNA constructs in a single MspA pore in a microfluidic-painted $PMOXA_{13}$-*b*-$PDMS_{47}$-*b*-$PMOXA_{13}$ membrane at 140 mV and 180 mV. The smaller plots show zooms of the first six partial blockades (in gray) and the first six deep blockades (in black) from each trace of the larger plots for blockades less than 20 ms in duration. It is clear from these traces that partial blockades increase in duration and deep blockades decrease in duration when voltage is increased. This data is part of the dataset used to compute statistics in Figures 3.8 and 3.9

of the current blockades were analyzed. Figure 3.8 shows scatter plots of an individual pore at 120, 140 and 180 mV. Current blockades for hairpin DNA commonly have two magnitudes based on the location of the hairpin DNA relative to the MspA [83]. Hairpins that translocate through the pore cause large dips in current (deep blockades) because the DNA occludes a large portion of the MspA constriction, which dominates the MspA conductance. On the other hand, hairpins that do not translocate through the MspA reside in the MspA vestibule and causes smaller dips in currents (partial blockades). The threshold used for discerning partial and deep blockades was determined to be 30% of the baseline current[5]. This differs from the value of 50% in Butler et al. due to our use of a hairpin with a T_{50} tail compared to A_{50}. It is this difference that allows for discerning bases during sequencing [85].

The scatter plots show that partial blockades tended to increase in dwell time with increased voltage, while deep blockades have the opposite trend. This is consistent with the description that partial blockades correspond to hairpins which escape back into the channel (the cis compartment), so that increasing voltage increases the barrier to escape; on the other hand, deep blockades correspond to hairpins which translocate through the pore, so that increasing voltage reduces the barrier to escape. These are the same trends that were reported in Butler et al. for a similar MspA mutant in a lipid membrane.

The partial blockade dwell times were fit well by an exponential function. Figure 3.9 shows that the time constant for partial blockade dwell time approximately doubles from 120 mV to 140 mV, and doubles again from 140 mV to 180 mV. These time constants are about 10 times greater than those reported in Butler et al. for 50 nt-long strands T_{50}

[5] The 10,000-point-smoothed baseline $I_B(t)$ was used, as computed in the previous section. The criteria for accepting and rejecting current dips as blockades is similar to those in Butler et al. [83]. Different thresholds between deep and partial events were used due to the difference in current associated with adenine and thymine, as described. Additionally, we used a 10-kHz filter, so blockades less than 100 µs were rejected. Similarly, due to our 100-kHz sampling rate, blockades were rejected if they occured within 30 µs of each other, compared to 26 µs in Butler et al.

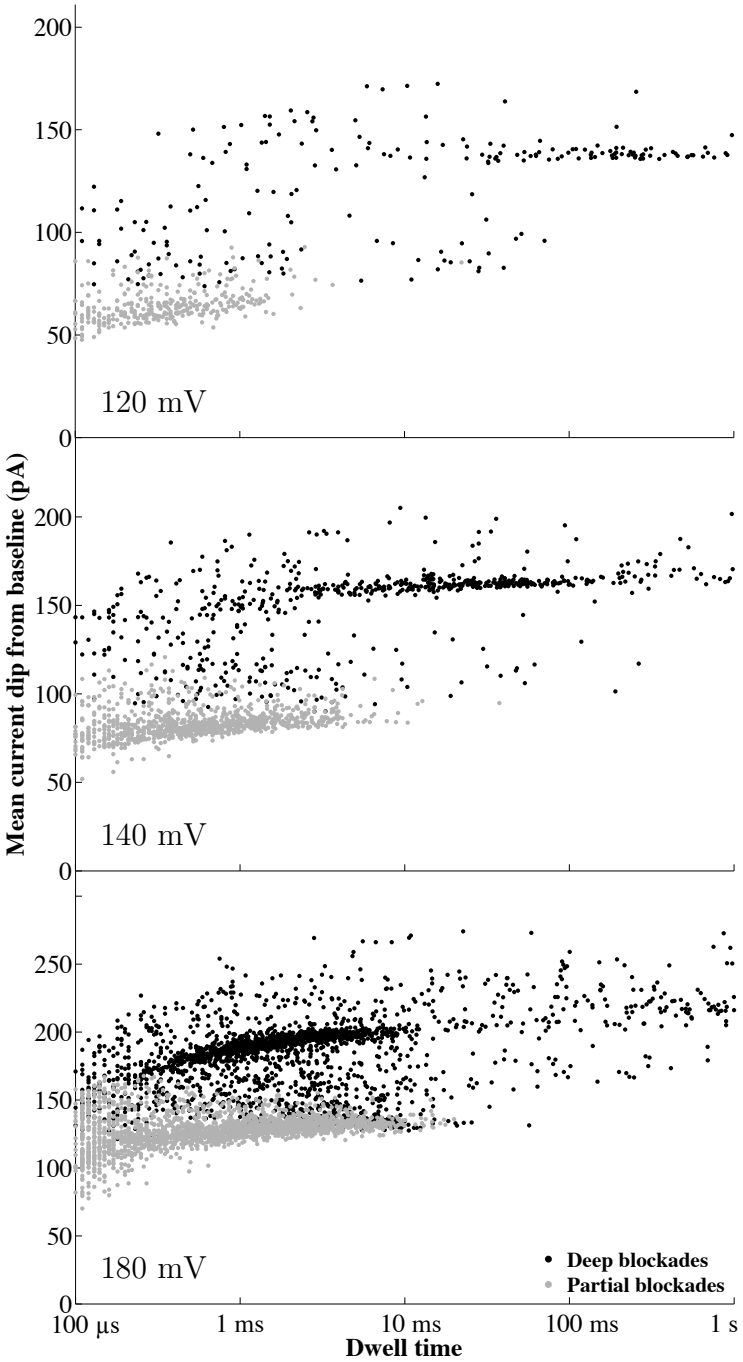

Figure 3.8: Scatter plots of mean blockade current vs dwell time. Shading was added to distinguish deep and partial events on the basis of maximum blockade current. The criteria for selecting and rejecting events for inclusion in these plots is described in Footnote 5. The slant in current dips is due to an RC time constant arising from the membrane capacitance and is fit well by $I_0(1 - e^{-t/\tau})$.

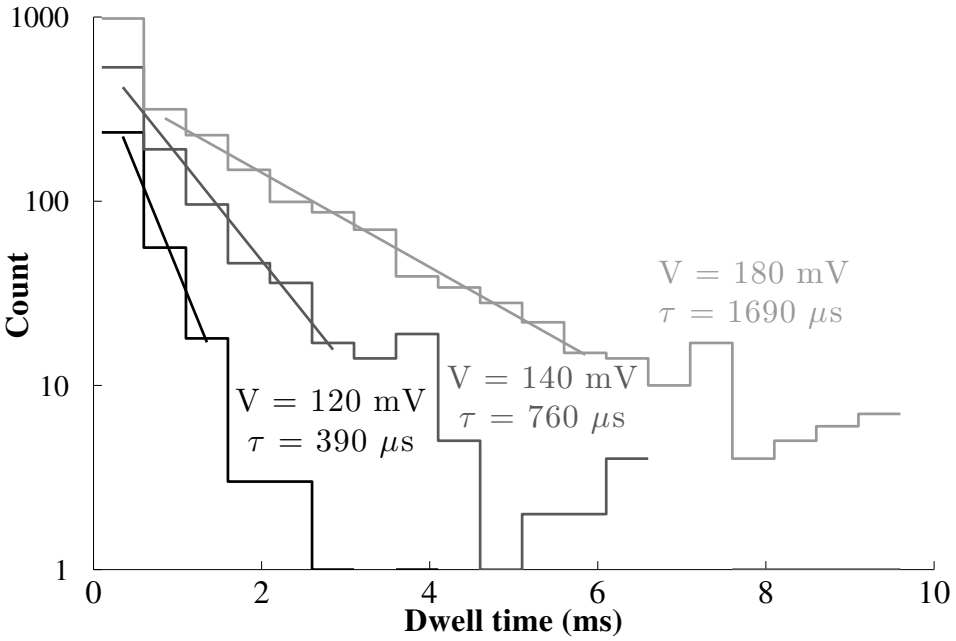

Figure 3.9: Histogram and fits of partial blockade data. Partial blockades are fit with simple exponentials with $r^2 > 0.98$. The first 0.25 ms bin was excluded from the fit for the 180 mV data, for which it was difficult to distinguish between partial and deep blockades due to the RC rise time. The 120 mV and 140 mV data were less sensitive to this effect. The criteria for selecting and rejecting events for inclusion in these plots is described in Footnote 5.

without a hairpin loop in M2MspA. This is likely due to the presence of the hairpin loop. Additionally, whereas blockades including both partial and deep current levels were rare in Butler et al. [83] for hairpins with M1MspA, they were more common in our system. This effect is likely due to the longer time constant for partial blockades: longer residence times increase the probability that a DNA molecule will ultimately translocate.

All of these results suggest that the same results would have been obtained if these experiments were repeated in phospholipid membranes. All deviations from the results of Butler et al. have justifications that rely on other differences in our experiments[6]. This suggests that the use of PMOXA-*b*-PDMS-*b*-PMOXA in an optimized system would compatible with the use of MspA for the application of DNA sequencing.

[6]We did not perform measurements in phospholipid membranes that would serve as a direct control to polymer membranes due to a shortage of time and resources.

Chapter 4

Experimental results for droplet interface bilayers

The previous chapter described experiments performed using $PMOXA_{13}$-*b*-$PDMS_{47}$-*b*-$PMOXA_{13}$ in aperture-suspended membranes, which allowed for the translocation of DNA through MspA nanopores. The results showed a large variability in MspA behavior, but also suggested the requirements for consistent, good MspA behavior. The approach was limited in that it did not allow for a measurement of bilayer thickness and tension, which are primary candidates for the cause of MspA variation.

On the other hand, droplet interface bilayers (DIBs) have been shown to allow the measurement of thickness and tension of phospholipid membranes using the Young-Lippmann equation [10]. In this chapter, we use DIBs with the goal of determining these properties for $PMOXA_{13}$-*b*-$PDMS_{47}$-*b*-$PMOXA_{13}$. We begin by describing the preparation and properties of polymer vesicle solutions. We demonstrate that poor adsorption dynamics of the polymer solutions causes loosely packed monolayers that cannot form stable bilayers. To solve this issue, we present a technique for manually packing monolayers so that they form stable bilayers.

An additional challenge was that the Young-Lippmann equation failed to describe $PMOXA_{13}$-*b*-$PDMS_{47}$-*b*-$PMOXA_{13}$ membranes due to their long equilibration timescale. In response to this, we established a new approach for measuring monolayer and bilayer tensions using droplet shape analysis via the Young-Laplace equation. We end the chapter by using this approach to determine monolayer and bilayer tensions for the DIBs made using $PMOXA_{13}$-*b*-$PDMS_{47}$-*b*-$PMOXA_{13}$.

4.1 Preparation and characterization of aqueous polymer solutions

The first step in DIB experiments is the preparation of a surfactant solution that adsorbs to form a monolayer at an oil-water interface. We prepared aqueous vesicle solutions by the solvent injection technique, in which the block copolymer is first dissolved in a solvent that dissolves both the hydrophobic and hydrophilic blocks. The solvent is miscible with water so that when the polymer-solvent solution is added to an aqueous solution, the solvent partitions into the water and the polymer forms aggregates [130]. Some solvent remains in the solution, but it may be removed partially via evaporation or more thoroughly via dialysis. The technique has the benefits of being simple and scalable [130]. Additionally, it has previously been demonstrated to yield unilamellar vesicles for PMOXA-*b*-PDMS-*b*-PMOXA [131].

Several aqueous solutions were made using $PMOXA_{13}$-*b*-$PDMS_{47}$-*b*-$PMOXA_{13}$ DIBs via the solvent injection technique. Acetone, ethanol, and tetrahydrofuran (THF) were used as solvents and Millipore water or buffered salt solution were used for the aqueous phase. The buffer solution was the same as in the previous chapter: 1M KCl, 10 mM HEPES, pH 8 in Millipore water. Agitation was applied by vortexing, sonicating,

or magnetically stirring the aqueous phase while the polymer solution was added; the agitation method used did not significantly affect the results, but there were causes for variation that could not be determined. Aggregate solutions were placed briefly in a rotary evaporator or were allowed to sit for a few hours to remove solvent. In some cases, the solution was dialyzed in buffer solution to remove residual solvent, but these solutions behaved similarly to solutions that were not dialyzed.

An important requirement for DIBs is that the aqueous polymer solution in a droplet must have enough polymer to form a complete monolayer on its surface in a reasonable timescale. To determine the concentration of polymer in vesicle form, nanoparticle tracking measurements were performed. The nanoparticle tracking equipment used (NanoSight NS300, Malvern Instruments) works by using an ultramicroscope to image the paths of nanoparticles over time. It then uses the two-dimensional position trace of each particle to determine its diffusion coefficient. The diffusion is due to Brownian motion, and the particle's hydrodynamic radius is related to the diffusion constant by the Stokes-Einstein equation. The NS300 software determines concentration by counting the number of particles in the viewable area. The solution is flowed between measurements to average over a sample. The result of a nanoparticle tracking measurement is a distribution of concentration against diameter, binned in 5 nm increments, provided by the NS300.

The molar concentration of polymer in vesicle form was calculated by performing a weighted sum over nanoparticle radii, assuming that all nanoparticles are unilamellar spherical vesicles:

$$c_{\text{vesicle}} = \sum_j 4\pi r_j^2 \Gamma c_j \tag{4.1}$$

where c_j is the concentration of vesicles of radius r_j in the j^{th} bin and Γ is the surface concentration of polymer molecules in units of [number]/[area]. As an estimate,

Solvent phase (wt.% polymer)	**Aq. phase**	**Vol.% solvent in aq.**	**Vesicle yield**	**$c_{vesicle}$ (mg/mL)**	**Solutions made**
2-10% in THF	water	5-20%	14-34%	0.2-1.5	6
8% in ACE	water	5%	15%	0.5	1
1.1% in EtOH	1M KCl	10%	4%	0.08	1
19% in EtOH	1M KCl	10%	2-4%	0.4-0.7	1
18-19% in EtOH	1M KCl	4%	3-4%	0.2-0.3	2

Table 4.1: Vesicle solutions prepared by the solvent injection method. Yield and concentration ranges arise either from different solutions or from multiple measurements of the same solution. In all cases, mean vesicle diameters were ~100 nm or larger. Smaller particles were not detected. None of these vesicle solutions could form stable DIBs in hexadecane without the shrink method introduced in the following section.

$\Gamma = 1$ nm^2 area was used[1]. A potential source of error in this calculation is that the nanoparticle tracking data could only provide particle sizes and could not distinguish between unilamellar vesicles, multilamellar vesicles, and solid spheres of precipitate.

In order to demonstrate the fraction of polymer converted to vesicles, c_{vesicle} was compared to the mass of polymer used to make the solution. A 100% vesicle yield indicates that the entire mass of polymer was converted to unilamellar vesicles. Yields below 100% indicate either a deviation from unilamellarity or a loss of polymer to precipitate or smaller aggregates that could not be detected[2]. Alternatively, the assumption that $\Gamma = 1$ nm^2 could lead to error. We also note that the nanoparticle tracking was not calibrated against a standard of known concentration. For these reasons, the computed yields should be viewed with some caution.

Table 4.1 shows results for selected aggregate solutions made via solvent injection. For ethanol, 2-4% of the polymer introduced is converted into vesicles, while for the

[1]A reference with the surface concentration in PMOXA$_{13}$-*b*-PDMS$_{47}$-*b*-PMOXA$_{13}$ vesicles could not be found, but the value of ~2.5 nm^2 from the polymer with different block lengths when compressed at an air/water interface [132] is an upper bound. Using this value instead of 1 nm^2 would give c_{vesicle} and vesicle yields that are 2.5x lower for this entire section, for which the same arguments would apply.

[2]In theory, the turbidity as well as other scattering techniques could be used to better determine the lamellarity of solution.

other solutions, above 14% is converted. For comparison, an aqueous solution of DPhPC prepared by rehydration according to the protocol in Taylor et al. [10] gave yields between 21% and 48% under the same assumptions (e.g. $\Gamma = 1$ nm^2). Although the yield was very low for ethanol injection, there was relatively little precipitate visible. To test the possibility of multilamellar vesicles, some solutions were prepared by either sonication or extrusion, both of which are known to induce unilamellarity [133]. Neither of these had a noticeable effect on yield. For example, one solution with a yield of 2.5% was passed 21 times through a 100 nm extruder (NanoSizer Liposome Mini Extruder, T&T Scientific), but the yield was unchanged when measured again.

To investigate further, some solutions were analyzed using dynamic light scattering (DLS) to determine if smaller aggregates were present. DLS measurements use an aggregate measure of the Brownian motion statistics using light scattering and allow for measurement down to ~1 nm. In contrast to nanoparticle tracking, DLS does not measure absolute concentration and works better for monodisperse samples. Additionally, DLS measurements are not as sensitive to low particle concentrations. This means that a combination of DLS and nanoparticle tracking analysis can provide a more accurate picture of a sample than either one alone.

DLS measurements were performed on a Zetasizer Nano SZ (ZEN3600, Malvern Instruments) with a 632.8 nm laser and are shown in Table 4.2. They reveal that ethanol-based solutions have sizable number of smaller aggregates that were not detected by nanoparticle tracking. On the other hand, smaller aggregates were not detectable in acetone- and THF-based solutions, which likely accounts for the discrepancy in the vesicle yields. The intensity of the signal due to the smaller aggregates is roughly the same as that of larger aggregates. For scattering by solid spheres much smaller than the wavelength of light, the scattered intensity increases as the third power of the diameter [134], so that the approximately fivefold difference in diameter would correspond to ~125 times

Solvent phase (wt.% polymer)	**Aq. phase**	**Vol.% solvent in aq.**	d_1 **(nm) (st. dev.)**	$\mathbf{I_1}$ **(%)**	d_2 **(nm) (st. dev.)**	$\mathbf{I_2}$ **(%)**
10% in THF	water	5-20%	142 (57)	26.3	1020 (696)	68.9
8% in ACE	water	5%	318 (63)	100	N/A	0
19% in EtOH	1M KCl	10%	38 (18)	52.3	219 (124)	47.7%
18-19% in EtOH	1M KCl	4%	29 (8)	41.4	169 (48)	58.6%

Table 4.2: DLS data for vesicle solutions in Table 4.1. d_1 and d_2 are the intensity-weighted mean diameter of aggregates in the solutions and I_1 and I_2 are the integrated intensities for the distribution about each mean. The intensity-weighted mean is related to but distinct from the number-weighted mean, so that e.g. d_2 for ethanol does not contradict the mean value of 100 nm determined from nanoparticle tracking measurements noted in the text.

more small aggregates than large ones. In our case, however, the scatterers are spherical shells, so that the math is different and the intensity is a complicated function of diameter. In Section A1 of the appendix, the function is used to determine that the amount of polymer in the smaller aggregates c_{micelle} is likely a few times larger than c_{vesicle}.

The number distributions calculated assuming solid spheres gives a mean hydrodynamic diameter of 16.5 nm (st. dev. 4.9 nm) for the ethanol-formed solution with the highest concentration. For comparison, PMOXA_6-*b*-PDMS_{44}-*b*-PMOXA_6 vesicles have been shown to have a bilayer thickness of 10.7 ± 0.7 nm by cryo-TEM imaging [135]. Using this as a minimum-bound for our polymer, which must form thicker bilayers due to the additional PMOXA and PDMS groups, the thinnest possible vesicle would be about 22 nm in diameter. Because the aggregates we see here are mostly smaller than this, they must necessarily be micelles. We note that while the hydrophilic ratio of PMOXA_{13}-*b*-PDMS_{47}-*b*-PMOXA_{13}, $f = \dfrac{2 \times 1{,}100 \text{ g/mol}}{(3{,}500 + 2 \times 1{,}100) \text{ g/mol}} = 39\%$, predicts the formation of vesicles, such predictions are only a rule of thumb [101]. Cryo-TEM images for PMOXA_6-*b*-PDMS_{44}-*b*-PMOXA_6 and PMOXA_7-*b*-PDMS_{49}-*b*-PMOXA_7 also appear to show smaller aggregates that are 10-15 nm in diameter in addition to larger vesicles [135].

An estimate of c_{vesicle} can be used to determine whether enough polymer is present to form a full monolayer on a DIB surface. For a droplet of radius r, the enclosed number of polymer molecules in a droplet is $N_{\text{V}} = VcN_{\text{A}} = \frac{4}{3}\pi r^3 cN_{\text{A}}$ where c is the molar concentration and N_{A} is Avogadro's number. The number of molecules needed to form a monolayer at the droplet surface is $N_{\text{S}} = \Gamma A = 4\pi r^2 \Gamma$ where Γ is again assumed to be 1 nm^2. The ratio $N_{\text{V}}/N_{\text{S}} = \dfrac{N_{\text{A}} cra}{3\Gamma}$ then indicates the relative abundance of polymer in the droplet, where $N_{\text{V}}/N_{\text{S}} = 1$ corresponds to the case where there is just enough polymer available to form a complete monolayer. This only serves as a minimum theoretical limit. In practice, there should be an overabundance of polymer in the droplet so the adsorption rate is not limited by long diffusion times or a finite desorption rate.

For our polymer, $c_{\text{vesicle}} = 0.4$ mg/mL was the lowest vesicle molar concentration attained when aiming for solutions with high aggregate concentration. We will use this as a worst case estimate of whether there is enough polymer present to form monolayer. Typically DIB droplets are 200 nL in volume (approximately a 350 µm radius). Using this with average molecular weight of 5,700 g/mol, a concentration of 0.4 mg/mL corresponds to $N_{\text{V}}/N_{\text{S}} = 5$. Thus, at this concentration, the average concentration will not drop by more than 20% of its original value.

To determine whether diffusion will have a limiting effect, we consider how far vesicles must diffuse to form a full monolayer and then calculate the corresponding diffusion time. Rather than solving the diffusion equation for this geometry, a simple algebraic estimate is made using the diffusion timescale. For $N_{\text{V}}/N_{\text{S}} = 5$, only 20% of the vesicles in a volume are needed to form a complete monolayer. Because half of the aggregates near the surface will diffuse toward the surface, we require the outwardly diffusing aggregates in the 40% of the volume closest to the surface. For a 200 nL spherical droplet, this is the region within 57 µm of the surface. We treat this spherical shell as planar as an approximation. Then we can estimate the diffusion time for all aggregates in this region

by using the average diffusion time for aggregates 57 µm from the surface.

For a single particle diffusing in one dimension, its mean squared displacement is $\langle x^2 \rangle = 2Dt$ so that the time to diffuse a distance of 57 µm is $t = \frac{(57\ \mu\text{m})^2}{2D}$. The Stokes-Einstein equation provides the diffusion constant D for spherical particles in a liquid at low Reynolds number: $D = \dfrac{k_\text{B}T}{6\pi\eta r}$, where η is the dynamic viscosity and r is the radius of the particle. Using the average vesicle diameter of 100-nm from the nanoparticle tracking data gives $D = 4\ \mu\text{m}^2/\text{s}$ and $t = 6$ minutes. This means that diffusion will not significantly delay the adsorption process at $c_\text{vesicle} = 0.4$ mg/mL. If every polymer that reaches the droplet surface adsorbs, these values would give the equilibration timescale for a full monolayer. If, in the opposite extreme, polymer adsorption is very slow, then these favorable diffusion timescales would keep the concentration near the surface above 80% of the initial value throughout the process.

For the smaller aggregates, the average diffusion constant is at least 5 times higher because the diameter is ~15-20 nm instead of ~100 nm. Then, assuming the molar concentration is $c_\text{micelle} = 0.4$ mg/mL also, the diffusion timescale is at most 1 minute. As mentioned above and calculated in Section A, c_micelle is likely a few times higher than 0.4 mg/mL. This means that for ethanol injected solutions, there is independently an overabundance of both micelles and vesicles for droplets larger than 200 nL. If the adsorption kinetics of either micelles or vesicles is dominant, ethanol based solutions will give the best or nearly the best monolayer formation results of the solutions tested. Time limitations prevented the study of whether adsorption occurred primarily from micelles or vesicles.

4.1.1 Dynamics of monolayer formation

Figure 4.1 shows an image of a pendant drop of aqueous $PMOXA_{13}$-*b*-$PDMS_{47}$-*b*-$PMOXA_{13}$ solution in hexadecane, along with a plot of its interfacial tension over time. The monolayer tension after 15 minutes is ~25 mN/m, which is an order of magnitude larger than phospholipids, e.g. 1.18 ± 0.2 mN/m for DPhPC and 1.99 ± 0.5 mN/m for DOPC [136]. Such high interfacial tension indicates exposure between the oil and water phases due to poor polymer packing. Pairs of droplets prepared this way typically fused either on contact or a few minutes after formation, even after waiting several hours prior to contact. Bilayers were not stable when formed in a bath of hexadecane, silicone oil AR 20, or mixtures of decane or D4 with squalene. Bilayers were sometimes stable when formed in a bath of pure decane or pure D4. The high thickness associated with membranes formed in decane or D4 (~20 nm according to the measured ~0.1 µF/cm^2 specific capacitance) stabilized the bilayers despite their poor polymer packing. These results held for all aqueous polymer solutions tested, including those formed from THF or acetone, although all polymer solutions were not tested with all oils.

Considering that diffusion is not limiting, the monolayer tension trace in Figure 4.1 implies that there is a large barrier to the adsorption process. In the initial stage of adsorption, adsorption is so fast that the tension is kept below 30 mN/m even as the droplet is dispensed. Below 30 mN/m, adsorption slows nearly to a stop. Longer-term measurements (data not shown here) showed that tension remained above 20 mN/m for hours despite the large over abundance of polymer due to the large droplet size (~5 µL). For comparison, the polymer-free control is shown to be above 50 mN/m and slowly decreasing due to trace contaminants, as expected for hexadecane (99%, Alfa Aesar) used as received [137][3].

[3]The inclusion of 1M KCl in the buffer serves to increase the tension only by ~1.5 mN/m [138] relative to pure water.

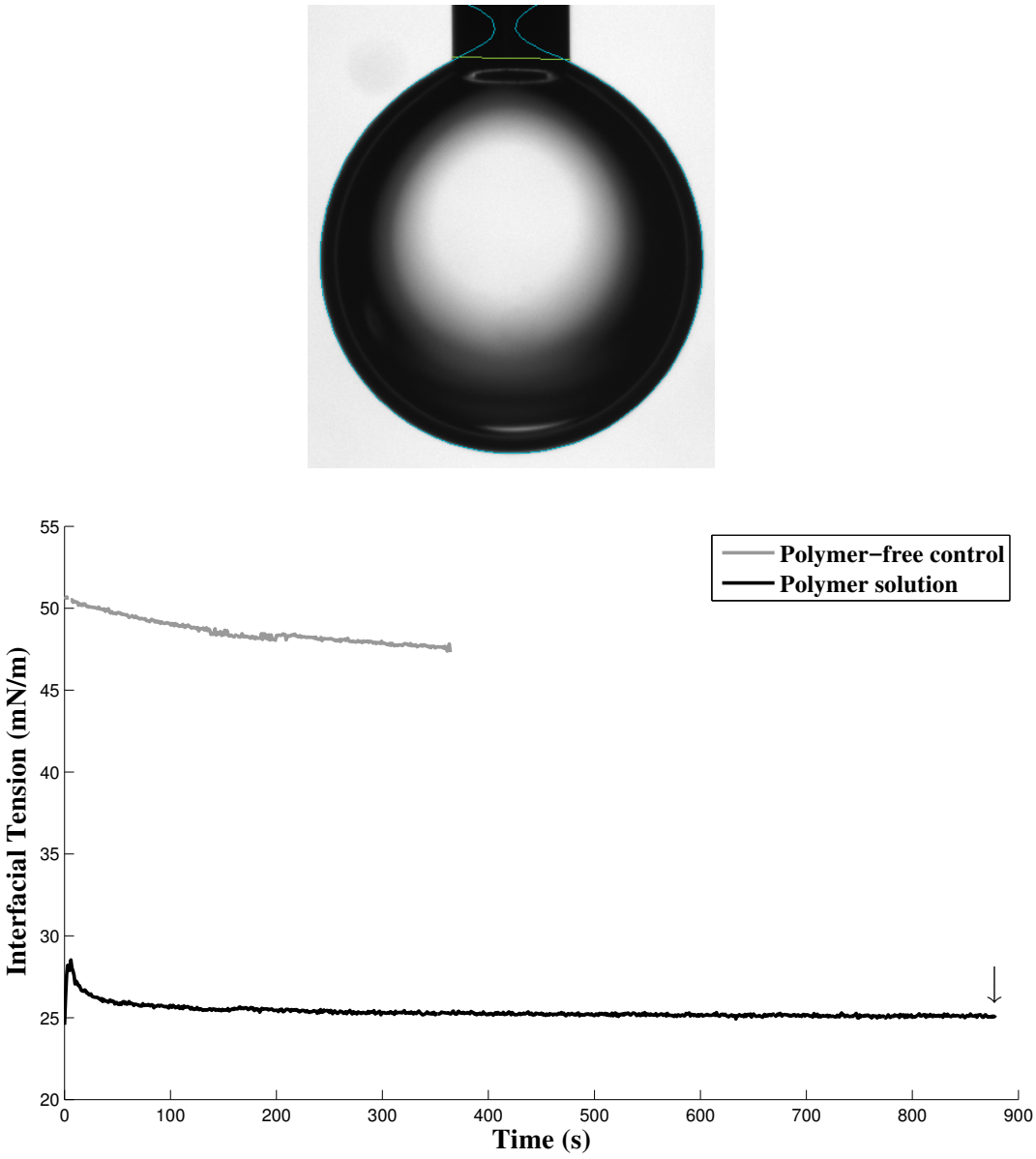

Figure 4.1: Pendant droplet image with fit line and plot of interfacial tension of aqueous droplets in hexadecane. The polymer solution was made in ethanol and contains both micelles and vesicles. The control data (in gray) used the same buffer (1 M KCl, 10 mM HEPES, pH 8) without polymer added. The data was obtained with a commercial pendant drop apparatus using OneAttension software. Each data point corresponds to an image which was fit with the Young-Laplace equation to determine tension. The image above corresponds to the datapoint denoted by the arrow. A longer continuous trace was not taken for the control, but the tension eventually dropped to ~30-35 mN/m due to surfactant activity of contaminants and potentially the HEPES buffer. For scale, the width of the needle is 0.51 mm

For phospholipids, Venkatesan et al. [136] observed a two stage process, which they attributed to two different mechanisms of adsorption: aggregate adsorption and single-molecule adsorption. Initially, the oil-water interface is bare so that entire aggregates may fuse onto it. Once the monolayer is moderately packed, this pathway becomes hindered. At this stage, adsorption continues at a slower rate with single molecules. Our polymer seems to behave similarly: the first adsorption stage may be attributed to faster aggregate adsorption while the second adsorption stage may be attributed to slower single molecule adsorption.

The process of adsorption is similar to the process of evolution in a micellar solution, which can also have two stages. When a micellar system is far from equilibrium, entire aggregates fuse together in a single step; but when a micellar system is nearer to equilibrium, the relaxation occurs through a single molecule exchange process [139]. The kinetics of this process for block copolymers are often far slower than phospholipids due to the larger size of both the hydrophobic and hydrophilic blocks [104, 140]. It has been demonstrated that the kinetics of single molecule exchange are hypersensitive to the molecular weight m_{B} of the hydrophobic block. This occurs because the hydrophobic block is exposed to the hydrophilic region during its transit [141], so that the associated activation energy scales as $m_{\mathrm{B}}^{2/3}$ or m_{B} [104]. Additionally, the hydrophilic blocks of adjacent molecules must be displaced for a molecule to pass through. This implies that in our case, as the monolayer becomes more packed, the hydrophilic blocks on the interface become increasingly difficult to displace so that the barrier to adsorption increases [104]. In view of the large molecular weight of both our hydrophilic and hydrophobic blocks relative to phospholipids, it is not surprising that the monolayer tension remains above 20 mN/m during adsorption.

4.2 Preliminary experiments on monolayers and bilayers of block copolymer DIBs

4.2.1 Shrinking droplet approach to DIBs

The source of bilayer instability in $PMOXA_{13}$-*b*-$PDMS_{47}$-*b*-$PMOXA_{13}$DIBs is poor monolayer packing at the interface, evidenced by monolayer tensions above 20 mN/m. Thus, a modified approach was conceived to manually compress the monolayers enough so that the droplets would not fuse on contact. The approach is demonstrated in Figure 4.2. First a droplet of aqueous polymer solution is pushed out through the needle into a bath of oil. After waiting for the polymer to adsorb onto the surface, most of the droplet volume is withdrawn. As the droplet surface area decreases, the area per molecule also decreases if the monolayer does not redistribute into the bulk and the monolayer does not slip at the contact point with the pipette.

This principle was adapted for use with DIB experiments. First a 2-µL droplet of vesicle solution is held suspended from the pipette tip for several seconds for the first phase of monolayer formation to complete. Then the droplet is withdrawn slowly back into the pipette. If the polymer in the monolayer does not leave the interface, this increases the monolayer packing. This is accompanied by a reduction in interfacial tension so that the droplet is distorted by gravity. Eventually the interfacial tension can no longer support the weight of the droplet hanging beneath it, and a part of the droplet separates and falls down. If the droplet is held to envelop the agarose-tipped ball electrode throughout this process, the separated droplet remains attached to the electrode. This process is repeated to form two droplets which are used to form a DIB.

Figure 4.3 shows images and monolayer tension traces of droplets prepared this way. In all cases the monolayer tension rises until it plateaus after about 5 to 20 minutes.

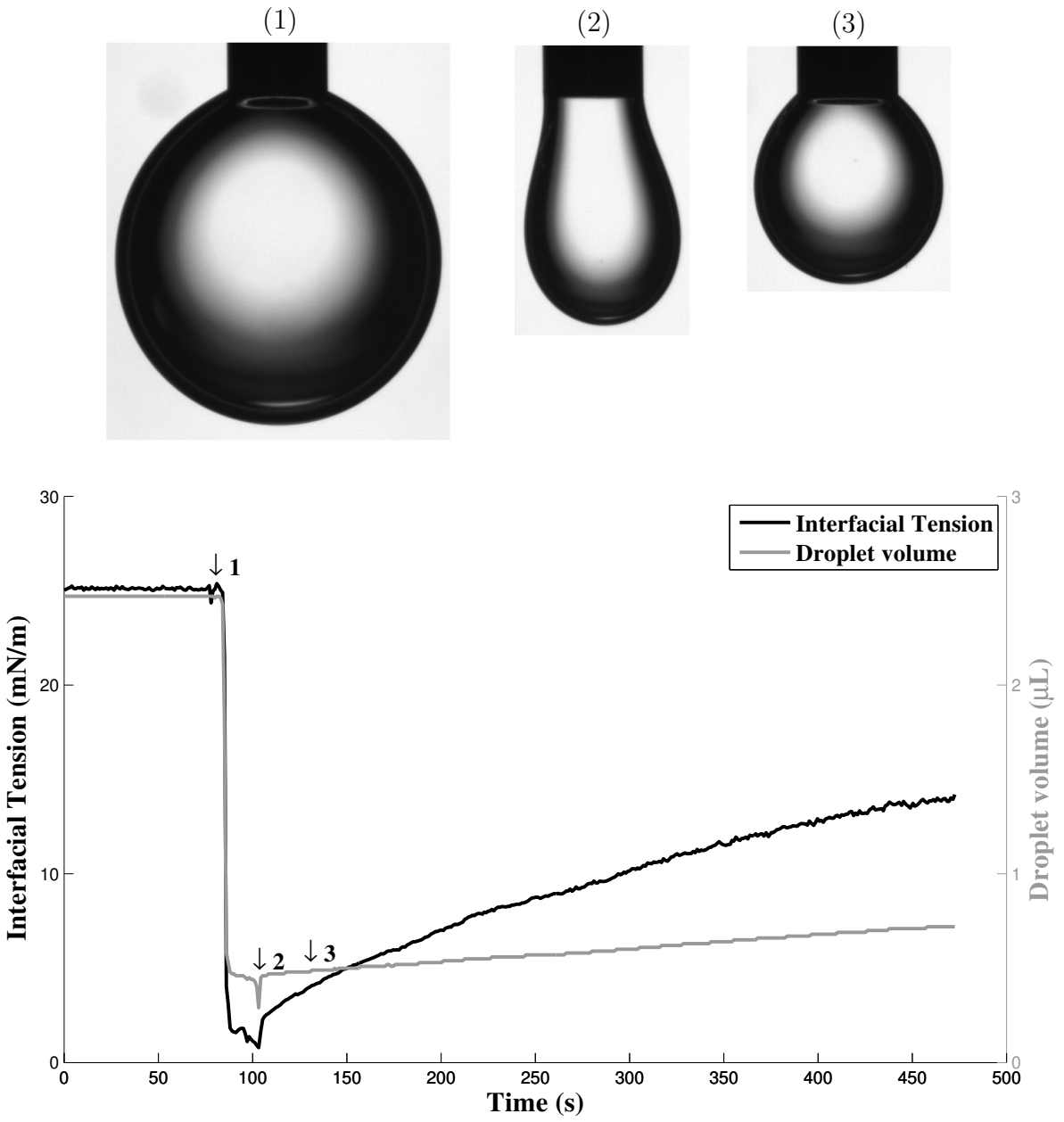

Figure 4.2: A demonstration of the droplet shrinking technique to increase the packing of the polymer monolayer. As solution is manually sucked back in through the needle, the droplet volume decreases and as a result the interfacial tension decreases also. The fits of the images above provided the volume and tension values indicated by the numbered arrows in the plot as in Figure 4.1. For scale, the width of the needle is 0.51 mm. The steady increase in volume was due to the use of a disposable syringe with poor control over the dispensed volume. The steady rise in interfacial tension is due to the volume increase and potentially also due to leakage of polymer molecules out of the monolayer.

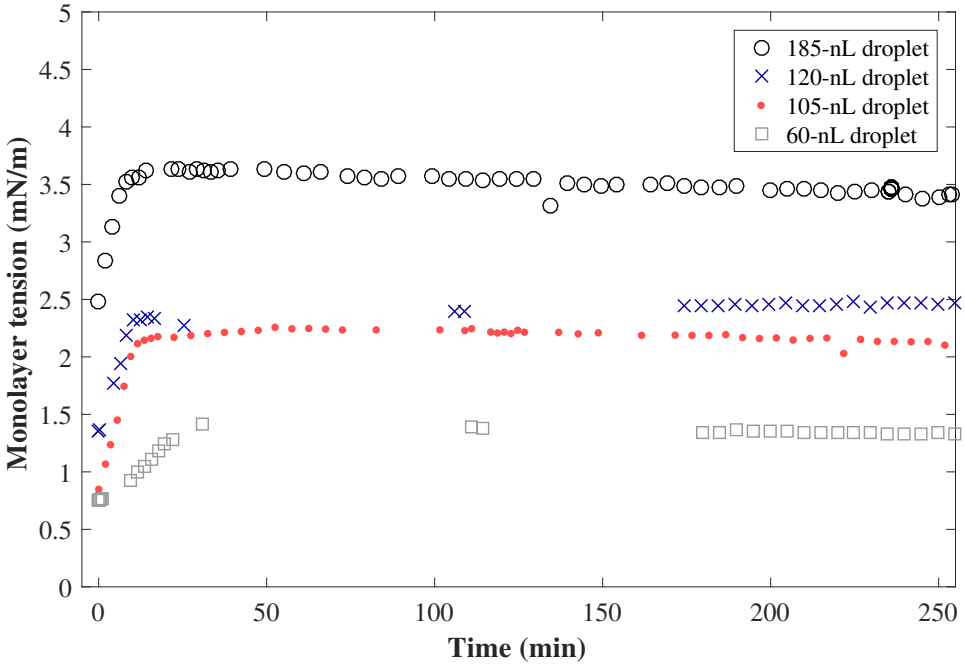

Figure 4.3: Monolayer tension traces for aqueous $PMOXA_{13}$-*b*-$PDMS_{47}$-*b*-$PMOXA_{13}$ droplets made using the shrinking approach and suspended from ball electrodes in a bath of hexadecane. First, a 2-µL droplet was held to envelop the ball electrode for about 30 seconds. Then the droplet was slowly withdrawn until the monolayer tension could no longer support its weight, so that a small part of the original droplet fell off onto the electrode. t = 0 marks the instant at which droplets detached from the pipette onto the electrode, but the first datapoint is between 40 and 105 seconds after this[4]. After an initial rise, the monolayer tensions remain constant over time. The monolayer tensions were determined via pendant drop fits made using Pendant Drop on ImageJ after preprocessing the images as will be described later in the text. The gaps in the data usually denote times when measurements were not made, but sometimes are a result of an error during analysis. The drifts and fluctuations in the tensions may result from measurement artifacts such as movement of the camera arm or from genuine changes in tension. Such changes in tension could arise from changes in the ambient temperature or from changes in droplet volume due to evaporation via wetting of the electrode wire.

The fact that the tension is stable over several hours shows that the number of polymer molecules in the monolayer is nearly constant. This proves that $PMOXA_{13}$-*b*-$PDMS_{47}$-*b*-$PMOXA_{13}$ behaves as a Langmuir monolayer on at least a several-hour timescale and additionally that there is no leakage of polymer from the monolayer where it meets the electrode.

The droplet shrinking process uses the same principle as a Langmuir trough experiment, which was illustrated in Figure 2.4. A Langmuir trough experiment begins by spreading a known quantity of amphiphile dissolved in a volatile solvent onto the surface of a tank of water. The amount of amphiphile used is small, so that after the volatile solvent evaporates the amphiphile is initially in a two-dimensional gas phase on the water surface. Then the surface area of the monolayer is reduced by moving a sliding barrier as the surface tension is measured. The area per molecule is calculated by dividing the total number of amphiphiles by the area enclosed by the barrier. Together, the surface tension and area per molecule comprise the desired Π–A isotherm.

This principle has already been exploited to use pendant drops to determine Π–A isotherms of Langmuir monolayers at water/air [142, 143] and water/oil interfaces [144]. First, a much smaller droplet of an amphiphile in solvent is spread onto an amphiphile-free pendant drop as the initial step. Then, as the droplet volume is reduced, its shape is analyzed to determine its surface area and tension at each instant, yielding the desired Π–A isotherm. The difference in our approach is that our polymer is introduced to the interface by adsorption, so that the area per molecule is unknown and a Π–A isotherm cannot be obtained.

One of the design criteria for a Langmuir trough experiment is the minimization of the amount of amphiphile that leaves, or "leaks" out of, the interface. Amphiphile that

[4]The reason for the delay before the first datapoint is that a video was recorded with the side camera during and after droplet dispension to capture the initial quick rise in tension at high frame rate. However, the video data has not yet been analyzed so it is not plotted here.

leaks to the adjacent phases leads to an error in the area per molecule in a Π–A isotherm, and can also prevent interrogation of the low-area regime. The amount of amphiphile leakage is based on the barrier material as well as the properties of the amphiphile and adjacent phases. For example, it has been shown that Delrin barriers reduce the amount of a phospholipid lost at the barrier when compared to Teflon barriers [145]. The pipette tips that we use (Gilson Diamond) are composed of pure polypropylene, which has a hydrophobicity intermediate to Delrin and Teflon. This suggests that while leakage may occur during the shrinking process for $\mathrm{PMOXA_{13}}$-*b*-$\mathrm{PDMS_{47}}$-*b*-$\mathrm{PMOXA_{13}}$, it is likely not greater than it would be for Teflon, which remains a popular material for Langmuir troughs. In our case, the amount of leakage that occurs during the shrinking stage is small enough that it is irrelevant.

On the other hand, once the droplet is transferred to the agarose-coated electrode, leakage of polymer out of the interface becomes relevant to the experiment. Any leakage of polymer will cause the packing of the monolayer to decrease and the interfacial tension to increase, a process which cannot be reversed due to the slow adsorption rate demonstrated in Figure 4.1. Images of shrunk droplets suspended on ball electrodes show that the droplet is initially in contact with the agarose. As the monolayer tension rises, the droplet climbs up the agarose until it reaches the wire, at which point the tension plateaus. The leakage of polymer occurs when the monolayer is in contact with agarose, but not when it is in contact with the AgCl of the electrode.

At equilibrium, the force exerted by the monolayer tension along the circumference of the electrode must support the weight of the droplet. The supporting force due to monolayer tension is given by $F_\mathrm{s} = 2\pi r_\mathrm{e}\gamma_\mathrm{m}\cos\theta_\mathrm{C}$, where θ_C is the contact angle as illustrated in Figure 2.2 and r_e is the electrode radius at the contact line. Let us consider a droplet that is initially in equilibrium while in contact with the 50-µm-diameter wire of the electrode. If the monolayer tension is decreased by the increasing the packing of

the monolayer, then F_s will no longer be able to support the weight of the droplet. The droplet will fall until it reaches the larger circumference of the ball of the electrode, and it will stop when F_s at the new circumference again balances the weight of the droplet. If, as in our case, the monolayer tension is increased in this position, the droplet will rise until equilibrium is reached again. This phenomenon has been noted before in DIBs: the lowering of a droplet from the electrode wire to the ball is used as a signal that lipid monolayer packing is dense enough for stable bilayer formation [47]. This phenomenon also explains the purpose of the ball electrode: without it, droplets of low monolayer tension would slide off the electrode.

In general, the contact angle θ_C will also vary with monolayer tension. However, this is not usually the case if $\theta_C = 0$, which often holds at the oil/water/electrode interface. Images show that the contact angle of the droplet on agarose and AgCl are very small. Additionally, the 0° contact angle with the electrode wire is evidenced by the slow reduction of droplet volume over time that is observed in all oils tested; a droplet will gradually lose on the order of half its volume over the course of 24 hours, depending on its initial size. Because water is insoluble in oils such as hexadecane or AR 20, the only way this can occur is if a thin film of water wicks up the electrode and evaporates, which indicates complete wetting. For comparison, droplets that were submerged for several days in hexadecane without contact to an electrode did not noticeably change in size, as expected for an oil that is so immiscible with water. The 0° contact angle of water on agarose is likely owing to the high percentage of water in agarose and the nonpolarity of the surrounding oil. Thus we can consider simply that $F_s = 2\pi r_e \gamma_m$ in our case because $\cos\theta_C$ is equal to 1 or very close to it.

This behavior makes it possible to control the monolayer tension of the droplet simply by controlling the volume of the dispensed droplet. To determine the relation between dispensed volume and γ_m we balance F_s with the weight of the droplet. In the case of

a pendant drop, there is a correction to the droplet weight that arises from the Laplace pressure. The higher pressure inside the droplet acts to push against the electrode, effectively increasing the droplet weight. To determine this excess pressure at the contact line, we begin with the value of the Laplace pressure at the bottom of the droplet, $P_0 = 2\gamma_{\mathrm{m}}/r_0$ where r_0 is the radius of curvature at the droplet bottom as discussed in Section 2.4. Then we subtract off the hydrostatic pressure difference between the droplet bottom and the contact point $P_h = \Delta\rho g h_{\mathrm{drop}}$, where $\Delta\rho$ is the density difference between the oil and aqueous phases. The additional weight due to the Laplace pressure is then $\pi r_{\mathrm{e}}^2(P_0 - P_h)$. r_0 and h_{drop} can be determined for a droplet from pendant drop fitting or by solving the pendant drop equation; but for the sake of simplicity and to demonstrate that volume is fully predictive of monolayer tension, we estimate both of them from the droplet volume under the approximation that the volume is spherical. This approximation gives $r_0 = \sqrt[3]{\frac{3V}{4\pi}}$ and $h_{\mathrm{drop}} = 2r_0$. Values calculated this way overestimate r_0 by 3-5% and underestimate h_{drop} by 12-16% relative to pendant drop fits for the four datapoints in Figure 4.3. These result in an error in the monolayer tension below ~1%.

Balancing F_{s} with the effective droplet weight gives the exact formula:

$$2\pi r_{\mathrm{e}}\gamma_{\mathrm{m}} = \Delta\rho g V_{\mathrm{d}} + \pi r_{\mathrm{e}}^2(2\gamma_{\mathrm{m}}/r_0 - \Delta\rho g h_{\mathrm{drop}})$$

Solving this equation for γ_{m} and plugging in the estimates for r_0 and h_{drop} in terms of the droplet volume gives:

$$\gamma_{\mathrm{m}} = \frac{\Delta\rho g}{2\pi r_{\mathrm{e}}} \times \frac{V_{\mathrm{d}} - \pi r_{\mathrm{e}}^2 \sqrt[3]{\frac{3V_g}{4\pi}}}{1 - r_{\mathrm{e}}\sqrt[3]{\frac{4\pi}{3V_g}}} \tag{4.2}$$

where a distinction is made between the volume dispensed, V_{d}, and the geometric volume,

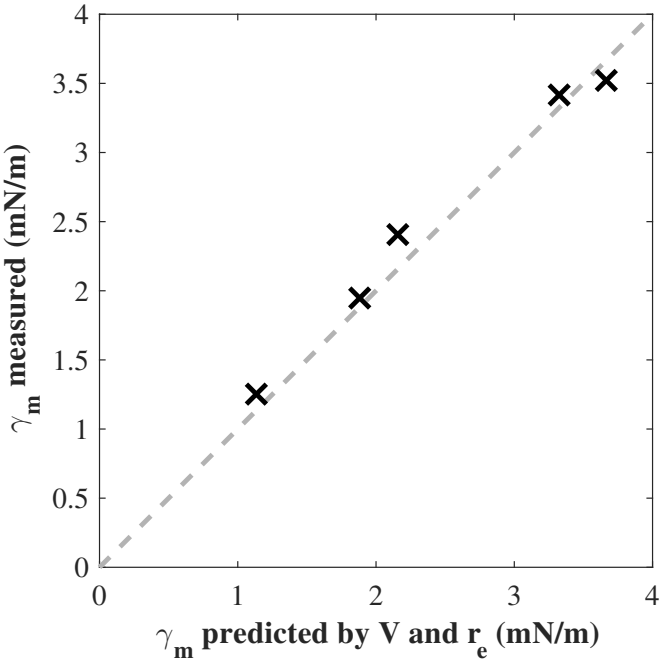

Figure 4.4: Scatter plot showing that the radius of the electrode wire r_e and the droplet's volume V determines its monolayer tension via the mechanism described in the text for shrunk droplets of aqueous $PMOXA_{13}$-*b*-$PDMS_{47}$-*b*-$PMOXA_{13}$. On the horizontal axis is the value of the monolayer tension predicted by Equation (4.2). On the vertical axis is the monolayer tension measured by pendant drop fitting. The monolayer tension traces of four of the five datapoints are shown in Figure 4.3 and the tension value for all droplets was averaged as described later in Table 4.3. The percentage error of the predicted values in comparison to the measured values ranged from -11% to 4%.

$V_g = V_d + V_{electrode}$, which includes the volume of the ball electrode. The volumes V_g are taken from the surface of revolution of the pendant drop profile, while the volumes $V_{electrode}$ are estimated from the width and height of the ball by assuming it to be a prolate spheroid undistorted by lensing due to the droplet shape. $V_{electrode}$ varied between 16 nL and 19 nL when estimated this way. r_e was taken to be 25 µm in all cases based on the nominal 50 µm diameter of the Ag wire. Figure 4.4 demonstrates the ability of Equation (4.2) to predict γ_m a priori for five droplets of different sizes.

This behavior applies exclusively to our particular system, in which amphiphile leaks out of the monolayer when in contact with the agarose but not when in contact with

bare Ag/AgCl. It can only be observed for a Langmuir monolayer for which adsorption from the adjacent bulk does not replenish amphiphile that leaks out of the monolayer. This implies that for a given oil the tension in a shrunk droplet of aqueous $PMOXA_{13}$-*b*-$PDMS_{47}$-*b*-$PMOXA_{13}$ can be controlled either by varying the droplet volume or the electrode wire diameter. Additionally, oils with a density closer to that of water will be associated with smaller tensions at the same droplet volume and electrode diameter, assuming that the initial monolayer tension falls within a range.

4.2.2 Bilayer formation experiments

When droplets of $PMOXA_{13}$-*b*-$PDMS_{47}$-*b*-$PMOXA_{13}$ solution are deposited using the shrinking approach, they form a stable bilayer. For example, in hexadecane the bilayers are stable with a specific conductance of 0.5 nS/mm^2 up to around 400 mV. An important aspect of these bilayers is they do not achieve equilibrium even after several hours. Their slow equilibration means that the Young-Lippmann equation cannot be used, so that the monolayer and bilayer tensions cannot be determined using the method of Taylor et al. [10].

The slow equilibration is demonstrated in Figure 4.5, which plots the response of the monolayer-bilayer contact angle to a step in voltage for aqueous polymer and aqueous lipid DIBs. DPhPC was used as the lipid, made with same 1M KCl buffer as the polymer[5]. For DPhPC, the response to the 100-mV step is abrupt and the contact angle achieves its new equilibrium value within a minute. For polymers, the contact angle is steadily rising prior to the voltage step, even after waiting over an hour for equilibrium. After the voltage step, the contact angle continues its steady rise without any noticeable reaction.

[5]The DPhPC solution was prepared as described in Taylor et al. [10] at 2 mg/mL. However, for the data in Figure 4.5, the DIB measurements were taken after the solution was stored for several months in a refrigerator. The initial monolayer formation took much longer than it did when the solution was first made, and these bilayer results may be affected also. However, considering that aged DPhPC solutions have worse kinetics than fresh ones [136], this further proves the point being made.

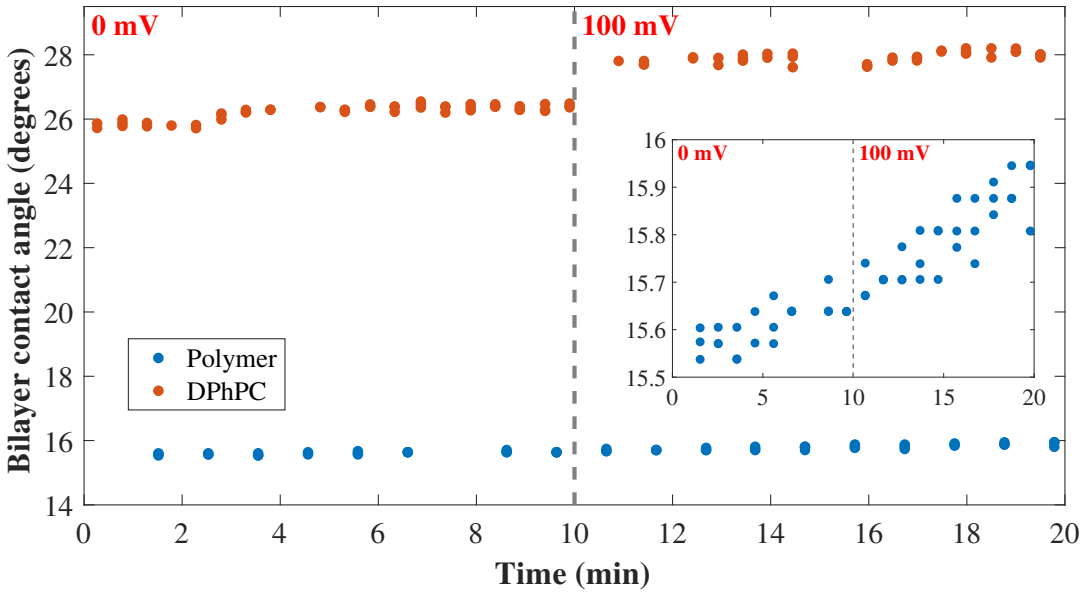

Figure 4.5: Comparison of DIB voltage response of contact angles for aqueous $PMOXA_{13}$-*b*-$PDMS_{47}$-*b*-$PMOXA_{13}$ compared with aqueous DPhPC, each in a bath of hexadecane. For DPhPC, the contact angle responds quickly to the voltage step so that equilibrium is reached within a minute. For polymer, the bilayer was neither in equilibrium before nor after the voltage step so that the Young-Lippmann equation cannot be used. The angles were computed as averages of the two left and two right contact angles shown in Figure 4.16 using the tangent algorithm. Images were taken in groups of three, although some failed to analyze. The inset is a vertical zoom of the polymer data. The polymer data is taken from Figure 4.7 between 80 and 100 minutes. See Footnote 5 for a note on the age of the DPhPC solution.

The slow change in contact angle is concurrent with a slow change in bilayer area. Figure 4.6 shows the initial bilayer formation at the instant of bilayer formation for polymer and DPhPC DIBs. In the 35 seconds plotted, the polymer bilayer grows to a fifth of the size of the DPhPC bilayer. The bilayer area stabilizes within 5 minutes for DPhPC (data not shown) but continues to grow for hours for our polymer. Figure 4.7 shows a bilayer area trace over a much longer period of time. Despite the electrodes being pushed together to accelerate bilayer growth, the area continued to grow after they were returned to their original position. This shows that equilibration would likely take several hours. Voltage steps up to 500 mV were also applied. While these increased the

rate of bilayer formation, they did not quickly achieve equilibrium either.

The slow rate of bilayer formation is the source of the slow change in contact angle. When a voltage is applied, the electric field becomes negligible within tens of nanometers from the contact line[6]. Outside of the region affected by the field, the droplet curvature is fully specified by the monolayer tension and the vertical position along the droplet (via $\Delta\rho g z$) in Equations (2.9) and (2.10). Thus, while the contact angle may be affected on the nanoscale, the macroscopic, measured contact angle is effectively unchanged without a change in bilayer area.

The slow rate of bilayer formation observed here stands in stark contrast to the results reported by Tamadonni et al. [146], who performed experiments on a similar block copolymer dissolved in the oil phase. They observed reversible, rapid growth of the bilayer area in response to steps in voltage, about a thousandfold faster than that observed here. There are two differences that may responsible for their results: the polymer and its presence in the oil phase instead of the aqueous phase. They used PEO_{45}-*b*-$PDMS_{27}$-*b*-PEO_{45} in comparison to our use of $PMOXA_{13}$-*b*-$PDMS_{47}$-*b*-$PMOXA_{13}$.

Considering the difference in the block length of the PDMS group and in view of the hypersensitivity of micellar exchange kinetics on hydrophobic block length, it is reasonable to ask whether some similar hypersensitivity is responsible for the thousandfold difference in bilayer formation kinetics. One process that may affect the zipping of monolayers to form a bilayer is the lateral diffusion coefficient. This sets the timescale of the lateral motion of molecules in the monolayer and bilayer. According to Itel et al. [135], the lateral diffusion of the molecules is determined by the molecular weight of the middle block. Extrapolating from the results in Itel et al., our polymer has a lateral diffusion coefficient of 1.7 $\mu m^2/s$ while Tamadonni's has a lateral diffusion coefficient of 3.4 $\mu m^2/s$.

[6]Even at the bilayer, an applied voltage has a relatively weak effect; for example, at 100 mV, the capacitive energy for a 0.2 $\mu F/cm^2$ bilayer is $CV^2/2 = 1$ nJ/cm^2, or less than 1% of $k_B T$ per molecule.

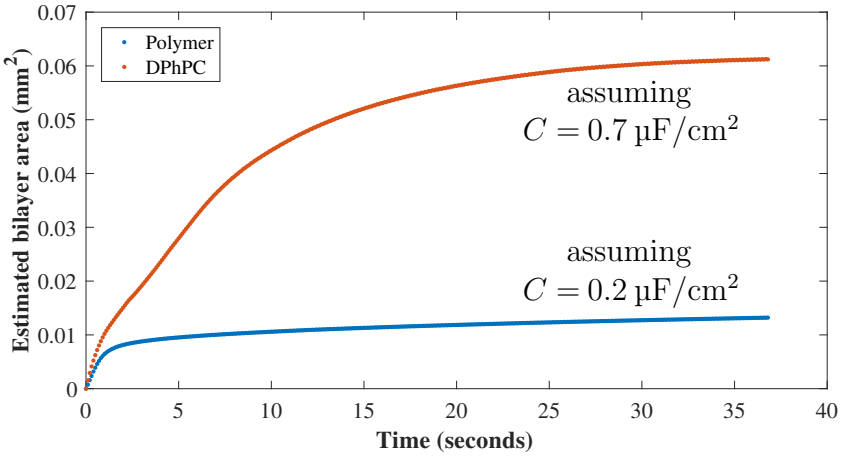

Figure 4.6: Comparison of initial bilayer formation rate for shrunk droplets of aqueous $PMOXA_{13}$-*b*-$PDMS_{47}$-*b*-$PMOXA_{13}$ against droplets of aqueous DPhPC, each in a bath of hexadecane. This demonstrates that the initial bilayer formation rate for the polymer is much slower than for DPhPC. The current response to a 100-mV-amplitude triangle wave was used to determine the capacitance via $I = C\frac{dV}{dt}$. Capacitance was scaled by 0.7 $\mu F/cm^2$ and 0.2 $\mu F/cm^2$ to yield areas for DPhPC and polymer, respectively, which are the values determined at large area. The assumption that the initial specific capacitances are equal to their later values may not be valid, so that this plot should be considered to be an estimate. This method was preferred over determining areas using microscopy due to the inaccuracy of measuring small areas.

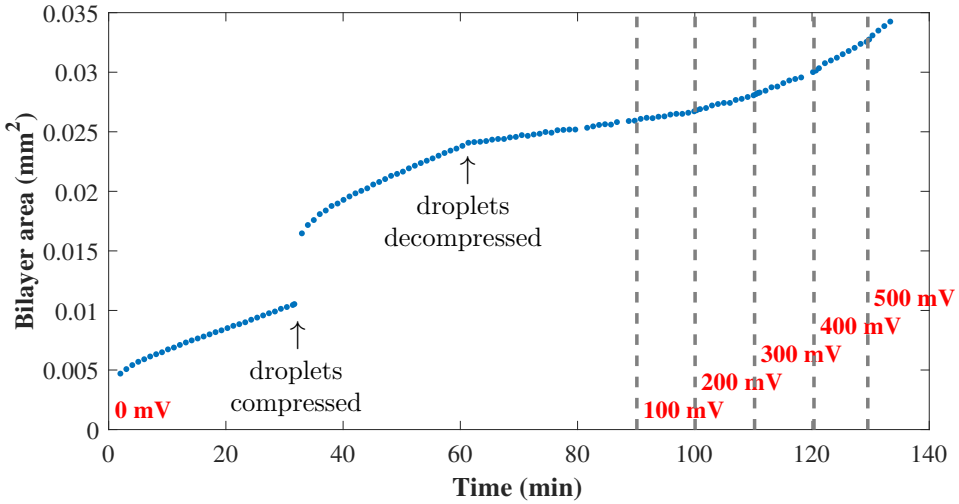

Figure 4.7: Bilayer area plotted against time for shrunk droplets of aqueous $PMOXA_{13}$-*b*-$PDMS_{47}$-*b*-$PMOXA_{13}$ in a bath of hexadecane. The rate of bilayer formation increases with droplet compression and with applied voltage, but equilibration would likely take several hours. The areas were computed automatically using the maximal algorithm explained later in Section 4.4.2 using microscope images.

For comparison, the lateral diffusion coefficient is 12.5 $\mu m^2/s$ for the phospholipid POPC. Considering that the threefold to fourfold reduction from phospholipids to Tamadonni's polymer does not necessitate slowing of the bilayer formation kinetics, it is unlikely that the additional twofold reduction to our polymer is responsible for slow kinetics. Another process that could potentially affect the dynamics of bilayer area changes is the exclusion of solvent between opposing PDMS molecules and within each PDMS group. Part of this is due to the viscosity of the solvent. However, the fast bilayer formation kinetics were demonstrated for an oil mixture with a viscosity larger than that used here[7].

One mechanism by which the bilayer area can change is by zipping and unzipping, whereby the opposing monolayers join or separate. Considering the middle block is PDMS in both Tamadonni's and our case, it is unclear why the kinetics of zipping and unzipping would be so different. One possibility is that the presence of polymer in the oil acts as a catalyst for zipping and unzipping.

An alternative mechanism to zipping and unzipping for bilayer area changes is the adsorption and desorption of polymer to and from the monolayer and bilayer. The bilayer could grow in size if polymer is simultaneously desorbed from the monolayer and adsorbed to the bilayer. This is similar to the exchange mechanisms that are responsible for the equilibration of aggregates that was mentioned earlier in this chapter. For amphiphiles in the oil phase, the adsorption and desorption of polymer onto the bilayer could occur along the monolayer-bilayer contact line[8]. The polymer used by Tamaddoni exhibited faster monolayer formation than lipids, forming packed monolayers within only 30 seconds of droplet deposition, compared to 2 to 5 minutes for lipids in water [146]. On the other hand, such a mechanism of bilayer growth would be nonexistent in the case of

[7]A video in their supplementary material features a mixture of 1:3 silicone oil AR 20:hexadecane. Considering silicone oil AR 20 has a viscosity of 20 mPa · s, its viscosity must be larger than that of pure hexadecane used in our case.

[8]There is also a possibility that the polymer would saturate the aqueous phase if its solubility is high enough, so that adsorption and desorption occur at the bilayer-water interface.

aqueous $PMOXA_{13}$-*b*-$PDMS_{47}$-*b*-$PMOXA_{13}$ due to the slow exchange dynamics, so that the bilayer must grow by a zipping mechanism. This vast difference in adsorption and desorption kinetics could result from differences in our polymers as well as their inclusion in the oil phase compared to the aqueous phase.

Bilayer specific capacitance

Specific capacitance measurements were made for $PMOXA_{13}$-*b*-$PDMS_{47}$-*b*-$PMOXA_{13}$ DIBs as a first estimate of the bilayer thickness using the DIB approach. It is well known that lipid membranes surrounded by an annulus of oil have a thickness that depends on the nature of the oil. For example, this was demonstrated in 1977 by White [7] for glycerol monooleate bilayers in alkanes in aperture-suspended membranes, as well as in 2011 by Gross et al. [8] for DPhPC DIBs in alkanes. In both cases, when the alkane was varied from decane to heptadecane (linear hydrocarbons from 10 to 17 carbons in length), the thickness of the hydrophobic layer decreased from 4.4-4.8 nm to 2.8-3.0 nm. We observed a similar trend for aqueous $PMOXA_{13}$-*b*-$PDMS_{47}$-*b*-$PMOXA_{13}$ DIBs: typically larger oil molecules resulted in thinner bilayers.

To demonstrate this effect, the specific capacitance of polymer DIBs was determined in mixtures of D4 in squalene. D4 (octamethylcyclotetrasiloxane) is a small molecule siloxane (and a precursor to the PDMS block during synthesis) with some amount of mixing with the PDMS block of the polymer. On the other hand, squalene is a large hydrocarbon composed mostly of alkyl groups which is excluded from the PDMS block. Specific capacitance was determined using simultaneous capacitance measurements with DIB images as shown in Figure 4.16. The result is plotted in Figure 4.8, which shows the dependence of specific capacitance on oil composition. Here only one experiment was

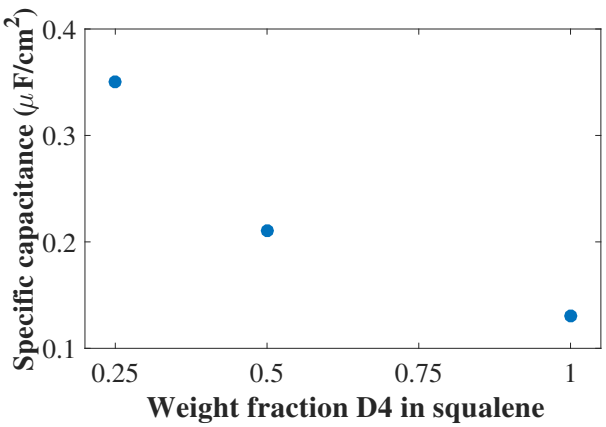

Figure 4.8: A plot of the specific capacitance against oil composition for mixtures of D4 and squalene. With increasing concentration of squalene, the specific capacitance rises significantly, demonstrating that more solvent is excluded from the membrane interior. For each measurement N=1 and measurements were made using a microscope camera only. Therefore, this plot should be viewed as an estimate.

performed for each oil and measurements were made using a microscope camera only[9], so the values should be viewed as estimates.

The thickness of the hydrophobic region h can be estimated using the specific capacitance and the dielectric constant ϵ of the hydrophobic region of the membrane using the formula for a parallel plate capacitor: $C_{\text{specific}} = \epsilon/h$. There are three possible components in the hydrophobic region (PDMS, D4, and squalene) and their proportions determine ϵ. Because squalene is less likely to remain in the bilayer, its contribution to ϵ is neglected. Thus we assume that the membrane is permeated by D4 only, which has a bulk dielectric constant of $2.39\epsilon_0$ [147]. The dielectric constant for the PDMS is assumed to be the same as for bulk PDMS: $2.8\epsilon_0$ [148]. As an estimate, we assume that the dielectric constant can be extrapolated linearly based on the volume fraction of D4 to PDMS in the membrane.

For a weight fraction of 0.25 D4 in squalene, we assume the hydrophobic region is

[9]Because the droplets are distorted by gravity, the bilayer area is an ellipse rather than a circle. These measurements neglect this effect by measuring the diameter of the ellipse from the bottom and assuming the interface area to be a circle.

almost completely comprised of PDMS so $\epsilon = 2.8\epsilon_0$ is used. Then the measured specific capacitance of 0.35 µF/cm^2 gives $h = 7$ nm. A membrane in pure D4 is ~70% D4 by volume according to its capacitance of 0.13 µF/cm^2, so $\epsilon = 2.5\epsilon_0$ is used. Similarly for a membrane in 50 wt.% D4, the membrane is ~50% D4 by volume based on its measured capacitance of 0.21 µF/cm^2, so $\epsilon = 2.6\epsilon_0$ is used. Using these estimates gives thicknesses of 11 nm and 17 nm for weight fractions of 0.5 and 1 D4 in squalene. Similar trends were observed in all oils studied. For example, the addition of squalene to silicone oil AR 20 or to hexadecane similarly increased their specific capacitance to ~0.35 µF/cm^2. Additionally, DIBs in decane had a specific capacitance of ~0.1 µF/cm^2, compared to ~0.2 µF/cm^2 for hexadecane.

These preliminary results demonstrate that the hydrophobic thickness of PMOXA$_{13}$-*b*-PDMS$_{47}$-*b*-PMOXA$_{13}$ bilayers may be as small as 7 nm and as large as 20 nm. These results show a larger range in thickness than observed by Gross et al. [8]. This is expected because while the lipid chains in DPhPC are relatively stiff, the PDMS groups are flexible, allowing them to have a larger range of thicknesses as they are permeated with oil. The values here are consistent with capacitance measurements of an aperture-suspended membrane using PDMS-PMOXA-PDMS with a 5,400 g/mol PDMS group by Nardin et al. [128]. Their hydrophobic thickness was deduced from $C_{\text{specific}} = \epsilon/h$ to be approximately 10 nm, although the level of solvent in their membranes (formed using chloroform and toluene) is not known. The relation between the molecular weight m of the hydrophobic and its thickness h for PDMS is about $h \propto m^{0.6}$ [123] in our case, so that extrapolating to our 3,500 g/mol PDMS block gives 7.7 nm. Additionally, electroformed vesicles of PDMS-PMOXA-PDMS with a 3,700 g/mol PDMS were deduced to have a hydrophobic thickness of 8.8 ±0.7 nm from TEM images [123], again in agreement with the estimates for our polymer.

Figure 4.9: A demonstration that droplet profile is not significantly altered by contact in a DIB. Even when the electrodes are moved far apart, the droplet profile looks about the same far from the electrodes and contact point.

4.3 Application of the Young-Laplace equation to DIBs

As described in the previous section, the Young-Lippmann equation cannot be used to find the monolayer and bilayer tension for aqueous $PMOXA_{13}$-*b*-$PDMS_{47}$-*b*-$PMOXA_{13}$ DIBs. We sought an alternative method that could determine monolayer and bilayer tension by analyzing droplet shape. As described in the theory section, a typical pendant drop tension measurement is fit using the Young-Laplace equation under the assumption of axial symmetry. This yields a simple differential equation that can be solved by numerical integration. In the case of two droplets that are adhered to each other, axial symmetry is necessarily broken, so that a simple solution is unattainable. One possible approach to determine the tension would be to use finite element analysis in three dimensions to fit the DIB profile. We avoided this approach in favor of an approach that is less cumbersome and computationally less expensive.

The shape of droplets in contact closely resembles their shape before contact, as shown in Figure 4.9. It seems plausible that the droplet profile far from the contact interface could be fit assuming axial symmetric to estimate interfacial tension. In this section we use finite element simulations to estimate the error associated with this approach. When optimized, the approach is accurate to within 5-10% over a variety of system parameters.

4.3.1 Symmetrization and droplet fitting algorithm

We begin by establishing a method for fitting parts of a DIB profile under the assumption of axial symmetry. Rather than write a new algorithm to fit portions of the DIB images, the images are digitally modified to appear as two separate, axisymmetric pendant drops. Then each symmetrized image is fed into open-source pendant drop software (Pendant Drop, developed by Daerr and Mogne [111] for ImageJ) to fit the droplet profiles. The digital symmetrization procedure was automated in a Matlab script.

The symmetrization algorithm begins by scaling the image intensity so that 1% of the pixels are saturated at white and black for consistency across different lighting conditions. The edges are then detected using a black/white threshold and a Canny edge detector, as described later for the angle-measurement algorithm. The image is split into a left and right half near the droplet interface. Then the outer side (the side not in contact) of each droplet is flipped over a vertical line going through the droplet bottom, so that each droplet appears as an individual, complete droplet with mirror symmetry.

In order to reduce errors associated with finding the droplet bottom, the Matlab script first detects the bottom edge of each droplet, and then compares it with its mirror image about all points near the droplet bottom. The origin of reflection yielding a mirror image most similar to the original is selected as the origin of the flip transformation. The similarity between the original and its mirror image is parametrized by the sum of vertical pixel distances between their edges. The result of this procedure is demonstrated in Figure 4.10 using an image from a real experiment.

4.3.2 Pendant drop fitting of simulations

Droplet profiles were simulated using Surface Evolver, a program for finding the minimal energy of surfaces subject to physical constraints. A continuous surface is ap-

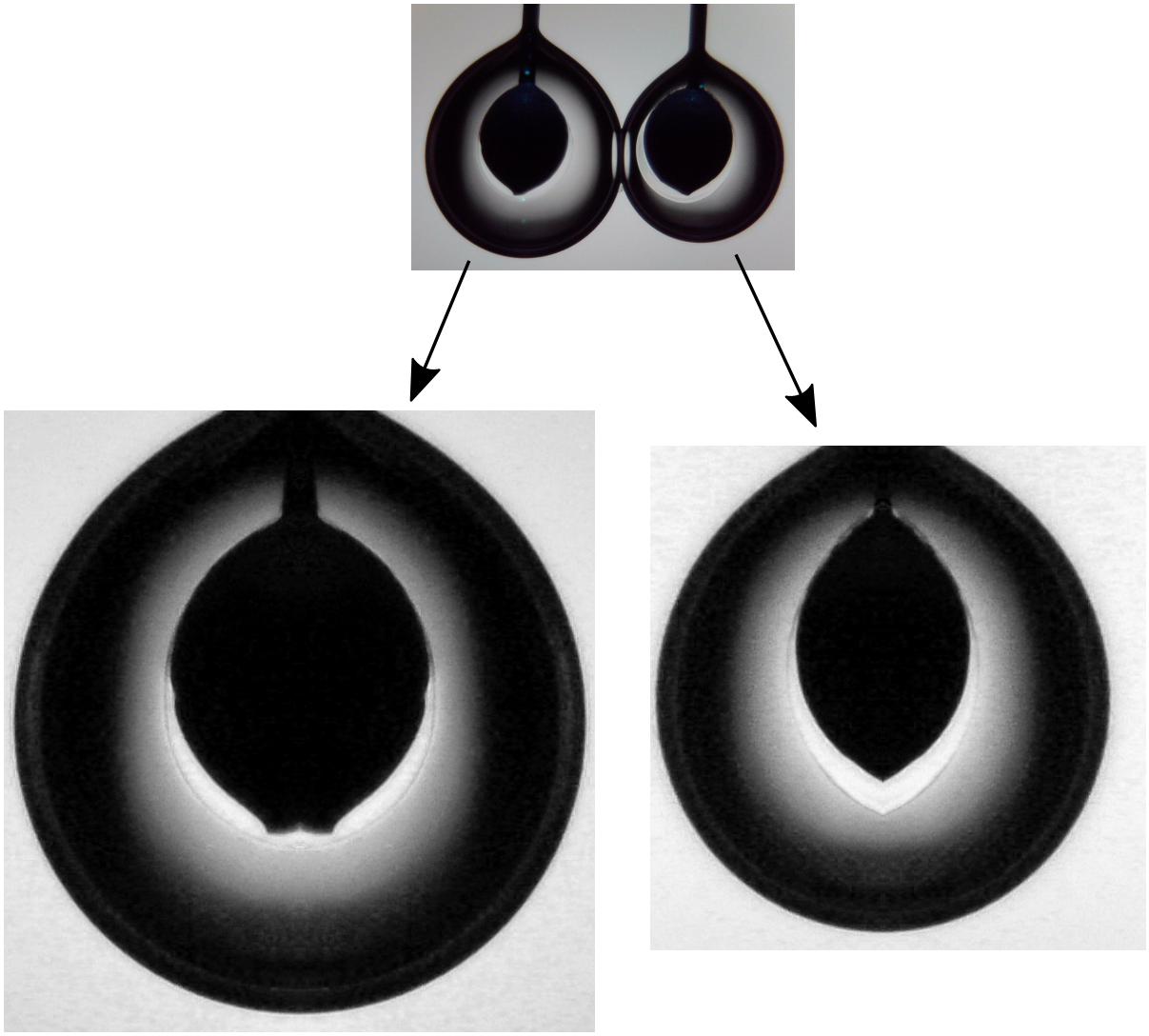

Figure 4.10: The results of the symmetrization algorithm (bottom images) applied to a DIB (top image). The symmetrized images are ready for analysis with pendant drop fitting software. During DIB experiments, the electrode separation was set so that the droplets appeared to hang vertically. This was visualized by imagining a vertical line running from the bottommost part of each droplet to the center of the contact point with its electrode.

proximated by vertices on a mesh and is iterated to minimize total energy. A standard iteration of the surface uses gradient descent, where the partial derivative of the total system energy with respect to the position of each vertex is used to take a step in the direction toward lower energy. Additionally, the matrix of second derivatives (the Hessian) of total energy with respect to vertex positions may be used along with the gradient to provide improved convergence.

The script used here was adapted from a Surface Evolver script provided generously by Stephen A. Sarles, the principal investigator in Taylor et al. [10]. The script was designed to estimate the ellipticity of the bilayer area for different values of interfacial tension using the gradient descent method. In our case, it was necessary to use Hessian iterations to produce single droplet profiles that could be fit accurately by Pendant Drop. Without the use of Hessian iterations, the fits to single pendant drops gave tension values that differed by ~30-70% from the programmed values. Additionally, the RMS distance between the fit line and the detected droplet edge was generally 3-8 pixels, signifying an unrealistic droplet shape. With the use of Hessian iterations, fits to single pendant drops had ~5% error in retrieving the programmed tension and an RMS fit distance generally less than 1 pixel at the same image resolution.

The Hessian iteration uses the Hessian matrix to take a much larger step toward the minimum energy than gradient descent; but if the surface is not already near equilibrium, the Hessian iteration will cause wildly unrealistic deformations. While Hessian iterations typically worked for single pendant droplets, they always failed for DIBs regardless of the mesh resolution. The source of the issue is at the bilayer interface and at the contact points with the wires. To solve the issue, vertices in those regions were frozen in place prior to Hessian iterations. They were then unfrozen and gradient descent iterations were performed. Though the regions that were temporarily frozen may have an unrealistic shape, they are effective in breaking the axial symmetry of the pendant drops.

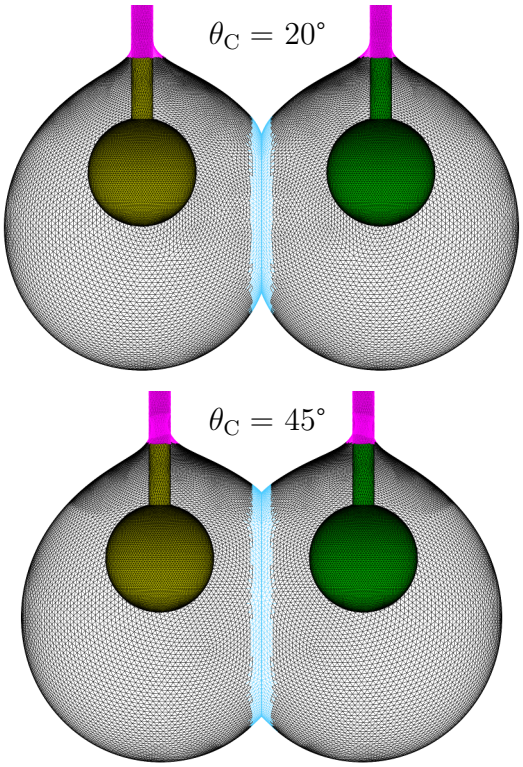

Figure 4.11: Simulations of droplet shape using Surface Evolver. In both cases, the monolayer tensions are 2 mN/m and the droplet volumes are 150 nL. The blue and magenta are regions of the droplets that were frozen in place partway through the simulation to avoid instabilities. The shape of the remainder of the droplets is accurate if the colored regions are regarded as fixed boundaries. After the simulation, the droplets and electrodes were colored black to produce high resolution droplet profiles, as shown in Figure 4.12. For scale, the balls of the electrodes are 250 µm in diameter.

Additionally, the remainder of the droplet shape should be accurate if the frozen regions are considered as fixed boundaries. Figure 4.11 shows the results of Surface Evolver simulations using this strategy.

The simulated meshes in Figure 4.11 were colored black and exported as high resolution images which were symmetrized and analyzed with Pendant Drop as though they were DIB images. Simulations were performed for three different droplet configurations: $\gamma_m = 2$ mN/m with $\theta_C = 20°$, $\gamma_m = 2$ mN/m with $\theta_C = 45°$, and $\gamma_m = 4$ mN/m with $\theta_C = 20°$. In all cases, the droplet volumes were fixed to 150 nL each, including the

volume of the enclosed electrode. The electrodes included a 50-µm-diameter wire (to match the diameter of the Ag wire) and a 250-µm-diameter ball. Physical parameters were chosen to match those in experiments: $\rho_{\text{aqueous}} = 1.04$ g/mL for the aqueous phase, $\rho_{\text{hexadecane}} = 0.77$ g/mL for hexadecane, and $g = 9.8$ m/s^2.

Two parameters are expected to have an effect on the success of the method: the height of the profile up to which the image is fit and the electrode separation. The electrode separation is expected to cause deviations from axial symmetry, as demonstrated in Figure 4.9. Because this deviation is largest at the contact point with the electrode, decreasing the height of the profile up to which the image is fit is likely to provide more accurate fits. The height to which the droplet profiles are fit is parametrized as the crop width: the image is cropped at the first vertical position at which the droplet width equals the crop width[10]. Figure 4.12 demonstrates the effects of both of these parameters. For crop widths greater than 200 µm, the programmed monolayer tension was recovered to within 10% accuracy over a 100-µm range of electrode separations. Control over electrode separation on this scale is easily achieved using micropositioners.

Figure 4.13 demonstrates the accuracy of all three droplet configurations using a crop width of 400 µm over an expanded 200 µm range of electrode separations for each case. Pendant drop fits using the symmetrization algorithm are successful in retrieving the programmed values of interfacial tension to within 6% in all cases. That the errors are low and vary little over a large range of electrode separations implies that the method is suitable for real experiments.

In real experiments, there is a trade off with respect to crop width. Larger crop widths reduce the amount of information for pendant drop fits. In fact, the droplets tops contain the largest deviation from sphericity, so that the region that is cropped off is the richest in information about the monolayer tension. This effect was mitigated in the case

[10]The automated algorithm for performing cropping at the crop width is explained in Section 4.4.1.

Simulated droplet profiles for different electrode separations:

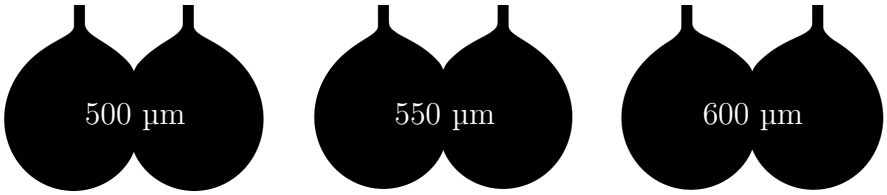

Symmetrized images for 550-µm electrode separation with different crop widths:

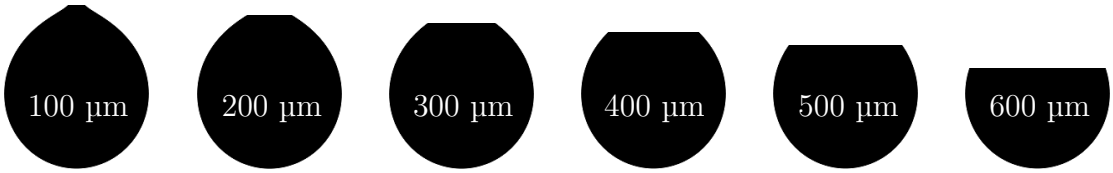

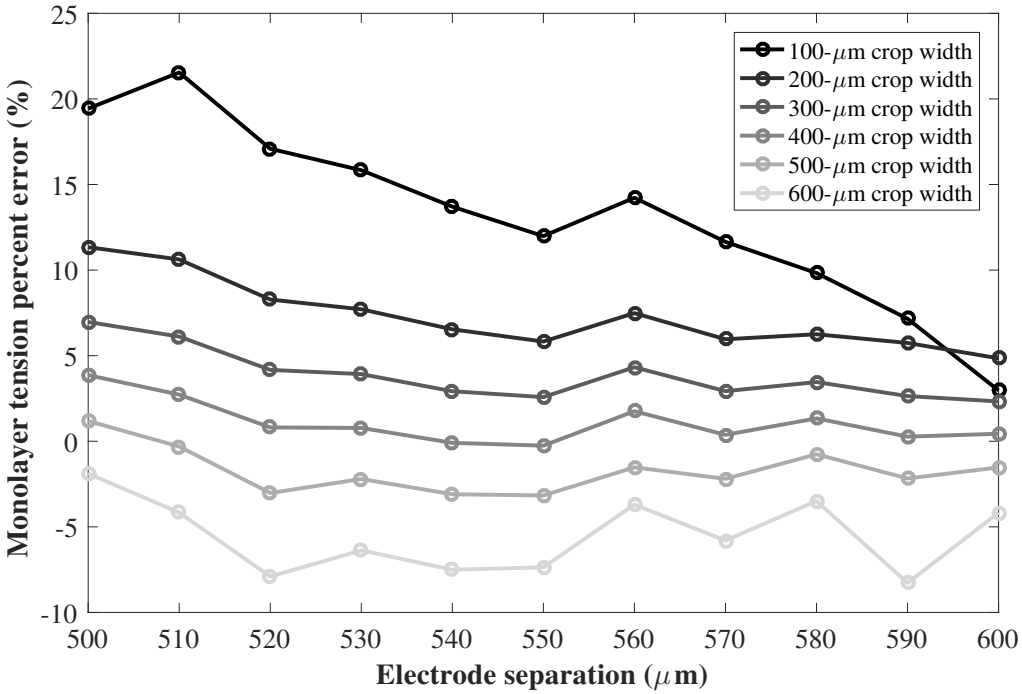

Figure 4.12: Percent error for monolayer tensions fit after using the symmetrization algorithm for simulated DIBs plotted against electrode separation for different crop widths. This plot shows that there is an ideal crop width for which the error is less than ~5%. All simulations used a monolayer tension of 2.0 mN/m and a bilayer contact angle of 20° for 150-nL droplets. After symmetrizing and cropping the left droplets, their tension was fit using Pendant Drop in ImageJ. Percent errors were computed by comparing the fitted tensions against the programmed tension of 2.0 mN/m.

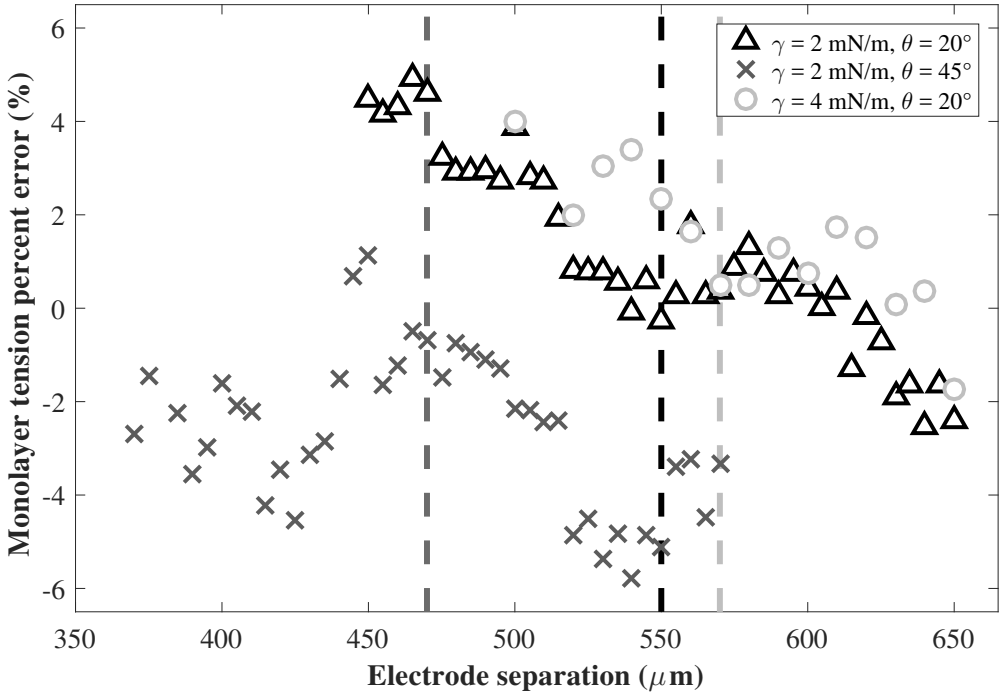

Figure 4.13: Percent error for monolayer tensions fit after using the symmetrization algorithm for simulated droplet profiles for three different scenarios: droplets with monolayer tension $\gamma_m = 2$ mN/m and bilayer contact angle $\theta_C = 20°$, droplets with $\gamma_m = 2$ mN/m and $\theta_C = 45°$, and droplets with $\gamma_m = 4$ mN/m and $\theta_C = 20°$. This plot demonstrates that the symmetrization method produces low errors in tension for different conditions over a large range of electrode separations when a favorable crop width is used. Here the crop width was 400 µm and the droplet volumes were 150 nL in all cases. The vertical dashed lines mark the electrode separation at which the bottommost part of the each droplet in the original image aligns with the center of its contact with the electrode.

of these simulations due to the high resolution (~3 pixels/µm) of the images used. In a real setting, this leads to larger random errors, so that an ideal crop width may be 200 or 300 µm, as we will demonstrate in Section 4.4.3. Finally, we note that, because the error in fitting single pendant drops simulated using Surface Evolver is approximately ~5%, the accuracy for a real experiment is potentially better or worse than demonstrated here.

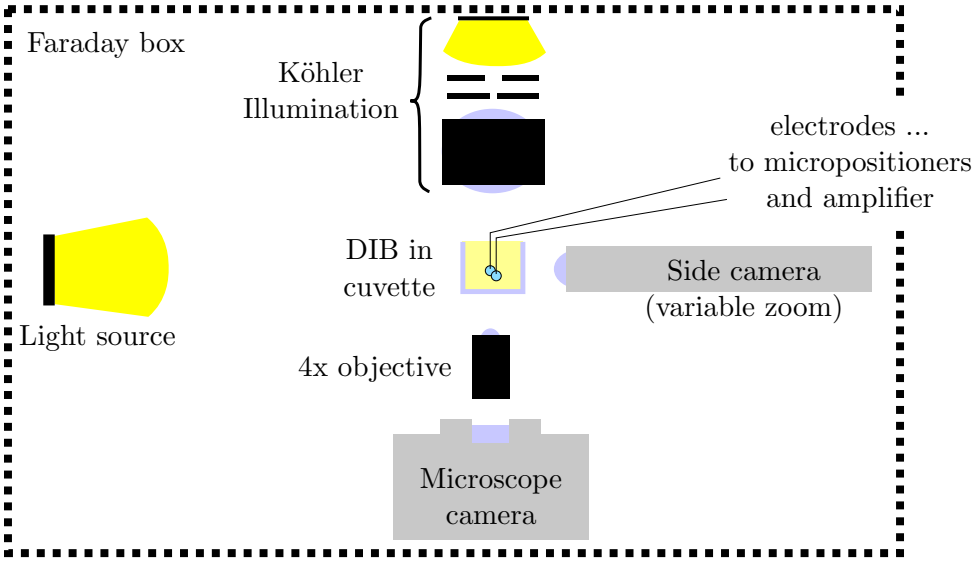

Figure 4.14: Experimental schematic for two-camera measurements. A photograph of the setup is shown in Figure 4.15.

4.4 Experimental and programming details for two-camera measurements

A schematic and photograph of the experimental setup during measurements are shown in Figures 4.14 and 4.15. All experiments were performed on a vibration isolation table in a grounded Faraday box large enough to enclose the microscope. An all-glass, all-sides-polished fluorometer cuvette (Varsal, 450-33-G20) was used to hold the oil bath, which allowed for distortion-free imaging of the droplets from both the bottom and side. The top of the cuvette was sawed off at a height of 8 mm for electrode access to the focal point of the objective.

A CMOS microscope camera was used (AmScope MU1803, 18 MP, USB 3.0) with the 4x objective of an inverted microscope (Tritech Research). The CMOS camera was chosen for its low cost and high resolution. The high resolution was somewhat beneficial to the profile fitting algorithms on Matlab, even though the resolution is limited by the numerical aperture of the microscope. However, a drawback of the CMOS camera was

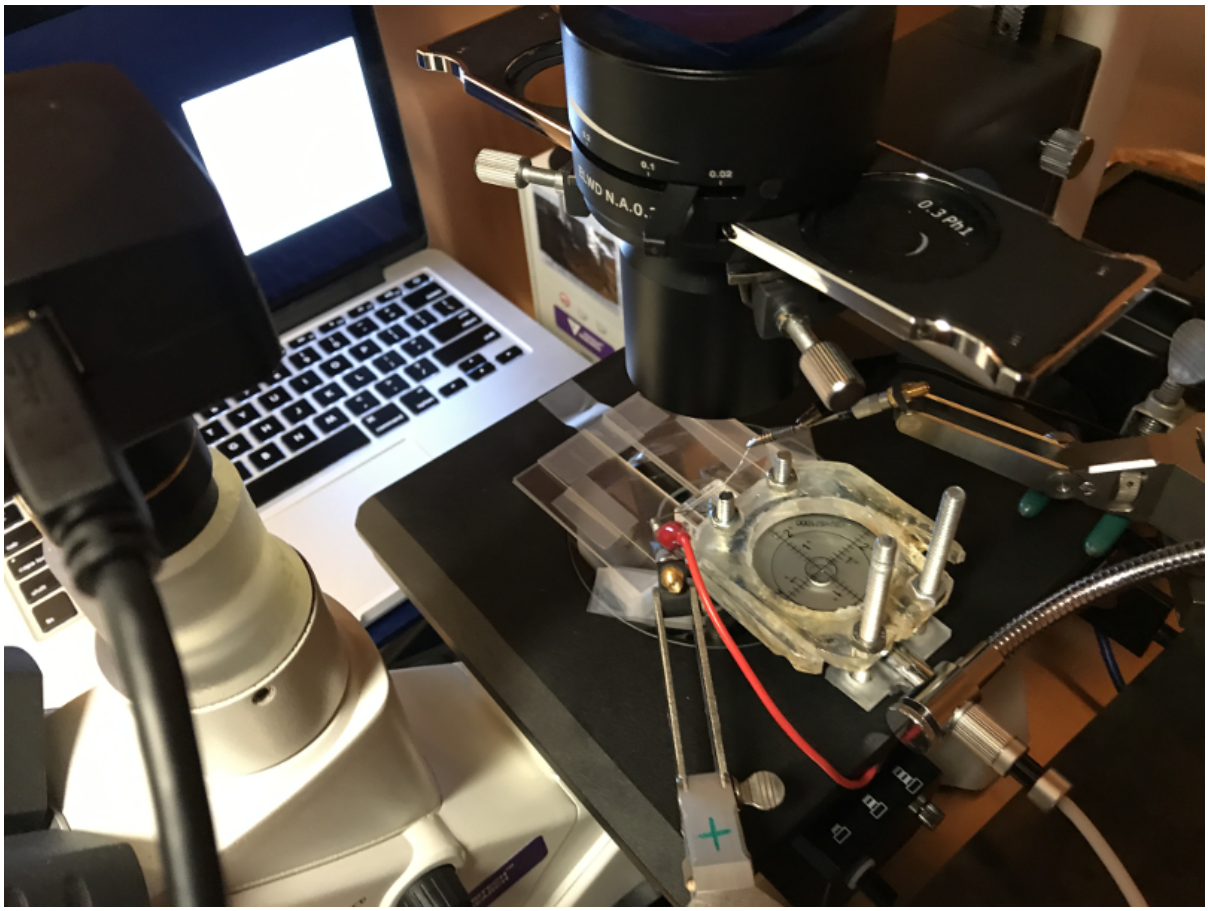

Figure 4.15: Photograph of the two-camera experimental setup for DIBs. The microscope camera is visible in the left foreground, while the side camera (a boroscope) is visible on the bottom right, held by a flexible arm and covered by a bubble level to which it is fastened by four nuts and bolts. A white square on the screen of a laptop is used as a source of uniform light for the side camera. The fluorometer cuvette is immediately in front of the side camera, and two electrode wires are held over it by micropositioners. Red and black alligator clips connect these wires to the headstage of the Axopatch, which is clamped just beneath the microscope stage. The entire setup is enclosed by a Faraday box with Cu-colored metal sheet that is visible in the background.

that the rolling shutter of the CMOS camera produced a wobble effect in combination with vibrations that could not be damped. This is the most likely source of the random error in contact angle and area measurements in Section 4.4.3.

The side camera (Opti-Tekscope OT-FlexScope, 2 MP) was also CMOS-based and allowed for continuous zoom by twisting a knob at its end. In order to ensure upright images, a two-axis bubble level was mounted to the cylindrical shaft of the camera after calibrating it with a plumb bob. The mounting was performed by 3D printing pieces that could be screwed together to fit snugly across the bubble level and camera shaft. Prior to beginning measurements, the camera head was adjusted to within 1 cm of the cuvette and leveled to less than 1° by adjusting the flexible holding arm of the camera. To limit cost, a laptop screen was used as a source of uniform light for the side camera. A 10-hour video of an approximately 10-mm square of white pixels on a black background was used so that the intensity remained constant. It was kept approximately 35 mm from the camera, with the center of the square aligned with the center of the field of view. The lighting conditions and camera created a blur along the droplet edge not seen on commercial pendant drop setups. This likely caused errors that may be improved with a more advanced setup.

50-µm silver wire (Alfa Aesar™ 44461G5, 99.99%, annealed) was used for the electrodes. One end of a ~1-cm length of wire was quickly moved in front of a propane flame to melt and ball up the end. The other end was soldered to a thicker piece of wire, which fit snugly into the arm of a micropositioner. The silver ball and wire was chlorided by submerging it in a bath of measurement buffer and applying a 100 mV voltage for 30-60 seconds using a much larger sintered Ag/AgCl pellet (In Vivo Metric) as a counter electrode. Low gelling temperature agarose (Sigma-Aldrich A9414) was mixed at 3% w/v with measurement buffer and heated to above 70°C and thoroughly mixed by vortexing. The Ag/AgCl electrode was carefully scraped along the meniscus of the melted agarose

solution, ensuring that the agarose coated the ball but not the wire. The same agarose preparation was reheated for reuse as needed. After being submerged in the bath of n-hexadecane (99%, Alfa Aesar), the agarose was rehydrated by suspending a 1-µL or 2-µL droplet of buffer solution for 5 minutes. The droplet was withdrawn with a pipette and vesicle solution was deposited using the shrinking approach described in Section 4.2.1. Before performing additional experiments, the polymer solution was removed from the electrodes and they were soaked again in buffer solution for 5 minutes.

For the aqueous polymer solution, the ethanol injection technique was used. First $PMOXA_{13}$-*b*-$PDMS_{47}$-*b*-$PMOXA_{13}$ was synthesized as in Isaacman et al. [115]. The buffer solution was made using Millipore water with 1M KCl and 10 mM HEPES, set to pH 8 by titration with KOH. 30 mg of the polymer was added to 174 mg of ethanol (Gold Shield) and allowed to dissolve, forming a turbid solution. 2 mL of buffer solution was held partially submerged in a sonicating bath while the polymer-ethanol solution was added over 30-60 seconds. After allowing evaporation overnight (100 mg evaporated), the solution was filtered once at 0.45 µm then four times at 0.2 µm using PTFE syringe filters. This solution was dialyzed 1:100 with the same buffer solution under constant stirring for 5 hours using a Pur-A-Lyzer dialysis kit (Sigma-Aldrich, PURN60010, 6-8 kDa MWCO). The density of this aqueous $PMOXA_{13}$-*b*-$PDMS_{47}$-*b*-$PMOXA_{13}$ solution was assumed to be 1.04 g/mL based on the value for 1M KCl solution. All experiments were performed at 21-24°C.

Capacitance and conductance measurements were taken by connecting the electrodes to the headstage of an Axopatch 200B. For an applied voltage $V_{\text{app}} = 0$, resistance was measured by applying ±10 mV for 100 ms each and using $R = \Delta V/\Delta I$. At higher voltages, $R = V_{\text{app}}/I$ was used, which was measured for 500 ms. Capacitance measurements were performed by applying a 50-Hz, 20-mV peak-to-peak sinusoid centered about the measurement voltage. The phase offset and amplitude of the response current

sinusoid were fit using a Matlab script to determine the impedance. The impedance Z of the sinusoid was used to deduce the capacitance assuming a simple series RC circuit, so that $C = \frac{1}{2\pi f}\frac{\mathrm{Im}\{Z\}}{\mathrm{Im}\{Z\}^2 + \mathrm{Re}\{Z\}^2}$. Additionally, a 20 mV peak-to-peak triangle wave was applied about V_{app} with $\frac{dV}{dt} = \pm 0.4$ V/s to determine the capacitance via $I = C\frac{dV}{dt} - \langle I \rangle_{V_{\mathrm{app}}}$, where $\langle I \rangle_{V_{\mathrm{app}}}$ is the mean current at V_{app}. The two capacitance methods generally agreed to around 1%, and the impedance-based approach was always used because it was assumed to have greater accuracy. All of these measurements were performed in a single 1.5-s sweep. The data was filtered using the Axopatch's built-in 8-pole, 1-kHz filter and was oversampled using a Digidata 1550 at 50 kHz to provide a higher resolution for fitting the phase of the sinusoid.

The two images and capacitance measurement used three separate programs, each provided by the manufacturers of the equipment (ToupView for the microscope camera, ehe for the side camera, and Clampex for the capacitance measurement). Their simultaneous acquisition was achieved by using AutoHotKey for Windows, a program that automates keystrokes and mouse clicks using a timer. Using this technique, all files acquired simultaneously were timestamped within 5 seconds of each other, a timescale over which significant changes were rare.

4.4.1 Experimental considerations for pendant drop measurements

The solution to the pendant drop equation, Equation (2.10), is fully specified by the density difference between the two fluids, and two unknowns such as the droplet width and the radius of curvature at the droplet bottom. However, in practice, pendant software fit for the direction of gravity also because the camera is not usually upright [111]. Fitting for the direction of gravity in an image is straightforward in the case of a single axially

symmetric droplet due to its mirror symmetry about the direction of gravity. However, it becomes nontrivial in the case of two droplets, which may have different volumes so that they are not mirror symmetric. This issue was addressed experimentally by calibrating the camera angle with a plumb bob as described in the experimental section.

The side angle of the camera features a variable zoom lens without gradations, making pixel scale calibration difficult. The variable zoom is a beneficial feature because it allows the user to fill the camera's field of view regardless of droplet size to attain a high resolution image. On the other hand, the microscope camera uses a fixed 4x objective with a pixel scale calibrated using a sample of known dimensions. This enables the use of the microscope camera to calibrate the length scale of the side camera. This was accomplished by identifying the horizontal extent of the droplets in the side camera with the same horizontal extent as measured with the microscope for every pair of images. A Matlab script was written to perform this process automatically using a Canny edge detector to determine the horizontal extent of the droplets in both images.

4.4.2 Details of contact angle and bilayer area determination

A Matlab script was coded to determine the two bilayer diameters and eight contact angles visible in the simultaneously captured images. The script was recreated based on the results reported by Taylor et al. [10]. As in the symmetrization algorithm, the script starts by scaling the image intensity so that 1% of the pixels are saturated at white and black for consistency under different lighting conditions. The image is then converted to black and white by establishing an intensity threshold below (above) which all pixels are changed to black (white). This prevents the edge detection algorithm from detecting edges other than the droplet profile. Wherever coordinates of the top and bottom edges of the droplet profile are desired, a Canny edge detection function is used. Then top and

bottom edges are converted to a function of horizontal position by counting the number of pixels until the first edge from the top or bottom of the image.

The images are rotated to upright under the assumption that the droplets should each be mirror-symmetric about an axis normal to the center of the bilayer plane[11]. This accounts for the possibility that the contact point on either side is occluded by the adjacent droplet edges, so that the true contact point is not identified. It also ensures that the contact angle on either side of the interface is measured relative to the plane of the bilayer. The applied rotation angle is found by guessing and checking applied rotations until the remaining deviation from mirror symmetry is below a threshold. Applied rotations are always applied to the original droplet image, prior to the black/white thresholding and edge detection, to prevent undesirable artifacts of the processes from compounding.

Two Matlab scripts are used to determine angles and interfacial lengths that we will call the maximal algorithm and the tangent algorithm. They are illustrated in Figures 4.16 and 4.17, which demonstrate the results of both algorithms for both the side and bottom view. In the maximal algorithm, the length of the contact interface is determined by counting the total number of pixels between lowest point of the top edge and the highest point of the bottom edge. To find the contact angles, first the edge is traced left or right from each contact point, calculating the angle to every point on the edge. This function of angle vs horizontal distance exhibits a minimum value, and this minimum is chosen as the correct contact angle. This approach is used because the contact point appears rounded in the 2-3 μm region surrounding it so that the contact angle is close to 90° when only this region is considered. Additionally, the entire region within 5 μm of the contact point is excluded as a candidate for the contact point due to undesirable optical distortions that occur in that region. The net result is that the

[11]This is based on the assumption that the contact angle of each droplet relative to the bilayer plane, θ_{L} and θ_{R}, is constant if the monolayer and bilayer tensions are fixed, as described in Equation (2.2).

maximal algorithm overestimates both the contact angle and the bilayer diameter.

In the tangent algorithm, first, differential contact angles are determined as a function of horizontal position by comparing each point on the edge to the point adjacent to it. Then all contact angles are smoothed over a 10 µm region, and the point with the smallest contact angle chosen as the correct angle. Again, the entire region within 5 µm of the contact point is excluded from consideration. The tangent lines are extrapolated from the points at which the contact angles are chosen until they intersect. The intersection points serve as the top and bottom contact points, so that the distance in pixels between them is used to determine the bilayer diameter.

The bilayer diameters of the side camera and microscope camera are assumed to be the major and minor diameters of an ellipse which represents the bilayer area. The bilayer area is combined with the simultaneously acquired conductance and capacitance measurements to provide the specific conductance and specific capacitance. The four left and four right contact angles are averaged to provide θ_{L} and θ_{R}. These are combined with the monolayer tensions γ_{L} and γ_{R} deduced by fitting the symmetrized droplets to provide the bilayer tension via Equation (2.2).

Bilayer bowing due to asymmetric DIBs

A bilayer will bow as a result of asymmetric droplets. To investigate whether this effect may be neglected in a DIB, an estimation of bilayer bowing is made for the case of zero gravity, as illustrated in Figure 4.18. The assumption of zero gravity allows for an order of magnitude approximation without complicated math. The Laplace pressure is $P_1 = \gamma_1/R_1$ in the left droplet and $P_2 = \gamma_2/R_2$ in the right droplet, so that the radius of curvature of the bilayer is given by $P_1 - P_2 = \gamma_{\mathrm{b}}/R_3$.

Using values similar to those in experiment ($\gamma_1 = 2$ mN/m, $\gamma_2 = 4$ mN/m, $R_1 = 250$ µm, $R_2 = 350$ µm, $\gamma_{\mathrm{b}} = 5$ mN/m, $A_{\mathrm{bilayer}} = \pi \times (40\mu\mathrm{m})^2$), and comparing A_{bilayer} to

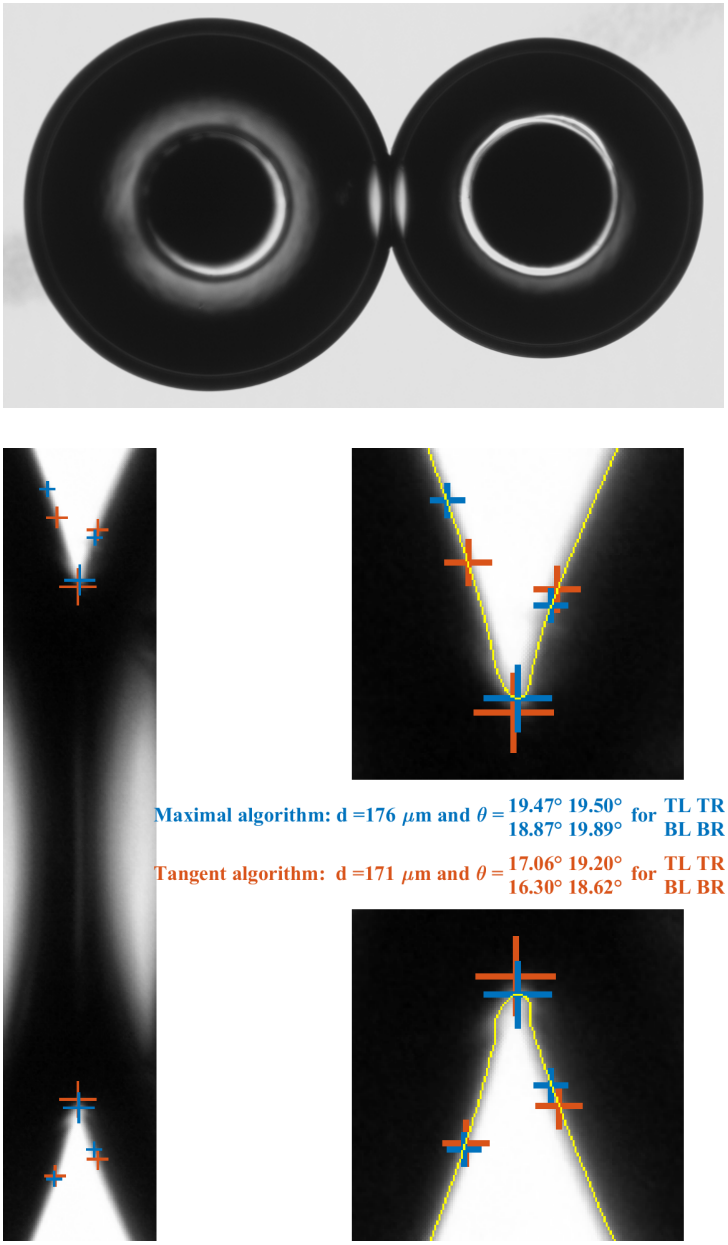

Figure 4.16: Bottom view image of an experimental DIB (top) and a demonstration of the fitting process using Matlab (bottom) as described in the text. The blue (red) crosses and text correspond to the maximal (tangent) algorithm. The results of the edge detection process is overlaid onto the image in yellow for demonstration purposes. The larger crosses denote the deduced contact points, and for scale the width of the larger blue crosses is 10 µm. The smaller crosses denote the points used for angle determination. Note the rounded shape surrounding the large blue crosses as well as subtle kinks in the detected edge near those points which arise from optical artifacts.

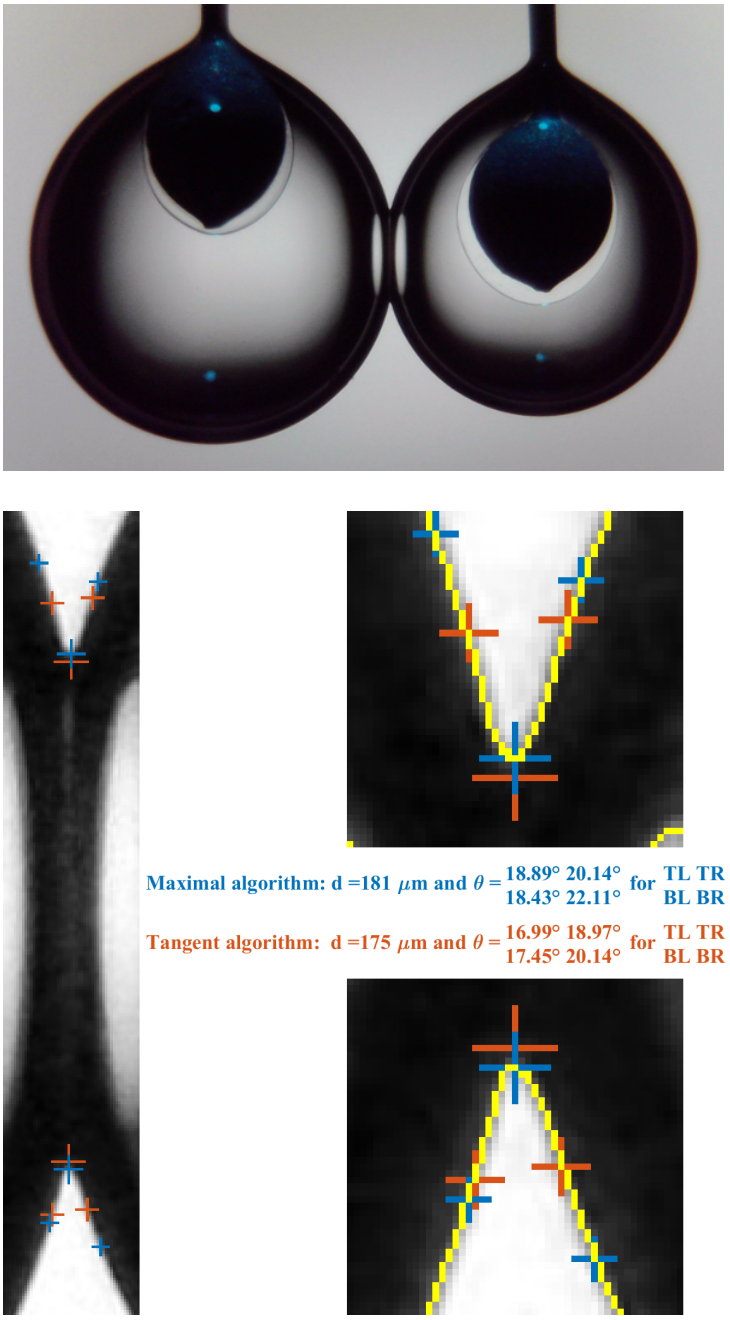

Figure 4.17: Side image of an experimental DIB (top) and a demonstration of the fitting process using Matlab (bottom). The same image processing is used as in Figure 4.16 and the colors have the same meanings. Again, the width of the larger blue crosses is 10 µm. Note the pixelation of the image due to the lower resolution of the side camera, and the same rounded shape surrounding the contact point.

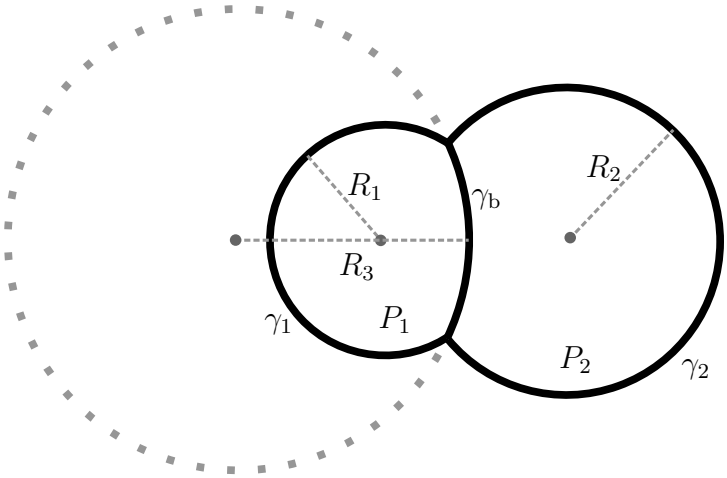

Figure 4.18: An asymmetric DIB in zero gravity. The left and right droplets have radii of curvature R_1 and R_2, monolayer tensions γ_1 and γ_2, and internal pressures P_1 and P_2, respectively. The bilayer has radius of curvature R_3 and tension γ_b.

the area of the associated spherical cap of radius R_3 gives an error or 0.02%. Even if the area were ten times as large, the percentage difference in area due to bowing would be 0.2%, so that the bilayer bowing due to the Laplace pressure can be neglected.

4.4.3 Optimization of algorithms for determining contact angles, bilayer areas, and tensions

There are various choices to make in the programming of the experimental approach explained above. One of these is the choice between the maximal and tangent algorithms. Another is the black/white threshold used prior to edge detection. To investigate the effect of these differences on experimental data, a set of 30 side images taken concurrently with 30 microscope images was analyzed. There was no significant variation over the 3 minute interval that the 60 images were taken. They were taken as a part of the experiment in Figure 4.22 so the monolayer tensions are $\gamma_L = 2.2$ mN/m and $\gamma_R = 3.4$ mN/m.

Figure 4.19 shows the results of the maximal and tangent algorithms for determining

the major and minor diameters as a function of the black/white threshold. It is not possible to know the true minor and major diameter, so this serves to show the sensitivity on the black/white threshold and the variability between pictures taken with the same settings. For both views, these span a ~5% range for a ~90 µm diameter, so by choosing a black/white threshold near the middle, it seems reasonable that the systemic error may be ±3%. The random error is given by the standard deviation σ of the diameter for the set of 60 images used. These σ values are of similar order (and are also relatively small) so that they do not constitute an important difference between the algorithms. In the absence of more compelling differences, we prefer the tangent algorithm because it is logically more likely to be accurate, considering that the maximal algorithm probably overestimates the area.

Figure 4.20 shows θ_{L} and θ_{R} for the same sequence of 60 images as a function of the black/white threshold. It is expected that the $\theta_{\mathrm{L,side}} = \theta_{\mathrm{L,bottom}}$ and $\theta_{\mathrm{R,side}} = \theta_{\mathrm{R,bottom}}$ from the spatial constancy of γ_{L}, γ_{R}, and γ_{b}. In the plot, these conditions hold for all black/white thresholds for the tangent algorithm but not for the maximal algorithm. Additionally, it is expected that $\theta_{\mathrm{L}} \neq \theta_{\mathrm{R}}$ due to the differing monolayer tensions of the two droplets. The tangent algorithm appears to do a better job at capturing the difference in θ_{L} and θ_{R} in both views. Another benefit of the tangent algorithm is that the standard deviation at each black/white threshold is lower, denoting a smaller random error. Finally, the tangent algorithm is less sensitive to changes in the black/white threshold. For all these reasons, the tangent algorithm is preferred for contact angle measurements.

Another parameter that was varied is the height at which droplet images are cropped before fitting their profile. This follows from the simulation results in Figure 4.12. The tops of the drop images were cropped off to avoid fitting a region whose shape is distorted by contact with the electrode as explained in Section 4.3.2. This was parametrized as

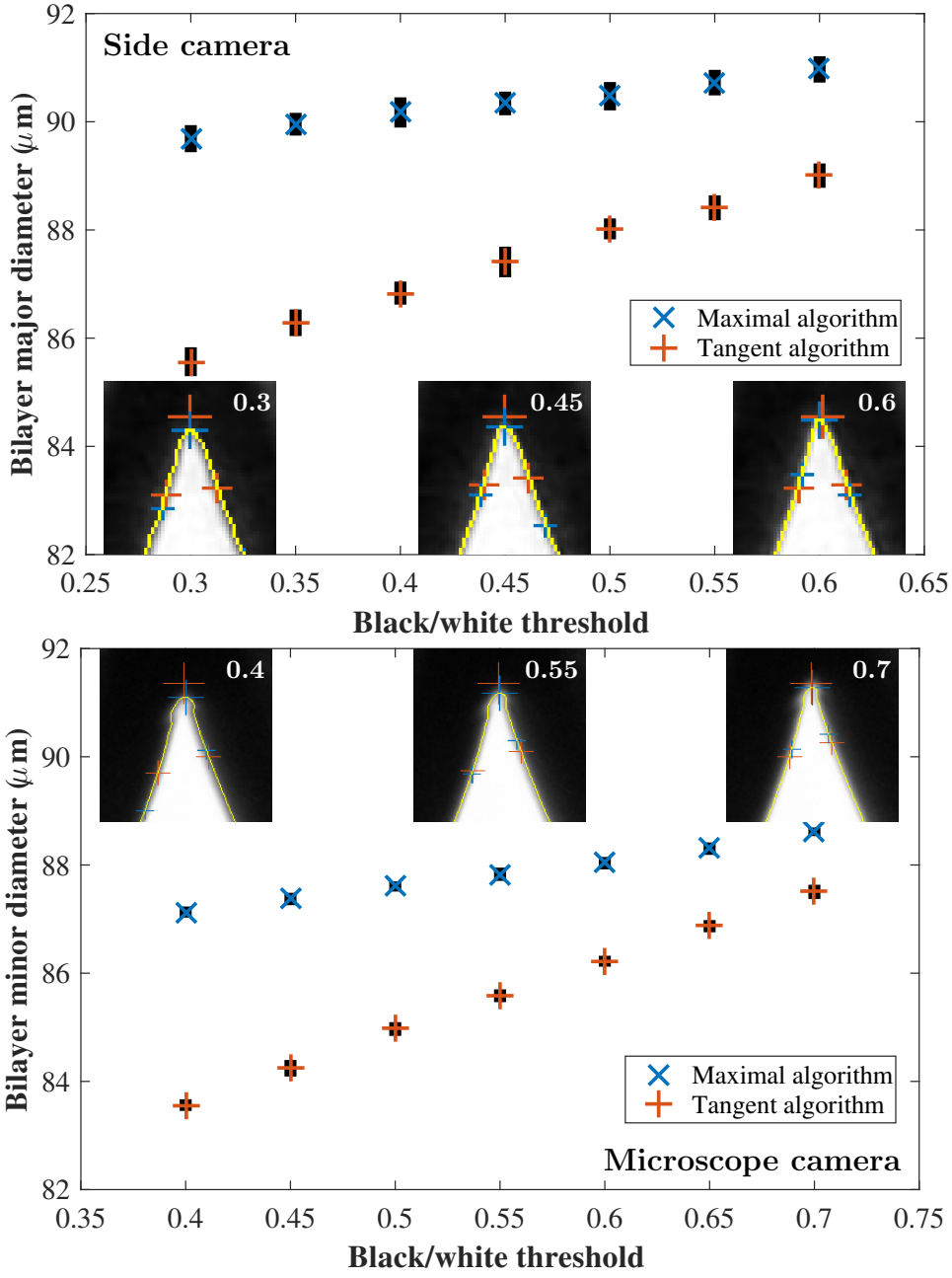

Figure 4.19: Comparison of maximal algorithm and tangent algorithm for computing bilayer interface diameter for microscope (top) and side camera (bottom) images. In every case, computed diameters for a group of 30 images are plotted against the black/white threshold used for edge detection in image processing. Note that the tangent algorithm has a greater dependence on the black/white threshold. The height of the error bars in black is double the standard deviation of each 30-image set.

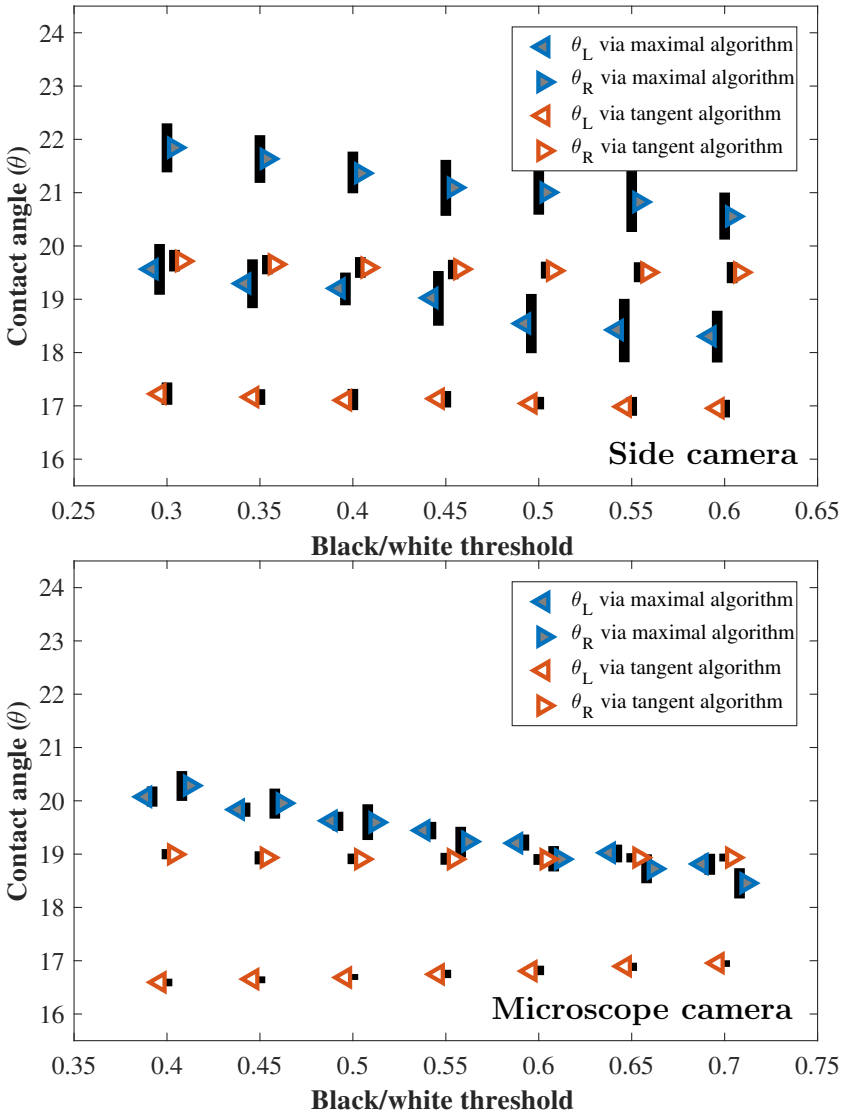

Figure 4.20: Comparison of maximal algorithm and tangent algorithm for computing left (θ_{L}) and right (θ_{R}) contact angles for microscope (top) and side camera (bottom) images. In every case, computed angles for a group of 30 images are plotted against the black/white threshold used for edge detection in image processing. Notice that that tangent algorithm is less sensitive to the black/white threshold, and also has a much smaller variation between measurements (as in Figure 4.19, the height of the error bars in black is double the standard deviation of each 30-image set.). Additionally, the tangent algorithm does a better job at capturing a difference between left and right contact angles in both cases. Note: the black/white threshold was varied only in increments of 0.05 and the data was offset horizontally as a visual aid.

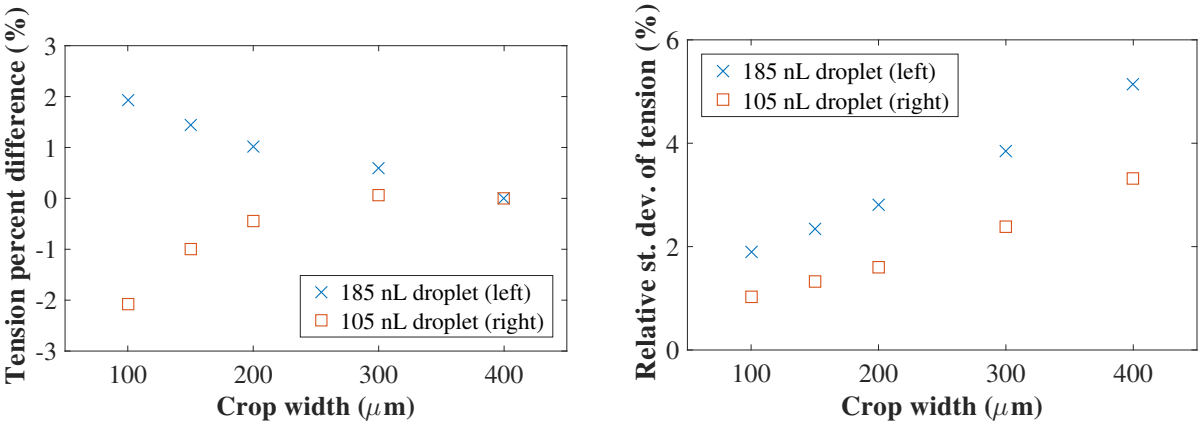

Figure 4.21: Demonstration that the measured tension in a DIB experiment with $PMOXA_{13}$-*b*-$PDMS_{47}$-*b*-$PMOXA_{13}$ in hexadecane is less sensitive to crop width than predicted by simulation in Figure 4.12. The tension is near 3.4 mN/m for the left droplet and is near 2.2 mN/m for the right droplet. The data is taken from between $t = 53$ and $t = 57$ minutes in Figure 4.22, where 40 side view images were taken; the number of images successfully processed was between 27 and 35 depending on crop width.

the crop width, the width of a droplet at which the droplet is cropped, as explained previously. The cropping was performed using a Matlab script that determined the droplet or electrode width at every row of pixels. The image processing was similar to that used for determining contact angles, using a black/white threshold and a Canny edge detector as the first step. The profile was smoothed with a nonlinear Matlab function which removed abrupt outlier points[12]. Then, beginning from the top of the image and moving downward, the first row with a width equal to the crop width was used as the cropping point for the image.

Figure 4.21 shows the how the random error for experimental tension measurements depends on crop width for symmetrized droplets for the experiment in Figure 4.22. A set of 40 side view images were taken, but number of images successfully processed was between 27 and 35 depending on crop width. The failures in processing were usually

[12]The setting "rloess" was used in the "smooth" command with a span of 0.02. The abrupt outlier points that needed to be removed were occasional dark pixels away from the droplets that fell below the black/white threshold.

due to bad initial guesses by Pendant Drop, which caused the fits to converge to a local optimum far from the global optimum. Surprisingly, all mean tension values are within 5% of each other for crop widths ranging from 100 to 400 µm; this is much smaller than for the simulations in Figure 4.12, suggesting that the simulated errors were artifacts of the simulation method.

Additionally, the variation between measurements at the same crop width is more pronounced at crop widths 200 µm, 300 µm, and 400 µm compared to the simulation results in Figure 4.12. Here the standard deviation is around 2-5% of the mean value. The reason for this was already explained in Section 4.3.2: the droplet tops are the richest in information, so cropping off more of them will introduce more random variation. The lower resolution of these images relative to the simulations exacerbates this effect. However, the quality of fits from Pendant Drop to both single and symmetrized droplets was generally good: in most cases, the RMS error between the fit line and the detected edge was less than 1 pixel. That the symmetrized droplets could be fit by a physically accurate profile is further evidence that the symmetrization algorithm gives accurate tension values for DIBs.

4.5 Results for real-time determination of tensions

Figure 4.22 shows the monolayer and bilayer tension traces for a carefully performed DIB experiment using shrunk droplets of aqueous $PMOXA_{13}$-*b*-$PDMS_{47}$-*b*-$PMOXA_{13}$ solution in a hexadecane bath. The bilayer tension was calculated via $\gamma_b = \gamma_L \cos\theta_L + \gamma_R \cos\theta_R$ with all quantities computed automatically as described in the previous sections. After an initial period of compressing the droplets to grow the bilayer area, the electrodes were separated to the location where the droplet bottoms were centered below the electrode contact points. Throughout the experiment, the electrode positions were manually adjusted in both relative height and separation to make the bilayer plane appear fully upright (i.e. aligned with the direction of gravity) from the side view. Without these adjustments, the bilayer continued to tilt away from the direction of gravity while one of the droplets climbed up its wire more than the other. Figure 4.23 shows the same experiment performed in two more trials, and time-averaged quantities corresponding to the three trials are tabulated in Table 4.3.

Considering the lack of equilibration of the contact angle, the use of $\gamma_b = \gamma_L \cos\theta_L + \gamma_R \cos\theta_R$ requires justification. Because the droplets were pushed into hard contact and then separated, the contact angles are brought closer to their equilibrium values, as demonstrated in Figure 4.7. The standard deviations of the contact angles in Table 4.4 show that the contact angle did not change much over the 60 minutes of data in Trial 1. This suggests that the contact angle is near equilibrium. Additionally, later in the same experiment (data not shown), the electrodes were separated slightly to increase the contact angles by an average of 3°. At this contact angle the bilayer area was observed to slowly decrease, which gives a definite upper bound on the equilibrium angles. Comparing e.g. $\cos 21°$ to $\cos 18°$ gives an error of about 2%, so that the errors arising from being out of equilibrium are small.

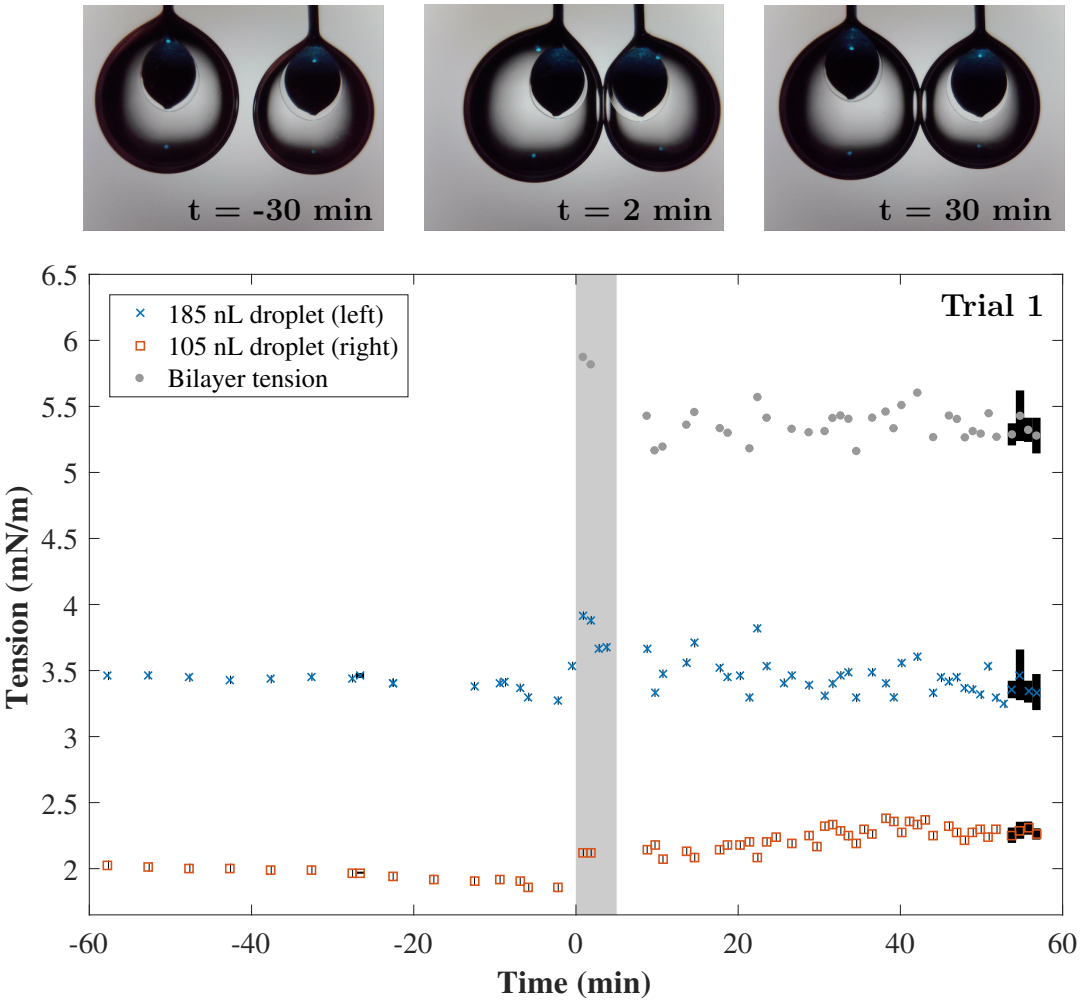

Figure 4.22: Monolayer and bilayer traces with representative images of the three stages in the experiment: before contact, during compression, and during contact. $t = 0$ is the time of contact and the shaded gray region denotes the time during which compression was high. Bilayer tension was calculated via $\gamma_b = \gamma_L \cos\theta_L + \gamma_R \cos\theta_R$. All monolayer tensions for times $t > 0$ are deduced by using the symmetrization procedure prior to pendant drop fits. The height of the error bars represent twice the standard deviation for sets of 10 side and bottom view pictures taken together. This gives an idea of the random variation in the measurement. Standard deviations include variations in angles and tensions, which were computed under the assumption that all variations are statistically independent. Note error bars that are barely visible for a set of 10 side view images taken near $t = -25$ mins. Also note that the monolayer of the right droplet is in contact with the agarose during the gray shaded region (top middle image), leading to a rise in the monolayer tension after contact.

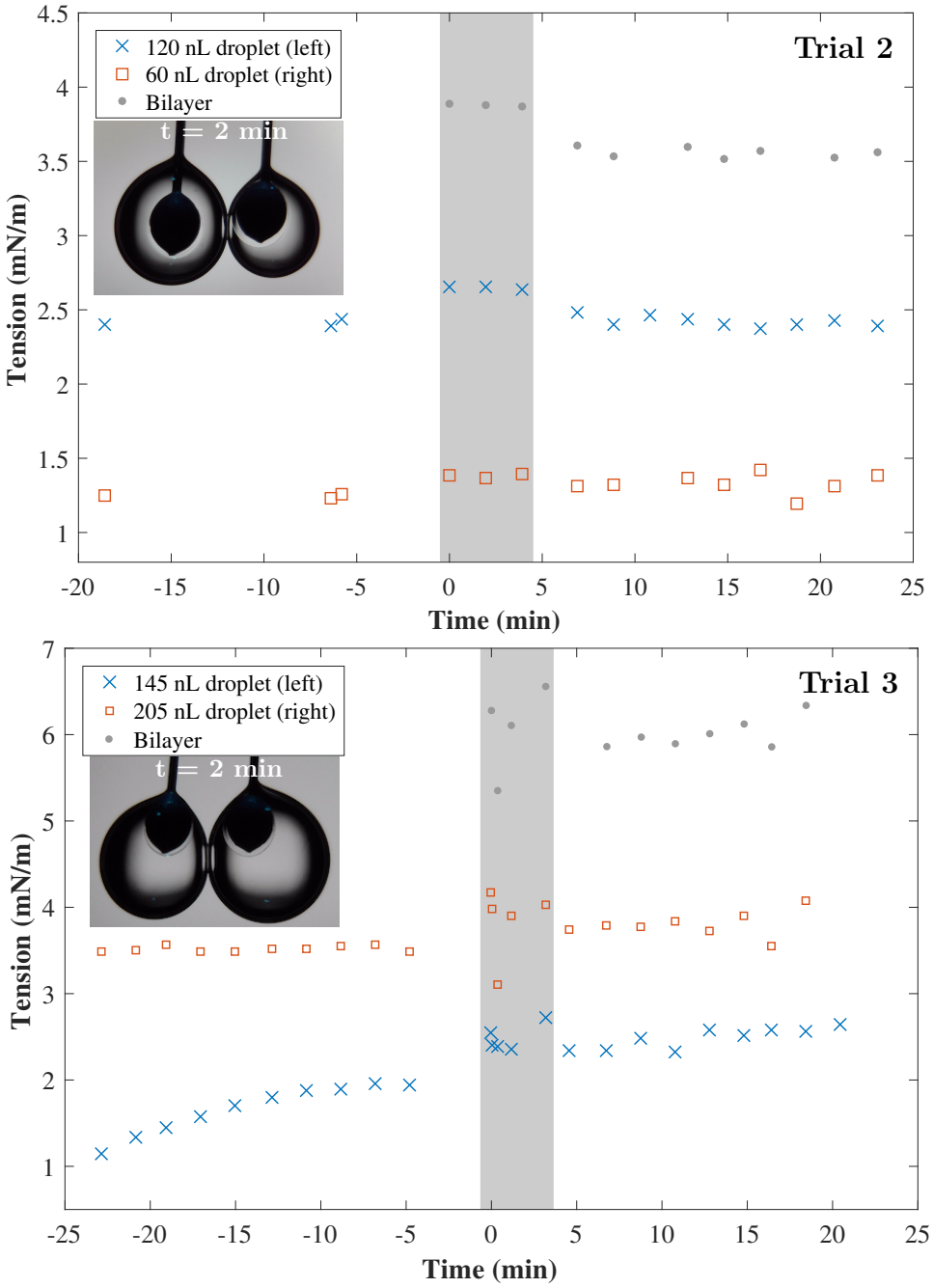

Figure 4.23: Monolayer and bilayer traces for two additional trials. As in Figure 4.22, $t > 0$ signifies contact and the gray region signifies high compression. The gray region includes $t < 0$ only to accommodate the plot marker size for aesthetic purposes. In Trial 3, the left droplet had not reached the expected monolayer tension given by Equation (4.2) prior to $t = 0$. Thus the difference between its post-contact and pre-contact monolayer tension is about twice as large as that of any of the other 5 droplets in Trials 1-3 whether by absolute or percentage rise. Gaps in data represent times when data was not taken or when automated analysis failed.

	$V_{\mathbf{L}}$	$V_{\mathbf{R}}$	$\gamma_{\mathbf{L},t<0}$	$\gamma_{\mathbf{L},t>0}$	$\gamma_{\mathbf{R},t<0}$	$\gamma_{\mathbf{R},t>0}$	$\gamma_{\mathbf{b}}$	C
Trial 1	185	105	3.41 (0.05)	3.44 (0.12)	1.95 (0.05)	2.24 (0.08)	5.36 (0.11)	0.207 (0.003)
Trial 2	120	60	2.41 (0.02)	2.42 (0.04)	1.25 (0.02)	1.33 (0.07)	3.56 (0.03)	0.194 (0.001)
Trial 3	145	205	1.93* (0.03)	2.41* (0.11)	3.52 (0.03)	3.81 (0.16)	5.92* (0.08)	0.227 (0.007)

Table 4.3: Results of the three trials of experiments performed on aqueous $PMOXA_{13}$-*b*-$PDMS_{47}$-*b*-$PMOXA_{13}$ in hexadecane. L and R denote the left and right droplet for each variable. With the exception of asterisked values, all values except volumes are averages performed over all times visible in Figures 4.22 and 4.23 excluding the grayed region. The corresponding standard deviations are given in parentheses. For asterisked values, only $|t| < 10$ mins was used. V denotes volumes in nL, γ denotes tensions in mN/m, and C denotes the specific capacitance in $\mu F/cm^2$. For monolayer tensions γ_L and γ_R, $t < 0$ denotes pre-contact tensions while $t > 0$ denotes post contact tension based on the image symmetrization procedure. Volumes are dispensed volumes V_d calculated as in Section 4.2.1. Additional geometric quantities are provided in Table 4.4.

For the five droplets whose tension plateaued prior to contact, the average monolayer tensions after contact are within 15% of those before contact. After contact, monolayer tension can change if the area per molecule in the monolayer increases or decreases. Assuming no leakage of polymer from the monolayers, this occurs both because the growth of the bilayer changes the monolayer area and because the bilayer can only take up molecules from the monolayer. Thus, the relevant parameters are the bilayer area and the area per molecule in the bilayer. Because it is expected that the area per molecule in the bilayer is either the same or not too different from the monolayer, and because the bilayer area is small in these experiments, it is expected that the monolayer tensions should not be significantly altered by the growth of the bilayer.

A look at the images during the initial hard contact period for Trial 1 shows that the monolayer of the right droplet was clearly in contact with the agarose for approximately 5 minutes. This is evident in the kink in the right droplet in the top center image in

	$\theta_{\mathbf{L,bot}}$	$\theta_{\mathbf{L,side}}$	$\theta_{\mathbf{R,bot}}$	$\theta_{\mathbf{R,side}}$	$d_{\mathbf{minor}}$	$d_{\mathbf{major}}$
Trial 1	16.6° (0.2°)	17.0° (0.2°)	19.0° (0.4°)	19.5° (0.2°)	85.5 (0.7)	87.1 (0.4)
Trial 2	16.3° (0.4°)	16.1° (0.2°)	20.2° (0.9°)	19.3° (0.5°)	71.4 (1.3)	71.8 (1.5)
Trial 3	15.7° (0.1°)	16.8° (0.4°)	14.7° (0.2°)	14.8° (0.4°)	78.7 (1.0)	83.0 (1.4)

Table 4.4: Additional geometric quantities for Table 4.3. Left and right contact angles θ_{L} and θ_{R} are each deduced from four measured angles, two angles from each view. The tangent algorithm was used to compute all values as described in Section 4.4.

Figure 4.22. This accounts for some of the 15% increase in γ_{R} after contact. A careful look at images during the initial hard contact period for Trial 3 is less conclusive; the monolayer of the right droplet is close to the agarose but the droplet is not kinked, so that they may or may not be in contact. If they are in contact, it could account for the 8% increase in γ_{R} after contact.

All droplets except for the left droplet in Trial 3 were plotted in Figure 4.4[13]. The left droplet in Trial 3 was excluded from the plot only because its tension had not yet plateaued prior to contact due to contact with the agarose. The expected tension due to Equation (4.2) is 2.55 mN/m while the actual tension was 1.93 mN/m, far greater than the ~5-10% discrepancy for the plateaued droplets as shown in Figure 4.4. Thus, it is expected that the rise in tension after contact would be larger than any of the other 5 droplets. This was indeed the case: the tension increased by 25% to 2.41 mN/m, which is near the predicted value of 2.55 mN/m. These observations justify the usefulness and validity of the symmetrization procedure; large changes in monolayer tension measured after contact are not due to artifacts of the symmetrization algorithm; rather, they arise from real physical changes in the system.

[13]Additionally, both the droplets in Trials 1 and 2 are plotted in Figure 4.3.

The specific capacitance measurements in Table 4.4 each have relatively small random errors, with standard deviations less than about 3% of the total. On the other hand, the variation among the specific capacitance determined in different trials is 17%. This suggests that either the specific capacitance can take different values depending on the experimental parameters or that there is a systemic error in the measurements. Without more data we cannot distinguish which of these is the case. If it is the result of a systemic error, the error may improve with the larger bilayer sizes and contact angles that are typical of lipid DIBs.

Comparison with other systems

One benefit of this method is that it obviates the need for the use of a bilayer area correction factor used by Taylor et al. [10]. They used Surface Evolver to compute correction factors for the bilayer area because in their case only a measurement of the minor diameter was available. In our case, the major diameter of the bilayer area can be measured directly. The use of smaller and asymmetric droplets makes it difficult to do a direct comparison to ellipticity factors predicted by Taylor, but a rough comparison can still be made. They predicted an ellipticity of approximately 1.03 for a monolayer tension of 2.5 mN/m and 300 nL droplets. The ellipticities in our experiments are 1.02, 1.01, and 1.05 for Trials 1, 2, and 3, respectively. Our ellipticities trend with average volume: 90 nL in Trial 2, 145 nL in Trial 1, and 175 nL in Trial 3. The values here and those predicted by Taylor et al. seem consistent with each other given the smaller size of our droplets. While these correction factors are small, they become significantly larger for larger droplets or lower interfacial tensions due to increased sagging.

Beltramo et al. [9] used a confocal microscope to determine the monolayer tension of a painted bilayer. They determined the monolayer tensions based on the shape of the solvent annulus using the Young-Laplace equation. However, their method requires

horizontal sectioning with a confocal microscope, so that the time for of each tension measurement is greater than 20 seconds. Our measurement time is only limited by the frame rate of the cameras we use. Additionally, they use a custom-made aperture with equipment that is more specialized than ours. Our method features the other benefits of DIBs, which includes the ability to make asymmetric bilayers. Still, there are trade-offs: their method provides for more accurate determination of bilayer area as well as a simple control over monolayer tension even for Gibbs monolayers.

In contrast to the oil-phase block copolymer DIBs in Tamadonni et al. [146], our system allows for asymmetric bilayers due to the inclusion of block copolymers in the aqueous phase. Additionally, while their monolayer and bilayer tensions are fixed by properties of the block copolymer solution, in our system, droplets of any arbitrary monolayer tension can be dispensed. This in turn determines the bilayer tension. This results from the insoluble characteristic of monolayers formed by our aqueous polymer solution as described earlier in the chapter.

Until now, the methods for determining monolayer and bilayer tension in DIBs in the literature [8, 10, 146] have used the Young-Lippmann equation (Equation (2.11)), which fails in the present case. In the cases where the Young-Lippmann equation may be used, measurements must be performed at different voltages, between which one must wait for the system to reach equilibrium. Additionally, it cannot be used for large voltages due to deviations from the Young-Lippmann equation. On the other hand, the droplet shape analysis used here works in real time and individually at any voltage. Because we used a triblock copolymer which does not readily achieve equilibrium, we expect that the quality of results will improve if this method is used for phospholipid DIBs.

4.6 Conclusions and future research

In this chapter, there were two main results. The first was that compressed Langmuir monolayers of $PMOXA_{13}$-*b*-$PDMS_{47}$-*b*-$PMOXA_{13}$ can be used to form a bilayer. The monolayer and bilayer tension have been decoupled from other system properties, allowing for deeper understanding of the membrane-protein interaction or of other membrane physical properties [9]. The dispersion of the polymer in the aqueous phase allows this method to generate asymmetric bilayers which can serve as more accurate models of cell membranes. The second main result was that droplet shape analysis can be used to determine monolayer and bilayer tensions in real time. The method is preferable to other methods for its ability to determine monolayer and bilayer tensions independent of applied voltage. The monolayer tension can be determined both prior to contact and during contact even if the bilayer is out of equilibrium. The use of the second camera also allows for more accurate bilayer area measurements. Additionally, the independent measurement of the monolayer tension of each droplet makes it better suited for asymmetric bilayers than the approach of Taylor et al.

Now that the system has been established and validated, the original goal of determining how bilayer tension and thickness affect MspA behavior can be addressed. The system could be used as is, or various improvements can be made. For example, control over the tension of compressed monolayers could be achieved by controlling the dispensed volume by an automated, precision system. The use of a side camera with a telecentric lens along with better lighting would improve the accuracy of droplet profiles and monolayer tension measurements. More broadly, droplet shape analysis is well-suited for characterizing the properties of different amphiphiles.

The work reported here leads naturally to more questions. Specifically, as applies to the triblock copolymer we used: is the leakage rate of triblock copolymer out of

compressed monolayers truly zero, or is it finite? This has implications for the long-term stability of devices made using compressed monolayers of our triblock copolymer. Also, what is the lowest tension that can be achieved without leakage of polymer out of the monolayer? How do the kinetics of adsorption of this triblock copolymer change when it is dissolved in the oil phase? In that case, would the polymer continue to behave as a Langmuir monolayer, or would the presence of aggregates in the oil phase increase the kinetics of both adsorption and desorption? How do asymmetric bilayers of the same triblock copolymer compare to asymmetric bilayers made of two different amphiphiles?

There are other questions that are raised for Gibbs monolayers. For example, considering the slow kinetics of bilayer area change in our polymer, what is the mechanism of growth for phospholipid DIBs? The microfluidic DIB method of Funakoshi et al. [45] is ideally suited for this experiment. Their setup makes it straightforward to form a packed monolayer using a phospholipid-oil solution and then to replace it with phospholipid-free oil prior to bilayer formation. If the bilayer formation rate depends on the presence of phospholipid in oil, this would show that the bilayer growth mechanism relies on phospholipid exchange with aggregates. Another question is whether contact with agarose affects phospholipid DIBs.

For real-time measurements of monolayer tension, the accuracy remains a question. While the simulation results suggest that the accuracy is ~5-10%, they are not ideal, considering the requirement to freeze parts of the simulation mesh and the ~5% error in tension when fitting the profiles of simulated single droplets. An alternative way to determine the accuracy of the method is to perform experiments on phospholipid DIBs with known properties. The method of Taylor et al. could also be used to determine monolayer and bilayer tensions in situ. Here the use of a new system using compressed monolayers made it difficult to assess the validity of real-time measurements of monolayer tension measurements. Some of these investigations are under way.

Appendix A

Analysis of DLS data

A.1 The relative number of small aggregates in polymer vesicles solutions made by ethanol injection

The intensity of scattered light due to spherical shells such as vesicles that have an index of refraction near that of water is given by [149]:

$$I(r) = \alpha \left[4\pi t \left(r - \frac{t}{2}\right)^2\right]^2 \times \left(\frac{3}{q^3 r^3 \left[1 - \frac{(r-t)^3}{r^3}\right]} \left[\sin(qr) - \sin(q[r-t]) + q(r-t)\cos(q[r-t]) - qr\cos(qr)\right]\right)^2 \tag{A.1}$$

where α is a constant, r is the shell radius, t is the shell thickness, and q is scattering vector. The scattering vector is $q = 4\pi n \sin\left(\frac{\theta}{2}\right)/\lambda$ where n is the index of refraction of the buffer solution ($n = 1.344$ for 1M KCl [150]), θ is the detection angle (173° for the Zetasizer, which detects backscattered light) and λ is the wavelength of light (632.8 nm

for the Zetasizer). The first term is the square of the volume of the vesicles, while the second term is the square of the form factor. Notably, the intensity oscillates in intensity when diameter is varied, with the first two minima near $r = 0$ and $r = 120$ nm for our experimental parameters.

Due to the complexity of this function, finding the relative number of small and large aggregates from the intensity distributions determined by DLS requires an involved calculation [149] that we do not attempt here. Instead we estimate the relative number of aggregates from the relative intensities of the intensity peaks as follows. First we assume a mean value and standard deviation for the number probability distributions $N_{\text{small}}(r)$ and $N_{\text{large}}(r)$ for small and large aggregates, which are approximated as normal distributions. Then we compute a weighted integral of each $N(r)$ with $I(r)$ in Equation (A.1) to provide the total intensities I_{small} and I_{large}. Because $N_{\text{small}}(r)$ and $N_{\text{large}}(r)$ are probability distributions normalized to 1, the ratio $I_{\text{large}}/I_{\text{small}}$ also gives the relative number of small and large aggregates if the intensities I_{large} and I_{small} were to be equal.

One source of uncertainty with this estimate is that number probability distributions are unknown. However, the number distributions are likely to be bounded by the intensity probability distribution on the one hand, and by the number distribution deduced by the Zetasizer assuming solid spheres on the other hand. Using these ranges gives that there are ~50 to ~2000 times more small aggregates than large aggregates in ethanol-injected solutions. By weighting this with the volume of the shells, this means there are between 1.5 and 10 times as much polymer in the small aggregates compared to the large aggregates. Another source of uncertainty is that the small aggregates are micelles (as explained in Chapter 4) whose optical intensities differ from small vesicles.

Bibliography

[1] B. Alberts, A. Johnson, J. Lewis, D. Morgan, M. Raff, K. Roberts, and P. Walter, *Molecular Biology of the Cell, Sixth Edition:*. Taylor & Francis Group, 2014.

[2] A. Krogh, B. Larsson, G. von Heijne, and E. L. Sonnhammer, *Predicting transmembrane protein topology with a hidden markov model: application to complete genomes11edited by f. cohen*, *Journal of Molecular Biology* **305** (2001), no. 3 567–580.

[3] L. Fagerberg, K. Jonasson, G. von Heijne, M. Uhlén, and L. Berglund, *Prediction of the human membrane proteome*, *PROTEOMICS* **10** (2010), no. 6 1141–1149.

[4] J. P. Overington, B. Al-Lazikani, and A. L. Hopkins, *How many drug targets are there?*, *Nature Reviews Drug Discovery* **5** (2006), no. 12 993–996.

[5] M. F. Brown, *Soft matter in lipid–protein interactions*, *Annual Review of Biophysics* **46** (2017), no. 1 379–410.

[6] G. W. Feigenson, *Phase boundaries and biological membranes*, *Annual Review of Biophysics and Biomolecular Structure* **36** (2007), no. 1 63–77.

[7] S. H. White, *Studies of the physical chemistry of planar bilayer membranes using high-precision measurements of specific capacitance*, *Ann. N. Y. Acad. Sci.* **303** (Dec, 1977) 243–265.

[8] L. C. M. Gross, A. J. Heron, S. C. Baca, and M. I. Wallace, *Determining membrane capacitance by dynamic control of droplet interface bilayer area*, *Langmuir* **27** (2011), no. 23 14335–14342.

[9] P. J. Beltramo, R. V. Hooghten, and J. Vermant, *Millimeter-area, free standing, phospholipid bilayers*, *Soft Matter* **12** (2016), no. 19 4324–4331.

[10] G. J. Taylor, G. A. Venkatesan, C. P. Collier, and S. A. Sarles, *Direct in situ measurement of specific capacitance, monolayer tension, and bilayer tension in a droplet interface bilayer*, *Soft Matter* **11** (2015), no. 38 7592–7605.

[11] J. Requena and D. Haydon, *The lippmann equation and the characterization of black lipid films*, *Journal of Colloid and Interface Science* **51** (1975), no. 2 315–327.

[12] A. J. Williams, *An introduction to the methods available for ion channel reconstitution*, in *Microelectrode techniques: the Plymouth Workshop handbook* (D. Ogden, ed.), ch. 5. Company of Biologists Limited, 1994.

[13] R. Kawano, T. Osaki, H. Sasaki, M. Takinoue, S. Yoshizawa, and S. Takeuchi, *Rapid detection of a cocaine-binding aptamer using biological nanopores on a chip*, *Journal of the American Chemical Society* **133** (2011), no. 22 8474–8477.

[14] G. Baaken, N. Ankri, A.-K. Schuler, J. Rühe, and J. C. Behrends, *Nanopore-based single-molecule mass spectrometry on a lipid membrane microarray*, *ACS Nano* **5** (2011), no. 10 8080–8088.

[15] D. Deamer, M. Akeson, and D. Branton, *Three decades of nanopore sequencing*, *Nature Biotechnology* **34** (2016), no. 5 518–524.

[16] K. Kita-Tokarczyk, J. Grumelard, T. Haefele, and W. Meier, *Block copolymer vesicles—using concepts from polymer chemistry to mimic biomembranes*, *Polymer* **46** (2005), no. 11 3540–3563.

[17] V. Malinova, S. Belegrinou, D. de Bruyn Ouboter, and W. Meier, *Biomimetic block copolymer membranes*, in *Advances in Polymer Science*. Springer Berlin Heidelberg, 2009.

[18] X. Zhang, P. Tanner, A. Graff, C. G. Palivan, and W. Meier, *Mimicking the cell membrane with block copolymer membranes*, *Journal of Polymer Science Part A: Polymer Chemistry* **50** (2012), no. 12 2293–2318.

[19] A. Blanazs, S. P. Armes, and A. J. Ryan, *Self-assembled block copolymer aggregates: From micelles to vesicles and their biological applications*, *Macromolecular Rapid Communications* **30** (2009), no. 4-5 267–277.

[20] D. Morton, S. Mortezaei, S. Yemenicioglu, M. J. Isaacman, I. C. Nova, J. H. Gundlach, and L. Theogarajan, *Tailored polymeric membranes for mycobacterium smegmatis porin a (MspA) based biosensors*, *J. Mater. Chem. B* **3** (2015), no. 25 5080–5086.

[21] T. Voets, K. Talavera, G. Owsianik, and B. Nilius, *Sensing with TRP channels*, *Nature Chemical Biology* **1** (2005), no. 2 85–92.

[22] M. D. Peraro and F. G. van der Goot, *Pore-forming toxins: ancient, but never really out of fashion*, *Nature Reviews Microbiology* **14** (2015), no. 2 77–92.

[23] E. Sezgin and P. Schwille, *Model membrane platforms to study protein-membrane interactions*, *Molecular Membrane Biology* **29** (2012), no. 5 144–154.

[24] F. M. Menger and M. I. Angelova, *Giant vesicles: imitating the cytological processes of cell membranes*, *Accounts of Chemical Research* **31** (1998), no. 12 789–797.

[25] O. Wesołowska, K. Michalak, J. Maniewska, and A. B. Hendrich, *Giant unilamellar vesicles - a perfect tool to visualize phase separation and lipid rafts in model systems*, *Acta Biochim. Pol.* **56** (2009), no. 1 33–39.

[26] M. Tanaka and E. Sackmann, *Polymer-supported membranes as models of the cell surface*, *Nature* **437** (2005), no. 7059 656–663.

[27] E. Sackmann, *Supported membranes: Scientific and practical applications*, *Science* **271** (1996), no. 5245 43–48.

[28] H. Bayley, B. Cronin, A. Heron, M. A. Holden, W. L. Hwang, R. Syeda, J. Thompson, and M. Wallace, *Droplet interface bilayers*, *Molecular BioSystems* **4** (2008), no. 12 1191.

[29] S. Aimon, J. Manzi, D. Schmidt, J. A. P. Larrosa, P. Bassereau, and G. E. S. Toombes, *Functional reconstitution of a voltage-gated potassium channel in giant unilamellar vesicles*, *PLoS ONE* **6** (2011), no. 10 e25529.

[30] J. H. A. Folgering, J. M. Kuiper, A. H. de Vries, J. B. F. N. Engberts, and B. Poolman, *Lipid-mediated light activation of a mechanosensitive channel of large conductance*, *Langmuir* **20** (2004), no. 17 6985–6987.

[31] X. Yajuan, L. Xin, and L. Zhiyuan, *A comparison of the performance and application differences between manual and automated patch-clamp techniques*, *Current Chemical Genomics* **6** (2012) 87–92.

[32] P. Mueller, D. O. Rudin, H. T. Tien, and W. C. Wescott, *Reconstitution of cell membrane structure in vitro and its transformation into an excitable system*, *Nature* **194** (1962), no. 4832 979–980.

[33] P. Mueller, D. O. Rudin, H. T. Tien, and W. C. Wescott, *Methods for the formation of single bimolecular lipid membranes in aqueous solution*, *The Journal of Physical Chemistry* **67** (1963), no. 2 534–535, [http://dx.doi.org/10.1021/j100796a529].

[34] S. H. White, *The physical nature of planar bilayer membranes*, in *Ion Channel Reconstitution*, pp. 3–35. Springer US, 1986.

[35] G. Szabo, G. Eisenman, and S. Ciani, *The effects of the macrotetralide actin antibiotics on the electrical properties of phospholipid bilayer membranes*, *The Journal of Membrane Biology* **1** (1969), no. 1 346–382.

[36] M. Montal and P. Mueller, *Formation of bimolecular membranes from lipid monolayers and a study of their electrical properties*, *Proceedings of the National Academy of Sciences* **69** (1972), no. 12 3561–3566, [http://www.pnas.org/content/69/12/3561.full.pdf].

[37] B. Fadeel and D. Xue, *The ins and outs of phospholipid asymmetry in the plasma membrane: roles in health and disease*, *Critical Reviews in Biochemistry and Molecular Biology* **44** (2009), no. 5 264–277.

[38] D. Marquardt, B. Geier, and G. Pabst, *Asymmetric lipid membranes: Towards more realistic model systems*, *Membranes* **5** (2015), no. 2 180–196.

[39] A. Wiese, M. Münstermann, T. Gutsmann, B. Lindner, K. Kawahara, U. Zähringer, and U. Seydel, *Molecular mechanisms of polymyxin b-membrane interactions: Direct correlation between surface charge density and self-promoted transport*, *Journal of Membrane Biology* **162** (1998), no. 2 127–138.

[40] M. Münstermann, A. Wiese, K. Brandenburg, U. Zähringer, L. Brade, K. Kawahara, and U. Seydel, *Complement activation by bacterial surface glycolipids: A study with planar bilayer membranes*, *Journal of Membrane Biology* **167** (1999), no. 3 223–232.

[41] M. D. Collins and S. L. Keller, *Tuning lipid mixtures to induce or suppress domain formation across leaflets of unsupported asymmetric bilayers*, *Proceedings of the National Academy of Sciences* **105** (2008), no. 1 124–128.

[42] S. White, D. Petersen, S. Simon, and M. Yafuso, *Formation of planar bilayer membranes from lipid monolayers. a critique*, *Biophysical Journal* **16** (1976), no. 5 481–489.

[43] L. M. Tsofina, E. A. Liberman, and A. V. Babakov, *Production of bimolecular protein-lipid membranes in aqueous solution*, *Nature* **212** (1966), no. 5063 681–683.

[44] D. W. Michaels and D. Dennis, *Asymmetric phospholipid bilayer membranes: Formation and electrical characterization*, *Biochemical and Biophysical Research Communications* **51** (1973), no. 2 357–363.

[45] K. Funakoshi, H. Suzuki, and S. Takeuchi, *Lipid bilayer formation by contacting monolayers in a microfluidic device for membrane protein analysis*, *Analytical Chemistry* **78** (2006), no. 24 8169–8174.

[46] M. Iwamoto and S. Oiki, *Contact bubble bilayers with flush drainage*, *Scientific Reports* **5** (2015), no. 1.

[47] S. Leptihn, O. K. Castell, B. Cronin, E.-H. Lee, L. C. M. Gross, D. P. Marshall, J. R. Thompson, M. Holden, and M. I. Wallace, *Constructing droplet interface bilayers from the contact of aqueous droplets in oil*, *Nature Protocols* **8** (2013), no. 6 1048–1057.

[48] E. C. Freeman, J. S. Najem, S. Sukharev, M. K. Philen, and D. J. Leo, *The mechanoelectrical response of droplet interface bilayer membranes*, *Soft Matter* **12** (2016), no. 12 3021–3031.

[49] O. S. Andersen and R. E. Koeppe, *Bilayer thickness and membrane protein function: An energetic perspective*, *Annual Review of Biophysics and Biomolecular Structure* **36** (2007), no. 1 107–130.

[50] J. Bibette, F. L. Calderon, and P. Poulin, *Emulsions: basic principles*, *Reports on Progress in Physics* **62** (1999), no. 6 969–1033.

[51] T. Takei, T. Yaguchi, T. Fujii, T. Nomoto, T. Toyota, and M. Fujinami, *Measurement of membrane tension of free standing lipid bilayers via laser-induced surface deformation spectroscopy*, *Soft Matter* **11** (2015), no. 44 8641–8647.

[52] A. D. Petelska and Z. A. Figaszewski, *Interfacial tension of the two-component bilayer lipid membrane modelling of cell membrane*, *Bioelectrochemistry and Bioenergetics* **46** (1998), no. 2 199–204.

[53] J. Schnitker, D. Afanasenkau, B. Wolfrum, and A. Offenhäusser, *Planar reference electrodes on multielectrode arrays for electrochemical measurements of ionic currents*, *physica status solidi (a)* **210** (2013), no. 5 892–897.

[54] H. Suzuki, K. Tabata, Y. Kato-Yamada, H. Noji, and S. Takeuchi, *Planar lipid bilayer reconstitution with a micro-fluidic system*, *Lab on a Chip* **4** (2004), no. 5 502.

[55] G. Baaken, M. Sondermann, C. Schlemmer, J. Rühe, and J. C. Behrends, *Planar microelectrode-cavity array for high-resolution and parallel electrical recording of membrane ionic currents*, *Lab on a Chip* **8** (2008), no. 6 938.

[56] T. Osaki, H. Suzuki, B. L. Pioufle, and S. Takeuchi, *Multichannel simultaneous measurements of single-molecule translocation in α-hemolysin nanopore array*, *Analytical Chemistry* **81** (2009), no. 24 9866–9870.

[57] M. Zagnoni, M. Sandison, and H. Morgan, *Microfluidic array platform for simultaneous lipid bilayer membrane formation*, *Biosensors and Bioelectronics* **24** (2009), no. 5 1235–1240.

[58] A. Hirano-Iwata, T. Nasu, A. Oshima, Y. Kimura, and M. Niwano, *Lipid bilayer array for simultaneous recording of ion channel activities*, *Applied Physics Letters* **101** (2012), no. 2 023702.

[59] R. Wheeler, *File:DNA Structure+Key+Labelled.pn NoBB.png — Wikimedia Commons, the free media repository*, 2015. `https://commons.wikimedia.org/w/index.php?title=File:DNA_Structure%2BKey%2BLabelled.pn_NoBB.png&oldid=182602131` [Online; accessed 31-July-2017].

[60] World Health Organization, *Genes and human disease*, 2017. `http://www.who.int/genomics/public/geneticdiseases/en/index2.html` [Online; accessed 8-August-2017].

[61] S. Zdravkovic, A. Wienke, N. L. Pedersen, M. E. Marenberg, A. I. Yashin, and U. D. Faire, *Heritability of death from coronary heart disease: a 36-year follow-up of 20 966 swedish twins*, *Journal of Internal Medicine* **252** (2002), no. 3 247–254.

[62] P. Poulsen, K. O. Kyvik, A. Vaag, and H. Beck-Nielsen, *Heritability of type II (non-insulin-dependent) diabetes mellitus and abnormal glucose tolerance - a population-based twin study*, *Diabetologia* **42** (1999), no. 2 139–145.

[63] P. Lichtenstein, N. V. Holm, P. K. Verkasalo, A. Iliadou, J. Kaprio, M. Koskenvuo, E. Pukkala, A. Skytthe, and K. Hemminki, *Environmental and heritable factors in the causation of cancer — analyses of cohorts of twins from sweden, denmark, and finland*, *New England Journal of Medicine* **343** (2000), no. 2 78–85.

[64] A. Antoniou, P. Pharoah, S. Narod, H. Risch, J. Eyfjord, J. Hopper, N. Loman, H. Olsson, O. Johannsson, Å. Borg, B. Pasini, P. Radice, S. Manoukian, D. Eccles, N. Tang, E. Olah, H. Anton-Culver, E. Warner, J. Lubinski, J. Gronwald, B. Gorski, H. Tulinius, S. Thorlacius, H. Eerola, H. Nevanlinna, K. Syrjäkoski, O.-P. Kallioniemi, D. Thompson, C. Evans, J. Peto, F. Lalloo, D. Evans, and D. Easton, *Average risks of breast and ovarian cancer associated with BRCA1 or BRCA2 mutations detected in case series unselected for family history: A combined analysis of 22 studies*, *The American Journal of Human Genetics* **72** (2003), no. 5 1117–1130.

[65] M. Morey, A. Fernández-Marmiesse, D. Castiñeiras, J. M. Fraga, M. L. Couce, and J. A. Cocho, *A glimpse into past, present, and future DNA sequencing*, *Molecular Genetics and Metabolism* **110** (2013), no. 1-2 3–24.

[66] Z. K. Stadler, K. A. Schrader, J. Vijai, M. E. Robson, and K. Offit, *Cancer genomics and inherited risk*, *Journal of Clinical Oncology* **32** (2014), no. 7 687–698.

[67] S.-M. Tu, M. A. Bilen, and N. M. Tannir, *Personalised cancer care: promises and challenges of targeted therapy*, *Journal of the Royal Society of Medicine* **109** (2016), no. 3 98–105.

[68] N. Zmora, D. Zeevi, T. Korem, E. Segal, and E. Elinav, *Taking it personally: Personalized utilization of the human microbiome in health and disease*, *Cell Host & Microbe* **19** (2016), no. 1 12–20.

[69] A. L. Komaroff, *The microbiome and risk for obesity and diabetes*, *JAMA* **317** (2017), no. 4 355.

[70] G. Egger, G. Liang, A. Aparicio, and P. A. Jones, *Epigenetics in human disease and prospects for epigenetic therapy*, *Nature* **429** (2004), no. 6990 457–463.

[71] L. C. Schenkel, D. I. Rodenhiser, P. J. Ainsworth, G. Paré, and B. Sadikovic, *DNA methylation analysis in constitutional disorders: Clinical implications of the epigenome*, *Critical Reviews in Clinical Laboratory Sciences* **53** (2016), no. 3 147–165.

[72] A. H. Laszlo, I. M. Derrington, H. Brinkerhoff, K. W. Langford, I. C. Nova, J. M. Samson, J. J. Bartlett, M. Pavlenok, and J. H. Gundlach, *Detection and mapping of 5-methylcytosine and 5-hydroxymethylcytosine with nanopore MspA*, *Proceedings of the National Academy of Sciences* **110** (2013), no. 47 18904–18909.

[73] J. Shendure and E. L. Aiden, *The expanding scope of DNA sequencing*, *Nature Biotechnology* **30** (2012), no. 11 1084–1094.

[74] K. A. Wetterstrand, *DNA Sequencing Costs: Data from the NHGRI Genome Sequencing Program (GSP)*. `http://www.genome.gov/sequencingcostsdata` [Online; accessed 31-July-2017].

[75] Wikipedia, *$1,000 genome — Wikipedia, The Free Encyclopedia*, 2017. `https://en.wikipedia.org/w/index.php?title=$1,000_genome&oldid=792593341` [Online; accessed 31-July-2017].

[76] J. M. Heather and B. Chain, *The sequence of sequencers: The history of sequencing DNA*, *Genomics* **107** (2016), no. 1 1–8.

[77] D. Branton, D. W. Deamer, A. Marziali, H. Bayley, S. A. Benner, T. Butler, M. D. Ventra, S. Garaj, A. Hibbs, X. Huang, S. B. Jovanovich, P. S. Krstic, S. Lindsay, X. S. Ling, C. H. Mastrangelo, A. Meller, J. S. Oliver, Y. V. Pershin, J. M. Ramsey, R. Riehn, G. V. Soni, V. Tabard-Cossa, M. Wanunu, M. Wiggin, and J. A. Schloss, *The potential and challenges of nanopore sequencing*, *Nature Biotechnology* **26** (2008), no. 10 1146–1153.

[78] Illumina, Inc., *Illumina Introduces the NovaSeq Seriesa New Architecture Designed to Usher in the $100 Genome*, 2017. http://www.businesswire.com/news/home/20170109006363/en/ [Online; accessed 25-July-2017].

[79] Oxford Nanopore Technologies, *Sets - Nanopore Store*, 2017. https://store.nanoporetech.com/minion/sets/ [Online; accessed 3-August-2017].

[80] Illumina, Inc., *Illumina Extends Genomics Portfolio*, 2016. http://http://www.businesswire.com/news/home/20160111006398/en/ [Online; accessed 3-August-2017].

[81] M. Wanunu, *Nanopores: A journey towards DNA sequencing*, *Physics of Life Reviews* **9** (2012), no. 2 125–158.

[82] J. J. Kasianowicz, E. Brandin, D. Branton, and D. W. Deamer, *Characterization of individual polynucleotide molecules using a membrane channel*, .

[83] T. Z. Butler, M. Pavlenok, I. M. Derrington, M. Niederweis, and J. H. Gundlach, *Single-molecule DNA detection with an engineered MspA protein nanopore*, *Proceedings of the National Academy of Sciences* **105** (2008), no. 52 20647–20652.

[84] K. R. Lieberman, G. M. Cherf, M. J. Doody, F. Olasagasti, Y. Kolodji, and M. Akeson, *Processive replication of single DNA molecules in a nanopore catalyzed by phi29 DNA polymerase*, *Journal of the American Chemical Society* **132** (2010), no. 50 17961–17972.

[85] E. A. Manrao, I. M. Derrington, A. H. Laszlo, K. W. Langford, M. K. Hopper, N. Gillgren, M. Pavlenok, M. Niederweis, and J. H. Gundlach, *Reading DNA at single-nucleotide resolution with a mutant MspA nanopore and phi29 DNA polymerase*, *Nature Biotechnology* **30** (2012), no. 4 349–353.

[86] A. H. Laszlo, I. M. Derrington, B. C. Ross, H. Brinkerhoff, A. Adey, I. C. Nova, J. M. Craig, K. W. Langford, J. M. Samson, R. Daza, K. Doering, J. Shendure, and J. H. Gundlach, *Decoding long nanopore sequencing reads of natural DNA*, *Nature Biotechnology* **32** (2014), no. 8 829–833.

[87] C. G. Brown and J. Clarke, *Nanopore development at oxford nanopore*, *Nature Biotechnology* **34** (2016), no. 8 810–811.

[88] S. Goodwin, R. Wappel, and W. R. McCombie, *1D Genome Sequencing on the Oxford Nanopore MinION*. John Wiley & Sons, Inc., 2001.

[89] M. Winterhalter, *Black lipid membranes*, *Current Opinion in Colloid & Interface Science* **5** (2000), no. 3-4 250–255.

[90] J. N. Israelachvili, *Intermolecular and Surface Forces*. Elsevier Inc., 3 ed., 2011.

[91] D. H. Everett, *Manual of symbols and terminology for physicochemical quantities and units, appendix II: Definitions, terminology and symbols in colloid and surface chemistry*, *Pure and Applied Chemistry* **31** (1972), no. 4.

[92] S. H. White, *Small phospholipid vesicles: internal pressure, surface tension, and surface free energy*, *Proc. Natl. Acad. Sci. U.S.A.* **77** (Jul, 1980) 4048–4050.

[93] P. A. K. Krassimir D. Danov and I. B. Ivanov, *Equilibrium and dynamics of surfactant adsorption monolayers and thin liquid films*, in *Handbook of Detergents: Properties*, Surfactant Science. Taylor & Francis, 1999.

[94] D. Needham and D. Haydon, *Tensions and free energies of formation of "solventless" lipid bilayers. measurement of high contact angles*, *Biophysical Journal* **41** (1983), no. 3 251–257.

[95] I. B. Ivanov, P. A. Kralchevsky, and A. D. Nikolov, *Film and line tension effects on the attachment of particles to an interface*, *Journal of Colloid and Interface Science* **112** (1986), no. 1 97–107.

[96] H. T. Tien, *Black lipid membranes at bifaces: Formation characteristics, optical and some thermodynamic properties*, *The Journal of General Physiology* **52** (1968), no. 1 125–144.

[97] P. Roura and J. Fort, *Local thermodynamic derivation of young's equation*, *Journal of Colloid and Interface Science* **272** (2004), no. 2 420–429.

[98] K. Seo, M. Kim, and D. H. Kim, *Re-derivation of young's equation, wenzel equation, and cassie-baxter equation based on energy minimization*, in *Surface Energy*. InTech, 2015.

[99] D. A. Balazs and W. Godbey, *Liposomes for use in gene delivery*, *Journal of Drug Delivery* **2011** (2011) 1–12.

[100] T. Smart, H. Lomas, M. Massignani, M. V. Flores-Merino, L. R. Perez, and G. Battaglia, *Block copolymer nanostructures*, *Nano Today* **3** (2008), no. 3-4 38–46.

[101] D. E. Discher and F. Ahmed, *Polymersomes*, *Annual Review of Biomedical Engineering* **8** (2006), no. 1 323–341.

[102] D. D. Lasic, *Spontaneous vesiculation and spontaneous liposomes*, *Journal of Liposome Research* **9** (1999), no. 1 43–52.

[103] S.-H. Choi, T. P. Lodge, and F. S. Bates, *Mechanism of molecular exchange in diblock copolymer micelles: Hypersensitivity to core chain length*, *Physical Review Letters* **104** (2010), no. 4.

[104] T. Zinn, L. Willner, V. Pipich, D. Richter, and R. Lund, *Molecular exchange kinetics of micelles: Corona chain length dependence*, *ACS Macro Letters* **5** (2016), no. 7 884–888.

[105] A. W. Adamson and A. P. Gast, *Physical Chemistry of Surfaces*. John Wiley & Sons, Inc., 6 ed., 1997.

[106] V. M. Kaganer, H. Möhwald, and P. Dutta, *Structure and phase transitions in langmuir monolayers*, *Reviews of Modern Physics* **71** (1999), no. 3 779–819.

[107] Z. Matharu, A. J. Bandodkar, V. Gupta, and B. D. Malhotra, *Fundamentals and application of ordered molecular assemblies to affinity biosensing*, *Chem. Soc. Rev.* **41** (2012), no. 3 1363–1402.

[108] C. Isenberg, *The Science of Soap Films and Soap Bubbles*. Dover books explaining science. Dover Publications, 1978.

[109] B. Lautrup, *Physics of Continuous Matter, Second Edition: Exotic and Everyday Phenomena in the Macroscopic World*. CRC Press, 2011.

[110] B. Guo, *Proof of the young–laplace equation using the theory of calculus of variations applied to petroleum fluids*, *Petroleum Science and Technology* **21** (2003), no. 7-8 1159–1165.

[111] A. Daerr and A. Mogne, *Pendent_drop: An ImageJ plugin to measure the surface tension from an image of a pendent drop*, *Journal of Open Research Software* **4** (2016).

[112] B. Song and J. Springer, *Determination of interfacial tension from the profile of a pendant drop using computer-aided image processing*, *Journal of Colloid and Interface Science* **184** (1996), no. 1 64–76.

[113] A. Bard and L. Faulkner, *Electrochemical Methods: Fundamentals and Applications, 2nd Edition*. John Wiley & Sons, 2000.

[114] Oxford Nanopore Technologies, *Update: New 'R9' nanopore for faster, more accurate sequencing, and new ten minute preparation kit*, 2016. https://nanoporetech.com/about-us/news/update-new-r9-nanopore-faster-more-accurate-sequencing-and-new-ten-minute-preparation [Online; accessed 3-August-2017].

[115] M. J. Isaacman, K. A. Barron, and L. S. Theogarajan, *Clickable amphiphilic triblock copolymers*, *Journal of Polymer Science Part A: Polymer Chemistry* **50** (2012), no. 12 2319–2329.

[116] G. Bainbridge, I. Gokce, and J. H. Lakey, *Voltage gating is a fundamental feature of porin and toxin β-barrel membrane channels*, *FEBS Letters* **431** (1998), no. 3 305–308.

[117] J. Huff, M. Pavlenok, S. Sukumaran, and M. Niederweis, *Functions of the periplasmic loop of the porin MspA fromMycobacterium smegmatis*, *Journal of Biological Chemistry* **284** (2009), no. 15 10223–10231.

[118] E. Perozo, D. M. Cortes, P. Sompornpisut, A. Kloda, and B. Martinac, *Open channel structure of MscL and the gating mechanism of mechanosensitive channels*, *Nature* **418** (2002), no. 6901 942–948.

[119] F. Wohnsland and R. Benz, *1/ f -noise of open bacterial porin channels*, *Journal of Membrane Biology* **158** (1997), no. 1 77–85.

[120] S. M. Bezrukov and M. Winterhalter, *Examining noise sources at the single-molecule level:1/fNoise of an open maltoporin channel*, *Physical Review Letters* **85** (2000), no. 1 202–205.

[121] E. M. Nestorovich, T. K. Rostovtseva, and S. M. Bezrukov, *Residue ionization and ion transport through OmpF channels*, *Biophysical Journal* **85** (2003), no. 6 3718–3729.

[122] M. Queralt-Martín, M. L. López, and A. Alcaraz, *Excess white noise to probe transport mechanisms in a membrane channel*, *Physical Review E* **91** (2015), no. 6.

[123] F. Itel, A. Najer, C. G. Palivan, and W. Meier, *Dynamics of membrane proteins within synthetic polymer membranes with large hydrophobic mismatch*, *Nano Letters* **15** (2015), no. 6 3871–3878.

[124] H.-A. Klok, P. Eibeck, M. Möller, and D. N. Reinhoudt, *Synthesis and characterization of polysiloxane-bound receptor molecules for ion-selective supported polymeric membranes*, *Macromolecules* **30** (1997), no. 4 795–802.

[125] M. E. Sandison, M. Zagnoni, and H. Morgan, *Air-exposure technique for the formation of artificial lipid bilayers in microsystems*, *Langmuir* **23** (2007), no. 15 8277–8284.

[126] S. H. White, *Analysis of the torus surrounding planar lipid bilayer membranes*, *Biophysical Journal* **12** (1972), no. 4 432–445.

[127] M. Faller, *The structure of a mycobacterial outer-membrane channel*, *Science* **303** (2004), no. 5661 1189–1192.

[128] C. Nardin, M. Winterhalter, and W. Meier, *Giant free-standing ABA triblock copolymer membranes*, *Langmuir* **16** (2000), no. 20 7708–7712.

[129] D. Wong, T.-J. Jeon, and J. Schmidt, *Single molecule measurements of channel proteins incorporated into biomimetic polymer membranes*, *Nanotechnology* **17** (2006), no. 15 3710–3717.

[130] C. Jaafar-Maalej, R. Diab, V. Andrieu, A. Elaissari, and H. Fessi, *Ethanol injection method for hydrophilic and lipophilic drug-loaded liposome preparation*, *Journal of Liposome Research* **20** (2009), no. 3 228–243.

[131] C. Nardin, T. Hirt, J. Leukel, and W. Meier, *Polymerized ABA triblock copolymer vesicles*, *Langmuir* **16** (2000), no. 3 1035–1041.

[132] T. Haefele, K. Kita-Tokarczyk, and W. Meier, *Phase behavior of mixed langmuir monolayers from amphiphilic block copolymers and an antimicrobial peptide*, *Langmuir* **22** (2006), no. 3 1164–1172.

[133] A. Güven, M. Ortiz, M. Constanti, and C. K. O'Sullivan, *Rapid and efficient method for the size separation of homogeneous fluorescein-encapsulating liposomes*, *Journal of Liposome Research* **19** (2009), no. 2 148–154.

[134] Malvern Instruments Ltd, *Intensity - Volume - Number*, 2017. `https://www.malvern.com/en/support/resource-center/technical-notes/TN101104IntensityVolumeNumber.html` [Online; accessed 16-August-2017].

[135] F. Itel, M. Chami, A. Najer, S. Lörcher, D. Wu, I. A. Dinu, and W. Meier, *Molecular organization and dynamics in polymersome membranes: A lateral diffusion study*, *Macromolecules* **47** (2014), no. 21 7588–7596.

[136] G. A. Venkatesan, J. Lee, A. B. Farimani, M. Heiranian, C. P. Collier, N. R. Aluru, and S. A. Sarles, *Adsorption kinetics dictate monolayer self-assembly for both lipid-in and lipid-out approaches to droplet interface bilayer formation*, *Langmuir* **31** (2015), no. 47 12883–12893.

[137] A. Goebel and K. Lunkenheimer, *Interfacial tension of the water/n-alkane interface*, *Langmuir* **13** (1997), no. 2 369–372.

[138] R. Aveyard and S. M. Saleem, *Interfacial tensions at alkane-aqueous electrolyte interfaces*, *Journal of the Chemical Society, Faraday Transactions 1: Physical Chemistry in Condensed Phases* **72** (1976), no. 0 1609.

[139] E. G. Kelley, R. P. Murphy, J. E. Seppala, T. P. Smart, S. D. Hann, M. O. Sullivan, and T. H. Epps, *Size evolution of highly amphiphilic macromolecular solution assemblies via a distinct bimodal pathway*, *Nature Communications* **5** (2014).

[140] J. Lu, F. S. Bates, and T. P. Lodge, *Remarkable effect of molecular architecture on chain exchange in triblock copolymer micelles*, *Macromolecules* **48** (2015), no. 8 2667–2676.

[141] A. Halperin and S. Alexander, *Polymeric micelles: their relaxation kinetics*, *Macromolecules* **22** (1989), no. 5 2403–2412.

[142] D. Kwok, D. Vollhardt, R. Miller, D. Li, and A. Neumann, *Axisymmetric drop shape analysis as a film balance*, *Colloids and Surfaces A: Physicochemical and Engineering Aspects* **88** (1994), no. 1 51–58.

[143] H. Wege, J. Holgado-Terriza, M. Gálvez-Ruiz, and M. Cabrerizo-Vílchez, *Development of a new langmuir-type pendant-drop film balance*, *Colloids and Surfaces B: Biointerfaces* **12** (1999), no. 3-6 339–349.

[144] J. Li, R. Miller, and H. Möhwald, *Characterisation of phospholipid layers at liquid interfaces 2. comparison of isotherms of insoluble and soluble films of phospholipids at different fluid/water interfaces*, *Colloids and Surfaces A: Physicochemical and Engineering Aspects* **114** (1996) 123–130.

[145] N. Hardy, T. Richardson, and F. Grunfeld, *Minimising monolayer collapse on langmuir troughs*, *Colloids and Surfaces A: Physicochemical and Engineering Aspects* **284-285** (2006) 202–206.

[146] N. Tamaddoni, G. Taylor, T. Hepburn, S. M. Kilbey, and S. A. Sarles, *Reversible, voltage-activated formation of biomimetic membranes between triblock copolymer-coated aqueous droplets in good solvents*, *Soft Matter* **12** (2016), no. 23 5096–5109.

[147] Gelest, Inc., *Octamethylcyclotetrasiloxane, 98% — Gelest, Inc.* `https://www.gelest.com/product/octamethylcyclotetrasiloxane-98/` [Online; accessed 15-Aug-2017].

[148] W. Noll, *Chemistry and Technology of Silicones*. Elsevier Science, 2012.

[149] F. Hallett, J. Watton, and P. Krygsman, *Vesicle sizing*, *Biophysical Journal* **59** (1991), no. 2 357–362.

[150] C.-Y. Tan and Y.-X. Huang, *Dependence of refractive index on concentration and temperature in electrolyte solution, polar solution, nonpolar solution, and protein solution*, *Journal of Chemical & Engineering Data* **60** (2015), no. 10 2827–2833.